



---

# Scientific Technical Report

ISSN 1610-0956

Fabien Magri

**Mechanismus und Fluidodynamik der  
Salzwasserzirkulation im  
Norddeutschen Becken:  
Ergebnisse thermohaliner numerischer  
Simulationen**

---

Dissertation  
zur Erlangung des Doktorgrades  
des Fachbereiches Geowissenschaften  
der Freien Universität Berlin  
Berlin 2005



Scientific Technical Report STR05/12



# **Mechanismus und Fluidodynamik der Salzwasserzirkulation im Norddeutschen Becken: Ergebnisse thermohaliner numerischer Simulationen**

**Laureato in Fisica (Scienze della Terra)**

**Fabien Magri**

vom Fachbereich Geowissenschaften  
der Freien Universität Berlin  
zur Erlangung des akademischen Grades eines  
Dr. rer. nat  
genehmigte Dissertation  
Berlin, 2005

Gutachter:

Prof. Dr. U. Bayer

Prof. Dr. A. Pekdeger

Tag der Disputation: 10. Juni 2005

GeoForschungsZentrum Potsdam

Scientific Technical Report STR 05/12





<b>Chapter 1. Introduction.....</b>	<b>1</b>
1.1 The North East German Basin: an unexplained large-scale transport system of dissolved halite.....	1
1.2 Data: aquifer and fluid model.....	4
1.2.1 Database and sampling location.....	5
1.2.2 Aquifer model.....	6
1.2.3 Fluid model: chemistry and density.....	8
1.3 Discussion and approaches.....	16
 <b>Chapter 2. 2D thermohaline approach: model scenario and preliminary simulations.....</b>	 <b>19</b>
2.1 Definition of the two-dimensional model scenario for thermohaline simulations by use of FEFLOW®.....	19
2.1.1 The need of a two-dimensional approach.....	19
2.1.2 Integration of the structural model of the NEGB into FEFLOW®.....	20
2.1.3 The representative NEGB cross-section.....	22
2.2 Preliminary 2D thermohaline simulations.....	24
2.2.1 Governing equations and assumptions.....	24
2.2.2 Boundary and initial conditions.....	27
2.2.3 Numerical and time step schemes.....	29
2.2.4 Building a mesh suitable for the thermohaline approach.....	32
2.3 Discussion.....	37
 <b>Chapter 3. Mechanisms driving brines within the NEGB. Results from 2D coupled fluid flow mass transport and thermohaline simulations.....</b>	 <b>39</b>
3.1 Diffusive brine transport.....	39
3.1.1 Boundary conditions.....	39
3.1.2 Diffusive brine transport without regional flow.....	41
3.1.3 Diffusive brine transport and regional flow.....	46
3.2 Thermohaline convection.....	53
3.2.1 Boundary conditions.....	54
3.2.2 Free convection.....	55
3.2.3 Mixed convection.....	65
3.2.4 Viscosity effects.....	71
3.3 Discussion.....	78

<b>Chapter 4</b>	<b>Three dimensional approach.....</b>	<b>79</b>
4.1	Large scale model scenario.....	79
4.2	Square box model scenario.....	82
4.3	Discussion.....	88
<b>Chapter 5</b>	<b>Summary and discussion-.....</b>	<b>89</b>
<b>References.....</b>		<b>93</b>
Appendix 1	Fluid, heat and mass transport equations in porous media.....	101
Appendix 2	Derivation of the coefficients of thermal expansion and compressibility for use in FEFLOW .....	111
Appendix 3	Implementation of the coefficient of thermal expansion and compressibility through the IFM interface manager for use with FEFOW .....	119
Appendix 4	Rayleigh stability criteria.....	125

Figures list	Pages
<b>Fig.1-1:</b> Study area, location of the observed springs (Schirrmeister 1996) and salty groundwater interface (Grube et al. 2000). The thin sediments area is denoted with “Uplifted”.	2
<b>Fig.1-2: a)</b> Glaux maritima (Sea Milkwort) and <b>b)</b> Triglochin maritimum (Sea Arrowgrass). The pictures were taken during a field trip in Gröben in 2004.	3
<b>Fig.1-3:</b> Sampling location for the lithological and petrophysical data ( <b>left</b> ), and for the chemistry and dynamics of deep and saline fluids ( <b>right</b> ). (provided by C. Jahnke, BTU)	5
<b>Fig.1-4:</b> Relief of the Top Zechstein derived from the geological input data (Scheck 1997; Scheck and Bayer 1999).	6
<b>Table.1-1 Physical parameters assigned to the stratigraphic layers.</b>	7
<b>Fig.1-5: Left:</b> Top Zechstein depth map (Scheck 1997), location of the observed springs (Schirrmeister 1996) and salty groundwater interface (Grube et al. 2000). <b>Right:</b> NEGB topography (Scheck 1997), location of the observed springs (Schirrmeister 1996) and salty groundwater interface (Grube et al. 2000).	9
<b>Fig 1-6:</b> Depth salinity trend of the groundwater samples in relation to the stratigraphic units of the NEGB (provided by M. Tasmer, FU Berlin).	10
<b>Fig. 1-7:</b> T-p corrected in-situ brine densities for the stratigraphic units (a) Cretaceous-Keuper (b) Buntsandstein (c) Zechstein (Provided by C. Jahnke, BTU Cottbus)	13
<b>Fig 1-8:</b> Spatial distribution of the density within: a) base of Jurassic b) top Buntsandstein c) base Buntsandstein (Provided by C. Jahnke, BTU Cottbus)	14
<b>Fig 1-9:</b> Corrected pressure gradients in the different stratigraphic units of the NEGB. (Provided by C. Jahnke, BTU Cottbus)	15
<b>Fig. 2-1:</b> 3D rendering of the NEGB incorporated in FEFLOW. The stratigraphic units abbreviations are given in Tab. 1-1. A detail of a finite element used to discretize the whole model volume is shown in the circle. The dashed line localizes the cross-section chosen for the 2D thermohaline model scenario (Fig. 2-2).	21
<b>Fig. 2-2 a:</b> Location of the 2D cross-section together with the fresh/salty water interface and saline springs as shown in Fig. 1-5	23
<b>Fig. 2-2 b:</b> Stratigraphic units of the 2D cross-section. The stratigraphic units abbreviations are given in Tab. 1-1.	24
<b>Fig.2-3: A:</b> Boundary conditions of the preliminary thermohaline simulations and, <b>B:</b> Initial temperature distribution (°C) derived from a steady-state heat transport problem. The bold line delimits the Top Salt. Temperature values have been interpolated with a Kriging gridding method by use of the commercial software Surfer 8.	28
<b>Fig.2-4:</b> Adaptive time scheme strategy for coupled transient flow, mass and heat transport.(Modified from Diersch and Kolditz 1998).	31
<b>Fig.2-5:</b> Initial finite element mesh obtained from the original 3D structural model of the NEGB. For pictorial needs a 10:1 vertical exaggeration is used. 60 grid points discretize each model slices. The rectangle delimits a salt dome environment which is illustrated in Fig.2-6 and Fig.2-7 with no vertical exaggeration.	32
<b>Fig.2-6:</b> Zoom of the initial finite element mesh in salt a dome environment. No vertical exaggeration. The mesh resolution of the cross-section from which this zoom is obtained is 60 grid points per slice. The chosen salt dome is localized in the rectangle depicted in Fig.2-5.	33
<b>Fig. 2-7:</b> Sketch illustrating the mesh robustness as a function of the number of grid points discretizing the model slices in the horizontal direction (x).	34
<b>Fig.2-.8:</b> Zoom of the refined finite element mesh in salt a dome environment. No vertical exaggeration. The mesh resolution of the cross-section from which this zoom is obtained is 159 grid points per slice. The chosen salt dome is localized in the rectangle depicted in Fig.2-5.	35
<b>Fig.2-9:</b> Mass distribution obtained from: a thermohaline simulation ( <b>A</b> ), and from a coupled fluid flow and mass transport simulation ( <b>B</b> ).	36
<b>Fig.2-10:</b> Zoom of the final finite element mesh in salt a dome environment. No vertical exaggeration. The final mesh resolution of the cross-section from which this zoom is obtained is 633 grid points per slice. The chosen salt dome is localized in the rectangle depicted in Fig.2-4.	37

<b>Fig.3-1: A and B</b> mass distribution resulting from coupled fluid flow and mass transport simulation at and respectively. The regional flow is excluded from the numerical computation. Salt concentrations are expressed in g/L. The snapshots are interpolated by the use of Surfer 8® and illustrated with a 10:1 vertical exaggeration. Two profiles P1 and P2 are located within the cross-section. The simulation results for these two profiles are shown with no vertical exaggeration in Fig.3.2 and Fig.3.3	42
<b>Fig.3-2: A and B:</b> Zoom of the diffusive brine transport simulation results for profile P1 as located in Fig.3.1 at $t = 30$ ka and at $t = 200$ ka respectively. No vertical exaggeration is used. <b>1:</b> pore water velocity field in $\text{myr}^{-1}$ . Pore vector linearly scaled to the largest flow arrow. <b>2:</b> Salt concentration distribution in g/L	44
<b>Fig.3-3: A and B:</b> Zoom of the diffusive brine transport simulation results for profile P2 as located in Fig.3.1 at $t = 30$ ka and $t = 200$ ka . No vertical exaggeration is used. <b>1:</b> pore water velocity field in $\text{myr}^{-1}$ . Pore vector linearly scaled to the largest flow arrow. <b>2:</b> Salt concentration distribution in g/L	45
<b>Fig.3-4: A:</b> Topography-induced groundwater flow (regional flow). Velocities are expressed in $\text{myr}^{-1}$ . Black bold lines indicate the flow direction in the shallow aquifer. Dashed lines depict the flow circulation in the deeper part of the basin. <b>B:</b> Geological structure (stratigraphic units abbreviations in Table 1.1)	47
<b>Fig.3-5: A and B:</b> Mass distribution resulting from coupled brine transport and regional flow simulation at $t = 30$ ka and $t = 200$ ka respectively	49
<b>Fig.3-6: A and B:</b> Zoom of the coupled brine transport and regional flow simulation results for profile P3 as located in Fig.3.4 at $t = 30$ ka and $t = 200$ ka respectively .No vertical exaggeration is used. <b>1:</b> Pore water velocity field in $\text{myr}^{-1}$ . Pore vector	51
<b>Fig.3-7:</b> Zoom of the coupled brine transport and regional flow simulation results for profile P4 as located in Fig.3.4 at $t = 30$ ka and $t = 200$ ka respectively. No vertical exaggeration is used. <b>1:</b> Pore water velocity field in $\text{myr}$	52
<b>Fig.3-8: A and B:</b> Mass distribution resulting from free thermohaline simulation at $t = 30$ ka and $t = 200$ ka respectively. Salt concentrations are expressed in g/L. Two profiles P3 and P4 are located within the cross-section. The simulation results for these two profiles are shown with no vertical exaggeration in Fig.3-10 and Fig.3-11	56
<b>Fig.3-9: A and B:</b> Temperature distribution resulting from free thermohaline simulation at $t = 30$ ka and $t = 200$ ka respectively. Temperatures are expressed in °C. Two profiles P3 and P4 are located within the cross-section. The simulation results for these two profiles are shown with no vertical exaggeration in Fig.3-10 and Fig.3-11	57
<b>Fig.3-10: A and B:</b> Zoom of the thermohaline simulation results for profile P3 as located in Fig.3-8 at $t = 30$ ka and $t = 200$ ka respectively . No vertical exaggeration is used. <b>1:</b> Pore water velocity field in $\text{myr}^{-1}$ . Pore vector	61
<b>Fig.3-11: A and B:</b> Zoom of the thermohaline simulation results for profile P4 as located in Fig.3-8 at $t = 30$ ka and $t = 200$ ka respectively . No vertical exaggeration is used. <b>1:</b> Pore water velocity field in $\text{myr}^{-1}$ . Pore vector linearly scaled to the largest flow arrow. <b>2:</b> salt concentrations in g/L. <b>3:</b> temperature distribution in °C. The rectangle locates a salt diapir flank. Velocity and temperature field within this salt diapir environment are further illustrated in Fig.3-12	62
<b>Fig.3-12:</b> Zoom of thermohaline simulation results in the salt dome environment as located in Fig.3-11 <b>1:</b> Pore water velocity field in $\text{myr}^{-1}$ . Pore vector linearly scaled to the largest flow arrow. <b>2:</b> temperature distribution in °C	64
<b>Fig.3-13: A and B:</b> Mass distribution resulting from mixed convection simulation at $t = 30$ ka and $t = 200$ ka respectively. Salt concentrations are expressed in g/L. Two profiles P3 and P4 are located within the cross-section. The simulation results for these two profiles are shown with no vertical exaggeration in Fig.3-15and Fig.3-16.	66
<b>Fig.3-14: A and B:</b> Temperature distribution resulting from mixed convection simulation at $t = 30$ ka and $t = 200$ ka respectively. Temperatures are expressed in °C. Two profiles P3 and P4 are located within the cross-section. The simulation results for these two profiles are shown with no vertical exaggeration in Fig.3-15 and Fig.3-16.	67
<b>Fig.3-15: A and B:</b> Zoom of the mixed convection results for profile P3 as located in Fig.3-12 at $t = 30$ ka and $t = 200$ ka respectively . No vertical exaggeration is used. <b>1:</b> Pore water velocity field in $\text{myr}^{-1}$ . Pore vector linearly scaled to the largest flow arrow. <b>2:</b> salt concentrations in g/L. <b>3:</b> temperature distribution in °C	69
<b>Fig.3-16: A and B:</b> Zoom of the mixed convection results for profile P4 as located in Fig.3-12 at	70

$t = 30 \text{ ka}$  and  $t = 200 \text{ ka}$  respectively. No vertical exaggeration is used. **1:** Pore water velocity field in  $\text{myr}^{-1}$ . Pore vector linearly scaled to the largest flow arrow. **2:** salt concentrations in g/L. **3:** temperature distribution in  $^{\circ}\text{C}$

**Fig.3.17:** Dynamic viscosity of freshwater as a function of temperature.

**Fig.3.18: A and B:** Mass distribution resulting from mixed convection and viscosity effects at  $t=30 \text{ ka}$  and  $t=200 \text{ ka}$  respectively. Salt concentrations are expressed in g/L. Two profiles P4 and P5 are located within the cross-section. The simulation results for these two profiles are shown with no vertical exaggeration in Fig.3.20 and Fig.3.21

**Fig.3.19: A and B:** Temperature distribution resulting from mixed convection and viscosity effects at  $t=30 \text{ ka}$  and  $t=200 \text{ ka}$  respectively. Salt concentrations are expressed in g/L. Two profiles P4 and P5 are located within the cross-section. The simulation results for these two profiles are shown with no vertical exaggeration in Fig.3.20 and Fig.3.21

**Fig.3.20: A and B:** Zoom of the thermohaline simulation results for profile P4 as located in Fig.3.18 at  $t=30 \text{ ka}$  and  $t=200 \text{ ka}$  respectively. No vertical exaggeration is used. **1:** Pore water velocity field in  $\text{myr}^{-1}$ . Pore vector linearly scaled to the largest flow arrow. **2:** salt concentrations in g/L. **3:** temperature distribution in  $^{\circ}\text{C}$ .

**Fig.3.21:** Zoom of the thermohaline simulation results for profile P5 as located in Fig.3-18 at  $t = 200 \text{ ka}$ . No vertical exaggeration is used. **1:** Pore water velocity field in  $\text{myr}^{-1}$ . Pore vector linearly scaled to the largest flow arrow. **2:** salt concentrations in g/L. **3:** temperature in  $^{\circ}\text{C}$

**Fig.4-1:** Sketch of the geological structure near the uplifted area.

**Fig.4-2:** Large scale model scenario results. Calculated mass distribution at the surface at the end of the simulation run.

**Fig.4-3:** Topography (m) of the reduced model scenario

**Fig.4-4:** Reduced model scenario results. **A:** Calculated patterns at the surface at  $t = 30 \text{ ka}$  and **B** at  $t = 200 \text{ ka}$  respectively. Left: salt distribution (g/L). Right: temperature ( $^{\circ}\text{C}$ ) distribution at the surface. Dotted lines indicate the location of the selected cross-section A-A'.

**Fig.4-5: A)** Geological structure (abbreviations given in Table.1) and finite element mesh of the selected cross-section as shown in Fig.4-4.

**Fig.4-6: 1)** velocity field along A-A' ( $\text{myr}^{-1}$ ) **2)** Profile of salt distribution (g/L), and **3)** temperature ( $^{\circ}\text{C}$ ) resulting from 3D thermohaline simulations at  $t = 30 \text{ ka}$ .(A) and at  $t = 200 \text{ ka}$  (B)



## Acknowledgments

This work would not have been accomplished without the help of many people, whom I would like to thank.

First of all, I would like to thank Prof. Ulf Bayer (FU, Berlin) for his supervision and fundamental support throughout the project. I greatly benefited from his wide experience of numerical modelling and from the fruitful discussions of the results. Thanks to Prof. Asaf Pekdeger (FU, Berlin) who has also supervised this work.

At the same time I am obliged to Prof. Hans Diersch and Dr. Volker Clausnitzer (WASY, Berlin) for the tutorial relating to FEFLOW and the intense exchange of new ideas.

Deep reaching fluid flow group<sup>(\*)</sup> is greatly acknowledged for important contributing. Especially, I would like to thank Christoph Jahnke (BTU, Cottbus) and Dr. Maja Tesmer (FU, Berlin) for making available the data and for the fruitful co-operation during these years of research.

Dr. Magdalena Scheck-Wenderoth has provided the geological data and is acknowledged for her support and help. I thank Dr. Frank Wenderoth for his advises in numerical modelling.

I wish to thank Björn Lewerenz for supplying computer help.

I acknowledge the German Science Foundation (DFG, Germany) for providing financial support via the GeoForschungsZentrum Potsdam.

Thanks to the SPP 1135 team group (Dynamics of Sedimentary Systems under varying Stress Conditions by Example of the Central European Basin System) for the nice meetings around Germany and the interesting workshops.

A sincere “Thank You” to Prof. Brian Horsfield and all colleagues here at the GFZ for the interest showed for my research and for offering a solid work environment. Significant support was also coming from the administrative personnel of the GFZ. Many thanks to Gisela Schmidt at the GFZ library for the speed with which she furnished me with papers and books.

Thank you Yuriy Maystrenko for the nice time we spent sharing the office at the GFZ. Thanks to Dr. Andrew Cavanagh, for the good music, the delicious Scottish salmon and English corrections.

Merci pour tout mon ami Wolfgang Momber.

A warm thank to Katrin Rehak for being near especially in the final stage of the thesis.

Finally, I thank my parents and all my family for their love and support during my studies.

And to whose I have forgotten to acknowledge explicitly: accept both my apologies and thanks!



\*Deep Fluid Working Group: U. Bayer<sup>(1)</sup>, F. Magri<sup>(1)</sup>, V. Clausnitzer<sup>(2)</sup>, H. J. Diersch<sup>(2)</sup>, C. Jahnke<sup>(4)</sup>, P. Möller<sup>(1)</sup>, A. Pekdeger<sup>(5)</sup>, M. Tesmer<sup>(5)</sup>, H. J. Voigt<sup>(4)</sup>

<sup>1</sup> *Geoforschungszentrum Potsdam 4.3, Telegrafenberg, 14473 Potsdam, Germany*

<sup>2</sup> *WASY GmbH, Waltersdorfer Str. 105, 12526 Berlin, Germany*

<sup>3</sup> *Weierstrass Institute for Applied Analysis and Stochastics, Mohrenstr. 39, 10117 Berlin, Germany*

<sup>4</sup> *Brandenburg University of Technology Cottbus (BTU), Environmental Geology, E. Weinert Str. 1, 03046 Cottbus<sup>5</sup>  
Freie Universität Berlin, Institut of Geological Sciences, Geochemistry, Hydrology, Mineralogy, Malteserstr. 74-  
100, 12249 Berlin, Germany*

## Abstract

In several areas of the North East German Basin (NEGB) saline water comes close to or even reaches the surface. Although this phenomenon has been observed during the past two centuries, the origin and mechanisms of brines within the NEGB aquifer are not fully understood. In geothermal systems, the driving forces can be intrinsic to the basin, like thermal variations, and/or external due to hydraulic head. In order to clarify the possible mechanisms of brine transport, thermohaline simulations have been carried for 2D and 3D model scenarios.

For this purpose, a hydrogeological model of the NEGB has been developed which contains the major stratigraphic and hydrogeologic units from the Quaternary to the Upper Permian. In contrast to normal groundwater models for freshwater, large-scale simulation of coupled flow, mass and heat transfer requires a proper fluid density model. Field measurements of pore fluid pressure and temperatures, as well as laboratory investigations of solute content provided density input data. The brine stratification is unstable in the deeper underground suggesting that convective flows are favoured.

The governing equations of density driven flow have been solved by the use of the finite element software FEFLOW 5<sup>®</sup>. The numerical approach of thermohaline simulations has been performed by testing different grid resolutions. The 2D model allows to quantify the interaction between diffusive solute transport, thermally and head-driven flow (forced versus free convection). The main fluid-dynamics of salt migration throughout the NEGB have been inferred from temporal analysis of the transport processes. Additionally, viscosity effects have been taken into account and have been evaluated. Based on these 2D numerical results, a regional picture of the transport processes affecting the NEGB has been tracked down. The 3D regional model (230x330 km) indicates that salt water occurring close to the surface may mainly be driven by hydrostatical forces from the surrounding highlands, describing part of the phenomena. In addition, a smaller 3D scale model (10x10 km) has been constructed with a grid resolution accounting for temperature effects. The results point towards that thermally induced flow, which may play a dominant role in areas with minor topography.

In summary, the complex pattern of near surface occurrences probably results from the interaction of hydrostatic and thermal forces.

Scenarios that allow for mixed convection are needed to understand the mechanism behind numerous previously unexplained field observations of deep-groundwater occurrences near the basin surface. The potential presence of large-scale convection cells has implications both for the fundamental understanding of basin processes as well as for socio-economic issues.

## Zusammenfassung

In vielen Gebieten des Norddeutschen Beckens (NEGB – Northeast German Basin) tritt Salzwasser oberflächennah auf oder erreicht sogar die Oberfläche. Obwohl dieses Phänomen bereits seit zwei Jahrhunderten beobachtet wird, sind der Ursprung und die Mechanismen des Salzwasserflusses im Aquifer des NEGB nicht vollständig verstanden. Die Antriebskräfte in einem geothermischen System wie einem Becken können intrinsisch sein, zum Beispiel thermische Gradienten, und/oder extern sein, zum Beispiel der hydraulische Druckhöhe. Um die Mechanismen des Salzwassertransports innerhalb des Beckens zu klären, wurden für das NEGB thermohaline Simulationen in 2D- und 3D-Szenarios durchgeführt.

Basierend auf einer umfangreichen Datensammlung wurde zu diesem Zweck ein hydrogeologisches Modell des NEGB entwickelt, das die stratigraphischen und hydrogeologischen Haupteinheiten vom Oberen Perm bis zum Quartär beinhaltet. Im Gegensatz zu herkömmlichen Grundwassermodellen für Frischwasser erfordern großmaßstäbliche Simulationen des gekoppelten Fluidflusses, Massen- und Wärmetransfers ein angepasstes Fluidichtemodell. Feldmessungen des Fluidporendrucks und der Fluidtemperaturen sowie Laborexperimente zu Lösungsgehalten liefern die in das Modell eingehenden Dichtedaten. Die Salzwasserschichtung ist im tieferen Untergrund instabil, was darauf hinweist, dass das Auftreten konvektiver Ströme sehr wahrscheinlich ist.

Die Gleichungen des dichtegesteuerten Fluidflusses wurden mithilfe der Finite-Elemente-Software FEFLOW 5 ® gelöst. Der numerische Ansatz der thermohalinen Simulation umfasst Tests verschiedener Gitterauflösungen. Das 2D-Modell erlaubt die Quantifizierung der Interaktionen zwischen diffusem Lösungstransport und thermisch sowie druckhöhegesteuertem Fluidfluss (gezwungene versus freie Konvektion). Die grundlegende Fluidynamik der Salzmigration im NEGB wurde anhand der temporalen Analyse der Transportprozesse ermittelt. Des Weiteren wurden Effekte der Viskosität berücksichtigt und evaluiert.

Basierend auf den numerischen 2D-Ergebnissen wurde ein regionales Bild der Transportprozesse, die das NEGB beeinflussen, erstellt. Das regionale 3D-Modell (230x330 km) zeigt, dass das oberflächennahe Auftreten von Salzwasser hauptsächlich durch hydrostatische Kräfte des umgebenden Reliefs gesteuert wird. Zusätzlich wurde ein kleineres 3D-Modell (10x10 km) mit einer Gitterauflösung konstruiert, die die Temperatureffekte einbeziehen kann. Die Ergebnisse machen deutlich, dass der thermisch induzierte Fluidfluss in Regionen mit wenig Relief ein dominanter Steuerungsfaktor sein kann.

Zusammenfassend ist festzuhalten, dass das komplexe Muster oberflächennahen Auftretens von Salzwasser höchstwahrscheinlich aus der Interaktion von hydrostratischen und thermischen Kräften resultiert.

Gemischte Konvektionsszenarien sind nötig, um die Mechanismen zu verstehen, die zum Auftreten von Tiefengrundwasser an der Beckenoberfläche führen. Der Nachweis und das Verständnis großmaßstäblicher Konvektionszellen hat Auswirkungen sowohl auf das fundamentale Wissen um Beckenprozesse an sich als auch auf sozioökonomische Belange.

# Chapter 1. Introduction

## ***1.1 The North East German Basin: an unexplained large-scale transport system of dissolved halite***

Solute and heat transport in aquifers are studied for their relevance in socio-ecological issues such as energy self-sufficiency and pollution of the environment. An example is the migration of dissolved halite released by salt structures which are commonly found in many geological formations. Subsurface dissolution of salt diapirs is usually invoked to account for the origin of saline groundwater in sedimentary basins (Posey and Kyle 1988; Musgrove and Banner 1993). Eventually, in some discharge areas, these saline waters reach the surface. Several mechanisms may be responsible for driving the heavier saline water up to the surface.

In the last decade, many studies, based on geothermal systems have demonstrated that temperature effects on liquid density can induce convective flows driving different dissolved solutes over long distances. Double-diffusive convection (DDC) is mentioned when the density variations are caused by two factors which have different rates of diffusion. The archetypal example is heat and dissolved salt in water, often referred to as thermohaline convection. In sedimentary basins, many situations in which fluid density varies occur because of changes in salt concentration, temperature and pressure of the groundwater (Cheng 1978; Oldenburg and Pruess 1998; Hanano 1998; Nield and Bejan 1999). Among the multitude of important environmental processes, the transport of pollutants released from waste disposal in salt rock formation (Evans 1989; Van der Lee 2001), saltwater intrusion in exploited coastal aquifers (Kohout 1965; Reese 2003) or salt layers embedded in aquifers (Sarkar et al. 1995) can be mentioned. In all these cases, it is proved that density-driven convection can lead to transport of heat and dissolved salt over large spatial scales and significantly shorter migration time scales than compared with diffusion alone (Straus and Schubert 1977; Straus 1979; Hanor 1987; Simmons et al. 2001; Flocks et al. 2001; Diersch and Kolditz 2002; Simms and Garven 2004). Thermohaline convection in geothermal systems usually occurs together with regional-scale groundwater flow induced by topographic variation. The convective flow regime is then referred to as mixed convection. For instance, in Garven et al. (2001) mixed convection is investigated as a mechanism for deep fluid migration of base metal ores in the McArthur Basin, Australia.

An interesting example of deep fluid flow involving the mentioned processes of halite transport in a geothermal system is provided by the North East German Basin (NEGB). Here the NEGB environmental issues will be briefly introduced.

The NEGB is shown in Fig.1-1. Its area extends over of 330 km x 230 km in the North-South and West-East direction respectively. In different regions of the basin, brackish water reaches the surface locally. This phenomenon is manifested through the occurrence of salty springs or pots. A common characteristic of these saline springs is their temporary and spatially instability. Fig.1-1 illustrates the location of the known saline springs observed in the NEGB (Schirrmeister 1996) together with the distribution of saline groundwater occurring at shallow levels between 0 and 300 m (Grube et al. 2000). The northern and southern basin margins are also depicted. These dashed areas delimit the eroded sediments regions within the study area (denoted as “uplifted”).

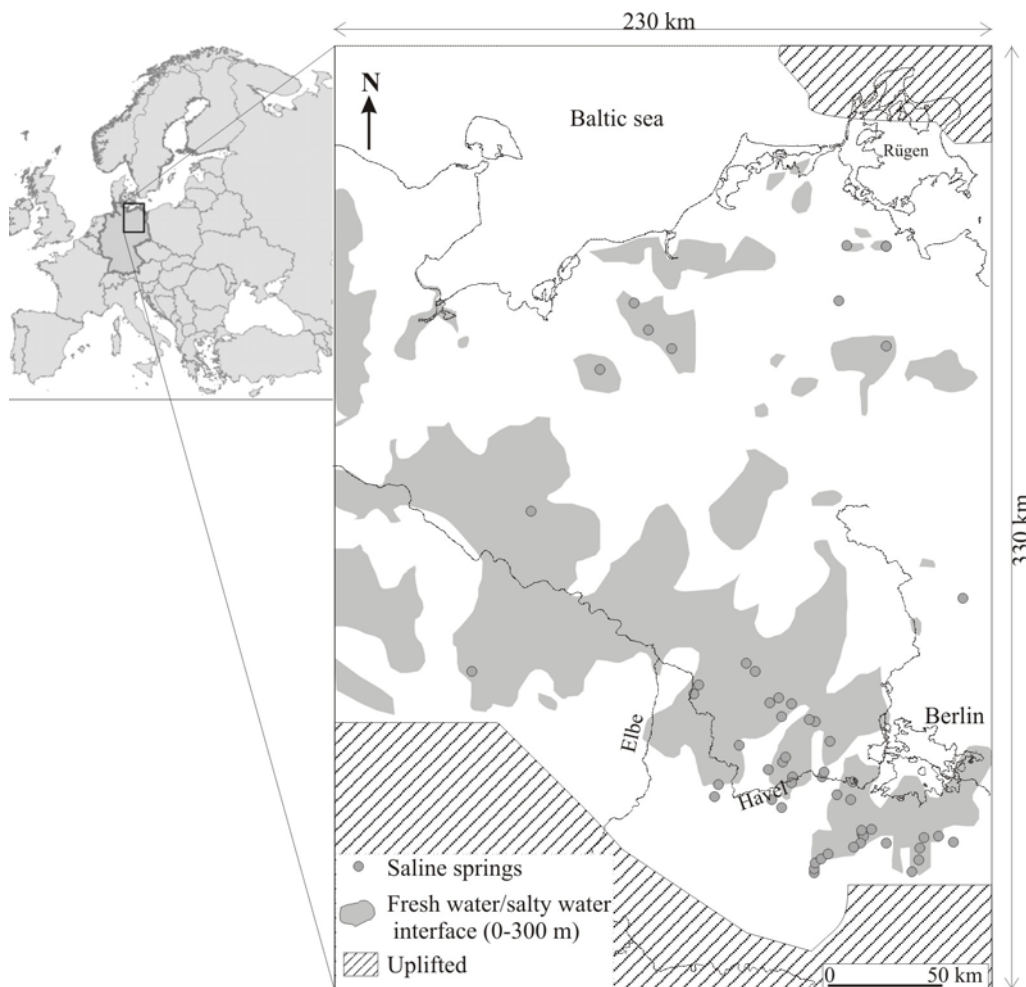


**Fig.1-1:** Study area, location of the observed springs (Schirrmeister 1996) and salty groundwater interface (Grube et al. 2000). The thin sediments area is denoted with “Uplifted”.

From Fig.1-1 it can be seen that the main brine plume of saline groundwater slants across the basin stretching over 250 km from the western part to the south-eastern area near Berlin. In addition, isolated brine formations with an extension in the order of 20 km can be observed in the northern and western part of the domain. The discharge area of brackish waters occurs in the south-eastern part of the NEGB. Presently, the majority of the saline springs are observed in the neighbourhood of the Elbe and Havel rivers and to the south of Berlin. Only few of them are encountered far from these locations.

Further evidence of saline waters is given by plants commonly found along sea beaches or in salty soils, such as seashore salt grass, which grow in different areas of the basin. Fig.1-2 illustrates two species of these plants which have been photographed during a field trip in 2004 in Gröben, 50 km south of Berlin. The spontaneous growth of seashore grass far from the Baltic Sea coast is unusual and signals the existence of highly salty soils in the inner part of the basin.

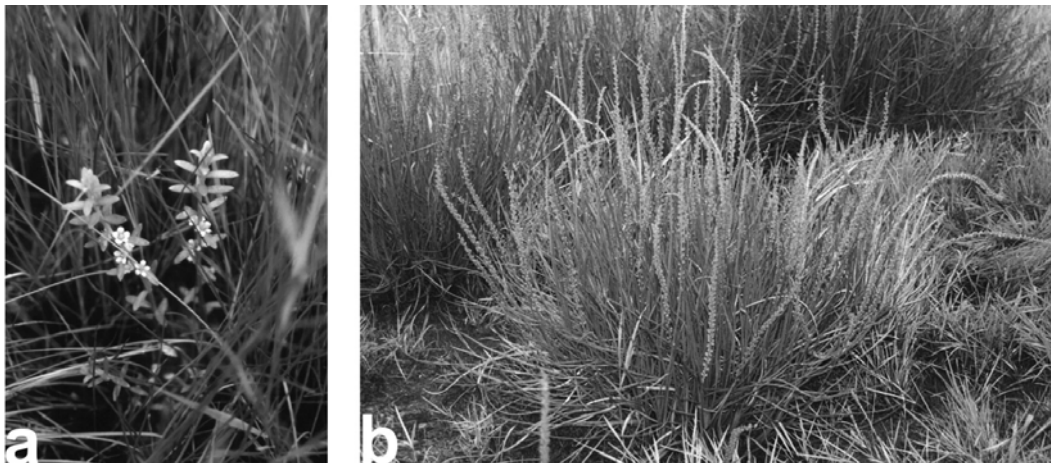


**Fig.1-2:** **a)** *Glaux maritima* (Sea Milkwort, Strand-Milchkraut) and **b)** *Triglochin maritimum* (Sea Arrowgrass, Strand-Dreizack). The pictures were taken during a field trip in Gröben in 2004.

Although these phenomena are observed since two centuries, the origin and mechanisms driving salt in the NEGB aquifer are not fully understood. Heck (1932) listed various locations of saltwater occurrences in Schleswig-Holstein which cannot be related to any shallow salt deposits or salt domes and whose cause remains unknown. A lack of explanation is also noted by Johannsen (1980) for steep vertical plumes of saline fluids reaching near-surface levels in Schleswig-Holstein that.

An important feature of groundwater flow systems within sedimentary basins is that hydrological, thermal and chemical mass transfer are closely coupled. As Chen et al. (1990, p.104) notes, “ Although we tend to think of a single process, it often happens that a variety of

processes are coupled so strongly that qualitatively new effects and system behaviours arise because of this coupling”. Numerical modelling represents a powerful investigation tool which can provide new insights into basin fluid dynamics resulting from the strongly coupled transport processes. For instance, previous coupled heat and fluid transport simulations based on the NEGB (Clausnitzer et al. 2001; Bayer et al. 2002) suggested that the thermal anomalies, due to the presence of salt domes in the basin, may force local up-welling of deep-seated water in specific locations. However, this hypothesis needs further testing by recognizing salt effects on fluid density that were ignored in the models.

Therefore the main goal of the thesis will be to numerically investigate thermohaline convective flows in the NEGB in order to provide fundamental informations on the unknown mechanisms that lift deep salty groundwater to near-surface.

## **1.2 Data: aquifer and fluid model**

Large scale simulation of coupled fluid flow, mass and heat transport based on real geothermal system requires a proper aquifer and fluid model. This is necessary because of the high spatial variability of the physical and chemical properties of the geological strata and the fluid. Therefore the input database must include:

- spatial aquifer characteristics (“aquifer model”), i.e. layer geometry, lithologies, and physical parameters of the different aquifers such as porosities, permeabilities, heat conductivity and heat capacity,
- chemical and physical fluid characteristics and their spatial distribution (“fluid-model”), i.e. water salinity, chemical components and fluid density.

In order to supply these input data, an integrated approach is applied. This method involves geological studies, field measurements of pore fluid pressure and temperatures, chemistry as well as laboratory investigations of solution properties and solutes content.

This research is part of a joint project between the Frei Universität of Berlin (FU), the Brandenburgische Technische Universität of Cottbus (BTU) and the GeoForschungsZentrum Potsdam (GFZ). Hydrochemical analyses were performed at the FU by Maja Tesmer and interpreted in collaboration with Peter Möller (GFZ) while fluid properties were derived at the BTU, Cottbus, by Christoph Jahnke.

In the next paragraphs, particular attention will be given on the available data of the NEGB system with regard to the aquifer and the fluid model. The state and the processes of

fluid migration in the NEGB will be described on the basis of these dataset in order to yield a regional picture of the dominating processes and to derive input data and control parameters for the numerical simulation.

### 1.2.1 Database and sampling locations

In order to improve the database, the ‘grey’ (unpublished) literature existing at the Geological Surveys of the federal districts of Germany and at commercial companies has been evaluated and organized in a digital database by Christoph Jahnke, BTU. This database contains lithological and petrophysical data, hydrochemical, hydraulic, and geothermal data from about 500 deep boreholes within the study area from Cretaceous to Permian/Carboniferous as well as several thousand datasets from superficial Cainozoic aquifers. The data are mostly from the 1960s to the 1980s. Fig.1-3 (left) illustrates the sampling location of the aquifer parameters. The data provided by Christoph Jahnke include stratigraphic and lithological logs, geophysical/petrophysical logs, data of reservoir tests and analysis of core material which provide input data for the physical parameters of the different stratigraphic units. The sampling location of the data for fluid chemistry and dynamics of saline waters (from Cenozoic to Paleozoic) are shown in Fig.1-3 (right).

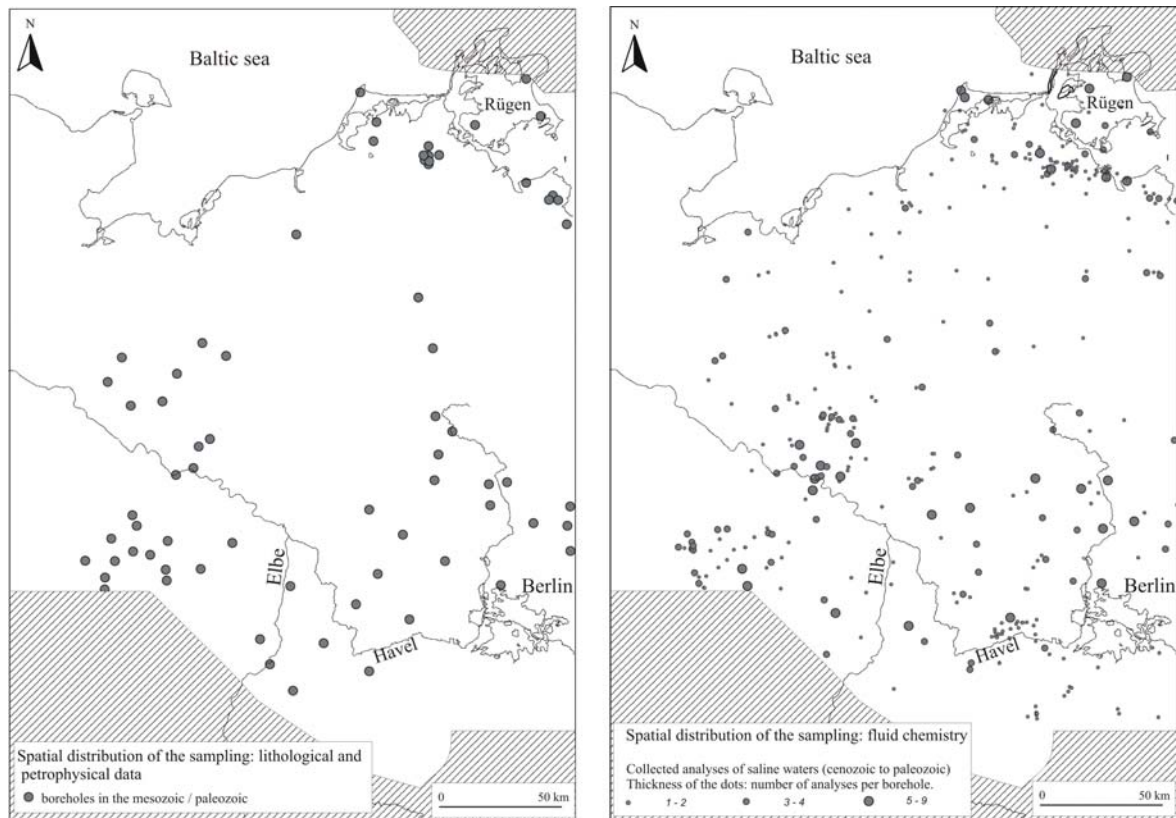


**Fig.1-3:** Sampling locations for the lithological and petrophysical data (**left**), and for the chemistry and dynamics of deep and saline fluids (**right**). (provided by C. Jahnke, BTU)



These data include chemical analyses of fluids as well as measurements of fluid pressures, hydraulic heads and temperatures which provide indication on the origin and dynamics of salt migration. The available data for fluid chemistry and dynamics are mainly clustered at the centres of the former oil and gas exploration activities and represent a good sampling distribution over the entire study area (in the north: Rügen and Barth-Grimmener structure; in the south-east: Lausatia; in the west: Altmark region).

### 1.2.2 Aquifer model

The incorporated geological data are derived from a three-dimensional structural model of the NEGB (Scheck 1997; Scheck and Bayer 1999). The area covered by the model is approximately 230 x 330 km in the horizontal extension and 30 km in the vertical direction which consists of 13 layers of the sedimentary fill. Figure 1-4 illustrates the relief of the Top Zechstein Salt derived from the geological input data. The NEGB is affected by intense salt tectonics. Thick salt diapirs pierce more than 4 km of overlying Mesozoic and Cenozoic strata. Salt crests can also be found 500 m below the surface level. Therefore depth and thickness of sedimentation sequences vary strongly within the basin.

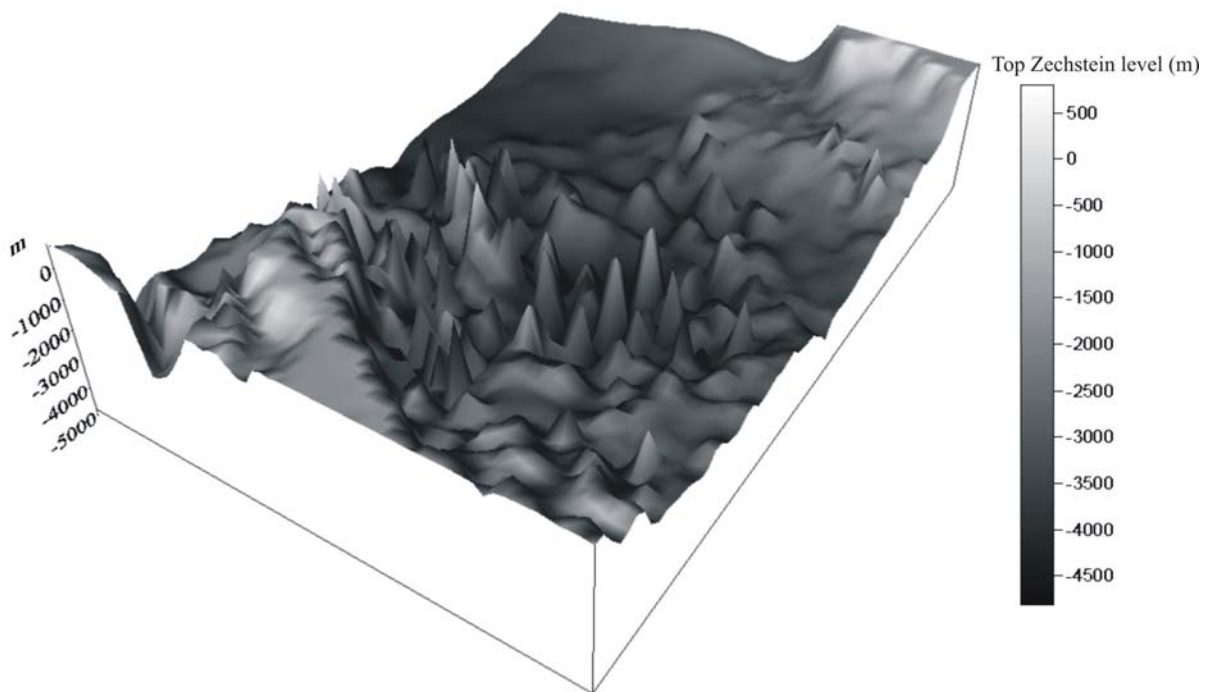


**Fig.1-4:** Relief of the Top Zechstein derived from the geological input data (Scheck 1997; Scheck and Bayer 1999).

The physical parameters of the sedimentary layer are those given by Scheck (1997, Tab.1). The physical properties considered within each layer are constant. This first rough aquifer model differentiates only the stratigraphic layers of the model without any spatial variation. The development of a detailed aquifer model with spatial variations of porosities, permeabilities, etc., corresponding to the collected petrophysical data is the aim of further research. Furthermore, local faults are not included.

By comparing the hydraulic permeability of the Muschelkalk with those of the younger sediments (Tab.1-1), it turns out that the value is five orders less than the average. Therefore it can be inferred that this stratigraphic formation behaves as a quasi-impervious unit. The Muschelkalk is mainly dominated by fine grained carbonates. Particularly, in the central part of the basin it contains evaporitic layers of salt rock up to some decametres with very low permeabilities. This impervious unit leads to a separation of the Post-Permian strata in two aquifer systems with different hydrochemical and hydrodynamical characteristics (from Lower to Upper Buntsandstein and from Keuper to Cretaceous).

Layer	Abbreviations	Permeability	Porosity	$\rho_s$	Heat capacity	Heat conductivity
		[m <sup>2</sup> ]	[--]	[kg/m <sup>3</sup> ]	[J/(kg*K)]	[J/(K*m*s)]
Cenozoic	Cz	1.e-12	0.23	2670	1180	1.5
Upper Cretaceous	K <sub>1</sub>	1.e-13	0.10	2400	1000	1.9
Lower Cretaceous	K <sub>2</sub>	1.e-13	0.13	2700	1180	2
Jurassic	J	1.e-13	0.13	2700	1180	2
Upper Triassic	T <sub>2-3</sub>	1.e-14	0.06	2700	1180	2.3
Middle Triassic	T <sub>2</sub>	1.e-18	0.00	2400	1000	1.85
Lower Triassic	T <sub>1</sub>	1.e-14	0.04	2670	1180	2
Zechstein (Salt)		1.e-30	~0.0	2160	840	3.5
Elbe Group		1.e-14	0.03	2670	1000	1.84
Mirrow Formation		1.e-14	0.03	2670	1000	2.13
Volcanics		1.e-14	0.03	2670	1000	2.4
Top basement		1.e-30	~0.0	2650	930	2.5
Top mantle		1.e-30	~0.0	2700	1000	2.65

**Table.1-1 Physical parameters assigned to the stratigraphic layers.**

From the geological model some considerations concerning its influence on regional flow in transporting solute within the NEGB can be inferred. Fig.1-5 (left) illustrates the topography of the top Zechstein Salt which has been derived from the geological input data (Scheck 1997) together with the distribution of saline groundwater (depicted with shaded patterns) as shown in Grube et al. (2000). Grey filled circles locate the position of the observed springs (Schirrneister 1996). In Fig.1-5 (left), dark patches show the occurrence of salt domes while light grey areas are associated with thin deeper salt pillows. From an analysis of Fig.1-5, no obvious spatial correlation between salt structures and near surface salt occurrences can be inferred. Brine patterns can also be found far away from salt dome crests. This observation already suggests that the regional groundwater flow plays an important role in driving solute. This hypothesis is further supported by comparing the distribution of saline groundwater with the topography of the NEGB as illustrated in Fig.1-5 (right). Although the topography variation is low, it can be seen that the main brine pattern stretches in the lowland along the rivers systems. Nevertheless, some salty plumes can also be observed in regions far from this area suggesting that regional flow, induced by topography, is not the only process transporting solute within the basin.

### ***1.2.3 Fluid model: fluid chemistry and density model***

#### **Fluid chemistry**

The hydrochemistry of deep saline waters in the Northern German Basin was investigated by Glander and Schirrneister (1975), Hoth et al. (1997), Hannemann and Schirrneister (1998), Huenges (2002), Kühn (1997), Lehmann (1974a, 1974b), Löhnert et al. (1986), Müller and Papendieck (1975), Naumann (2000), Neumann (1975), Rockel et al. (1997), Rutter (1988), Thomas (1994), Trettin et al. (1990, 1997), Voigt (1972, 1975, 1977). These studies focussed on subjects such as geochemistry, geothermal energy, oil field waters, isotopes, and environmental aspects and thus will not be discussed in detail here. Hannemann and Schirrneister (1998) concluded that the waters of the springs waters originated mainly in the deeper Pre-Tertiary sub-ground. The steep rising plumes observed in Schleswig-Holstein point to possibly significant temperature effects on the fluid density in addition to any existing forced convection. An overview is given in Grube et al. (2000).

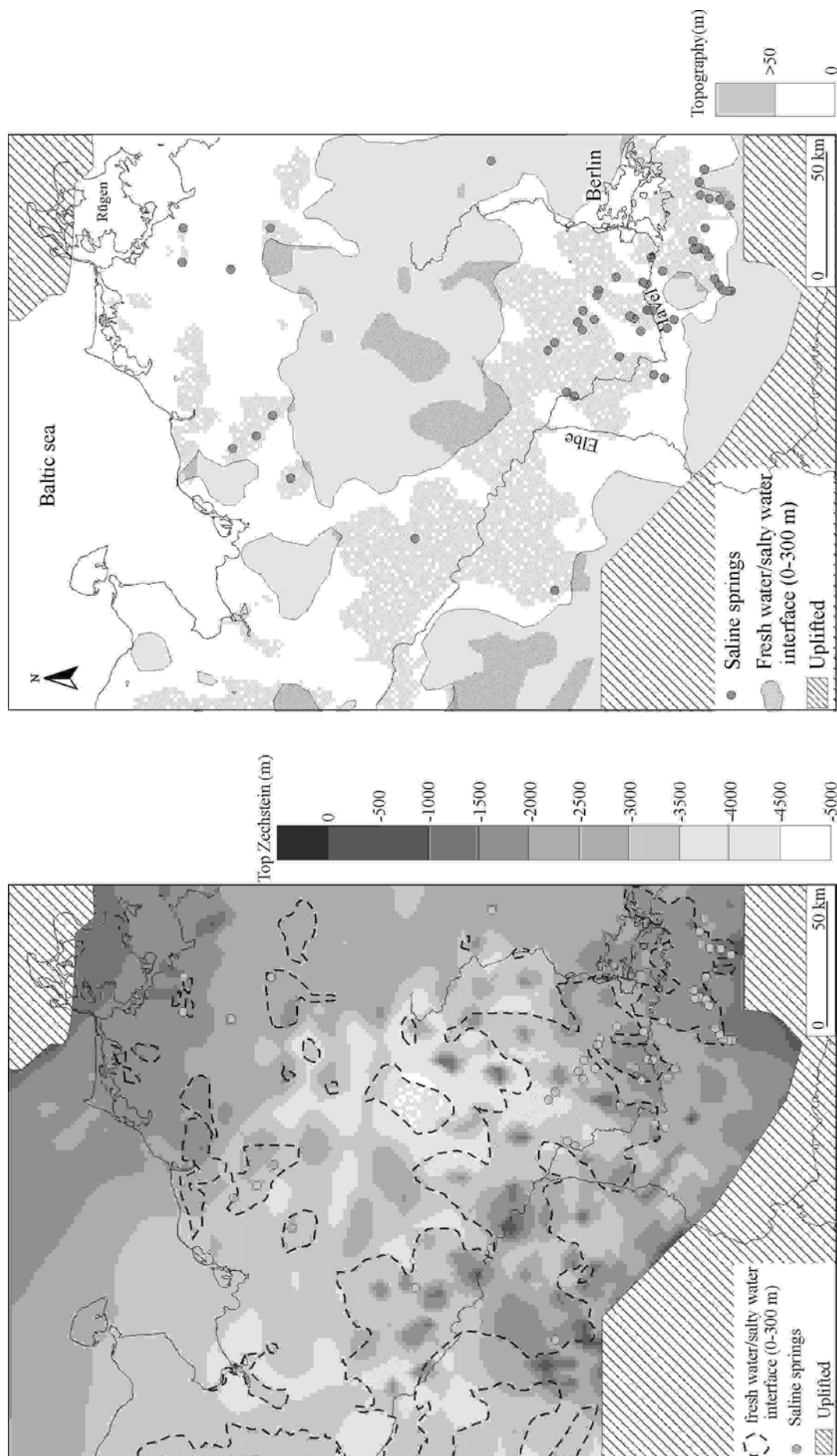


**Fig.1-5. Left:** Top Zechstein depth map (Scheck 1997), location of the observed springs (Schirmer 1996) and salty groundwater interface (Grube et al. 2000). **Right:** NEGB topography (Scheck 1997), location of the observed springs (Schirmer 1996) and salty groundwater interface (Grube et al. 2000).

The chemical data have been analysed for major and minor ions,  $^1\text{H}/\text{D}$  and  $^{16}\text{O}/^{18}\text{O}$  by Maja Tesmer (FU). In addition, new investigations on brine chemistry have been performed. At each location, samples for anions and cations, Rare Earth Element and Yttrium (REY),  $\delta^{18}\text{O}$ ,  $\delta\text{D}$ , and  $\text{SiO}_2$ -geothermometer have been sampled. Where no former analyses for  $^{34}\text{S}/^{32}\text{S}$  -,  $^{13}\text{C}/^{12}\text{C}$ - and  $^3\text{He}/^4\text{He}$  – isotope ratio and tritium existed, new samples for these isotopes have also been taken. Samples have been stored at  $4^\circ\text{C}$  and full water analysis has been generally performed as soon as possible. Sampling and analyses followed the directives of DVWK (1992), DIN (1986). A description of stable isotopes can be found in Meyer et al. Meyer et al. (2000) and for REY in Möller et al. (2003). REY analyses have been normalized by C1-Chondrite.

From the hydrochemistry analysis it emerges that the groundwater salinity increases with depth in the NEGB. Fig.1-6 illustrates the depth salinity trend of groundwater samples in relation to the different stratigraphic units. Salinity is expressed in mg/l of Total Dissolved Solids (TDS).

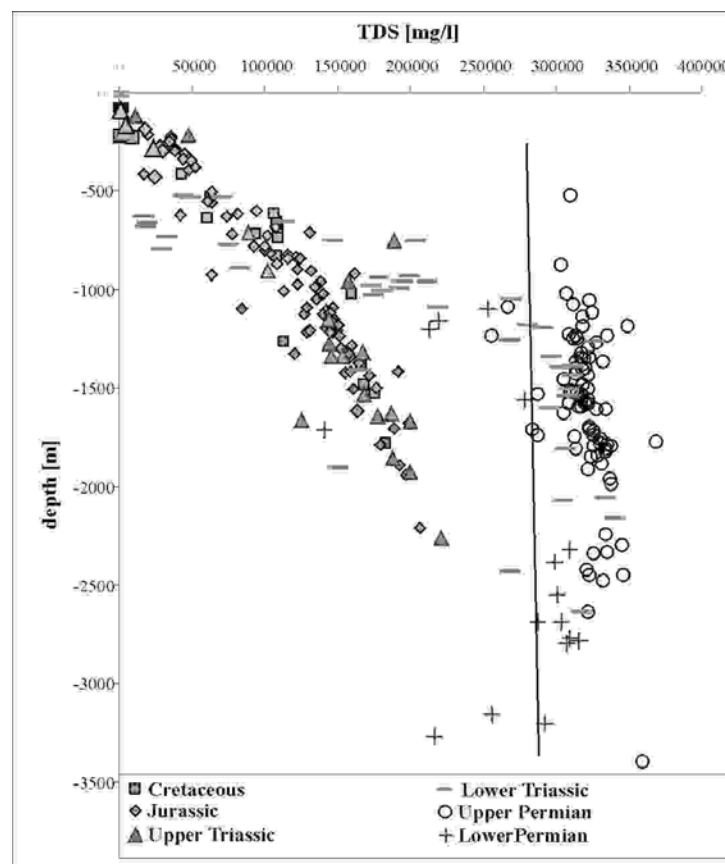


**Fig 1-6:** Depth-salinity trend of the groundwater samples in relation to the stratigraphic units of the NEGB (provided by M. Tasmer, FU Berlin).

From this figure it can be inferred that a salinity-depth dependency can be assumed for groundwaters belonging to the stratigraphic units from Cretaceous to Upper Triassic (Keuper). On the other hand, the salinity of Permian and Lower Triassic waters are depth independent showing that a saturation level of approximately 345 g/L is reached.

Cluster analyses have been performed by Maja Tesmer (FU, Berlin) to separate hydrochemically different population. Two main hydrochemical groups have been thereby distinguished. A first group consists of nearly pure NaCl waters. Salinity of this type of groundwater predominantly originates in dissolution of halite. This statement is further supported by recent data findings. In the second group, hydrochemical diversity is much higher since cation composition is not restricted to  $\text{Na}^+$ , but is also affected by  $\text{Mg}^{2+}$  and  $\text{Ca}^{2+}$ . On the other hand the overall dominant anion is always  $\text{Cl}^-$ .

Stable isotope content has been used to get a deeper insight into processes of groundwater salinity while from REY pattern the movement of groundwater between aquifers can be deduced. These chemical data interpretations were carried out by Maja Tesmer (FU) and P. Möller (GFZ). More details can be found in Tesmer et al. submitted). Isotopic contents show that all groundwater samples were built by infiltrating waters, although climatically different recharge conditions were encountered. In general, isotopic contents increase with salinity and depth below -500 m.

For aquifer systems above this level no salinity dependency can be inferred. Therefore mixing processes between waters built under recent or Pleistocene recharge conditions and waters built in warmer periods are supposed to reach this depth driven by topography-induced flow. Interaquifer flow is proven by the REY patterns, especially for shallower aquifer systems. REY patterns additionally prove that even at depth lower than -1500 m interaquifer flow is possible and can be assumed to be ascending.

In summary, chemistry analysis results point toward the main source of salinity from halite dissolution. Salt content increases with depth until it reaches a saturation point estimated around 345 g/l. Isotopic contents indicate that the regional groundwater flow affects the water cycle down to a depth of at least -500 m. REY patterns show the existence of communicating aquifers characterized by upward brine flow.

### **Fluid density**

In geothermal systems temperature and pressure effects on fluid density must be taken into account. Since these influences were neglected in former investigations, fluid density data needed in situ temperature and pressure corrections. The latter have been performed by Christoph Jahnke (BTU).

Fig.1-7 illustrates the density/depth relation in the different pre-Cenozoic aquifers. Approximate density/depth relations were fitted by Christoph Jahnke to the experimental data for the Cretaceous to Keuper, Buntsandstein and Zechstein (Fig.1-7a, b, c respectively). The density values are obtained from laboratory analyses and approximated in-situ densities. In each picture, the square dots represent the density values obtained from laboratory analysis measured at room temperature. The interpolated average trend is then illustrated by the grey line. The approximated in-situ densities is distinguished by the bold black line. For the determination of the in-situ densities a temperature and pressure correction of the laboratory data was performed. For this purpose an iteration procedure was carried out. Based on the assumption of a simple temperature model and hydrostatic conditions, temperature-corrected densities and pressures were calculated. The temperature model considers only a depth dependency of the temperature (no spatial variations). A thermal gradient of 35 °C/km was assumed for the Mesozoic strata corresponding to geothermal data (Hurtig 1994).

For the Cretaceous to Keuper (Fig.1-7a) the laboratory and in-situ values show a general increase of the fluid density with depth however, with wide scattering. On the other hand, in the Buntsandstein (Fig.1-7b), once NaCl saturation is reached the densities remain nearly constant at about 1220 g/dm<sup>3</sup>. At approximately -1.5 km depth the NaCl saturation is reached and at laboratory conditions the density remains close to 1220 g/L. The corrected density/depth temperature relation indicates that the density decreases with increasing depth after saturation has been reached. The inversion of the density/depth trend is due to the thermal expansion of the fluid: at saturation depth, temperature effects are dominating and increase the brine volume which leads to a decrease of its density. Accordingly, the fluid density stratification is unstable and promotes convective flows. Within the Cretaceous to the Keuper this effect may also occur but at depths below 3.500 m. In the Zechstein Salt (Fig.1-7c) the laboratory values indicate that the fluid saturation level is already reached (i.e. the density value is close to 1120 g/L independently of depth). The corrected density/depth temperature relation shows the same inversion trend already observed in the Buntsandstein.

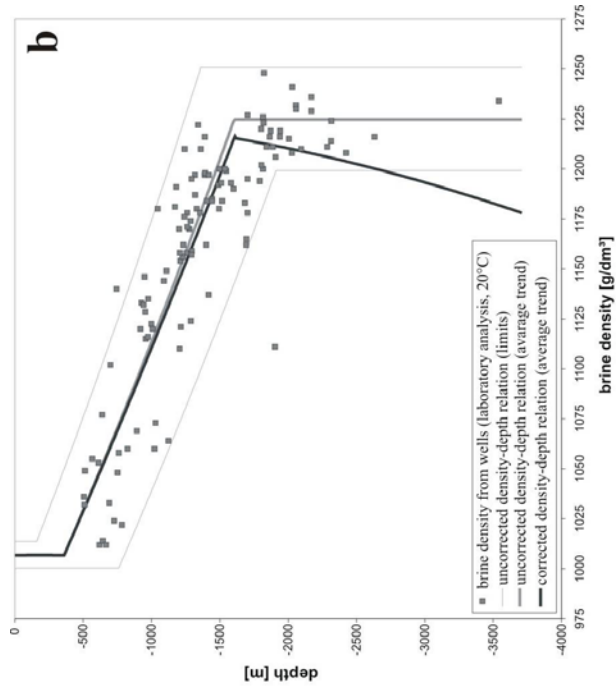
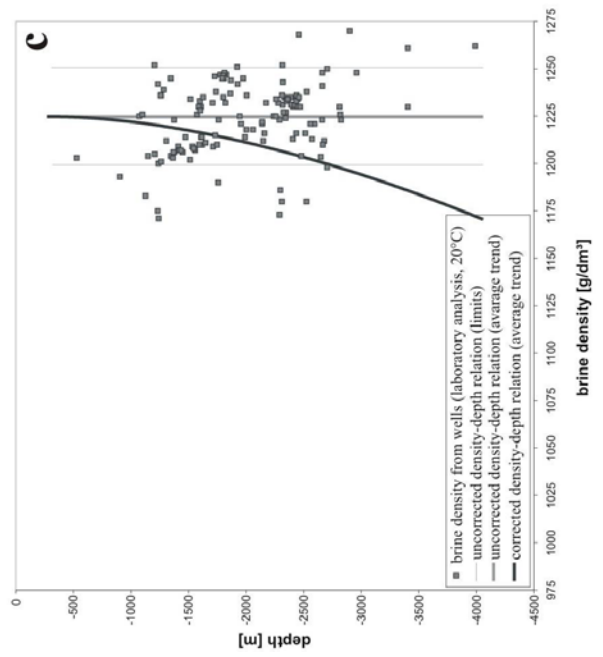
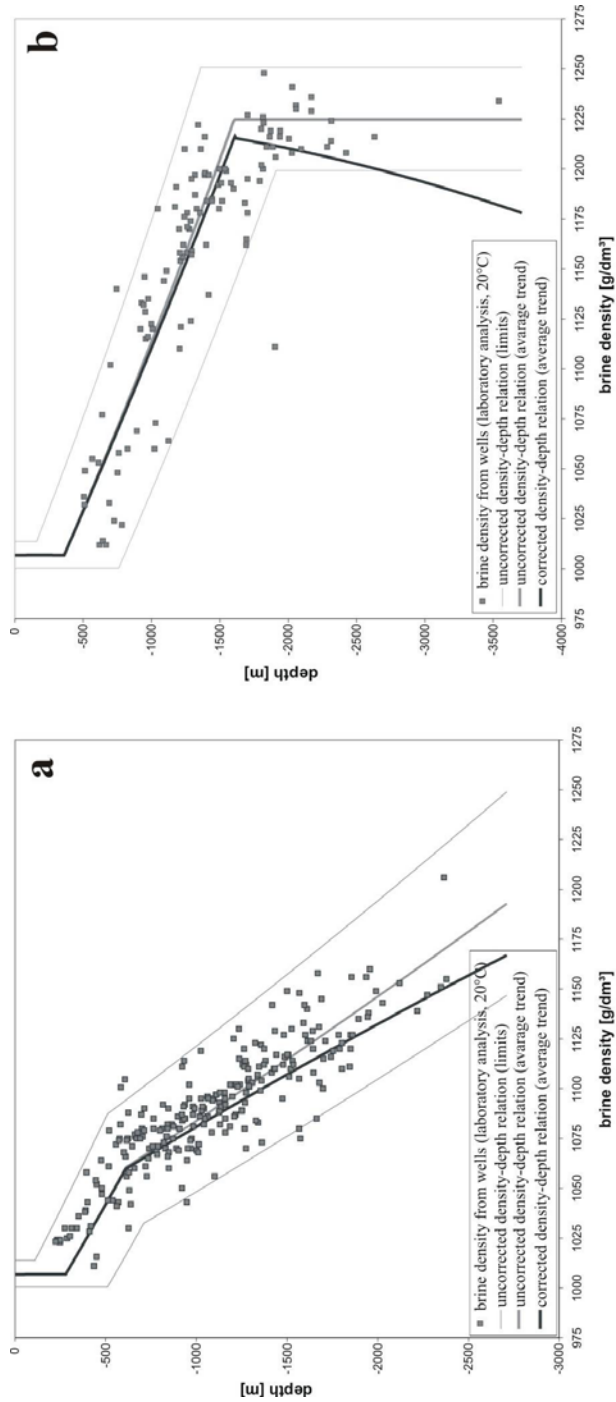
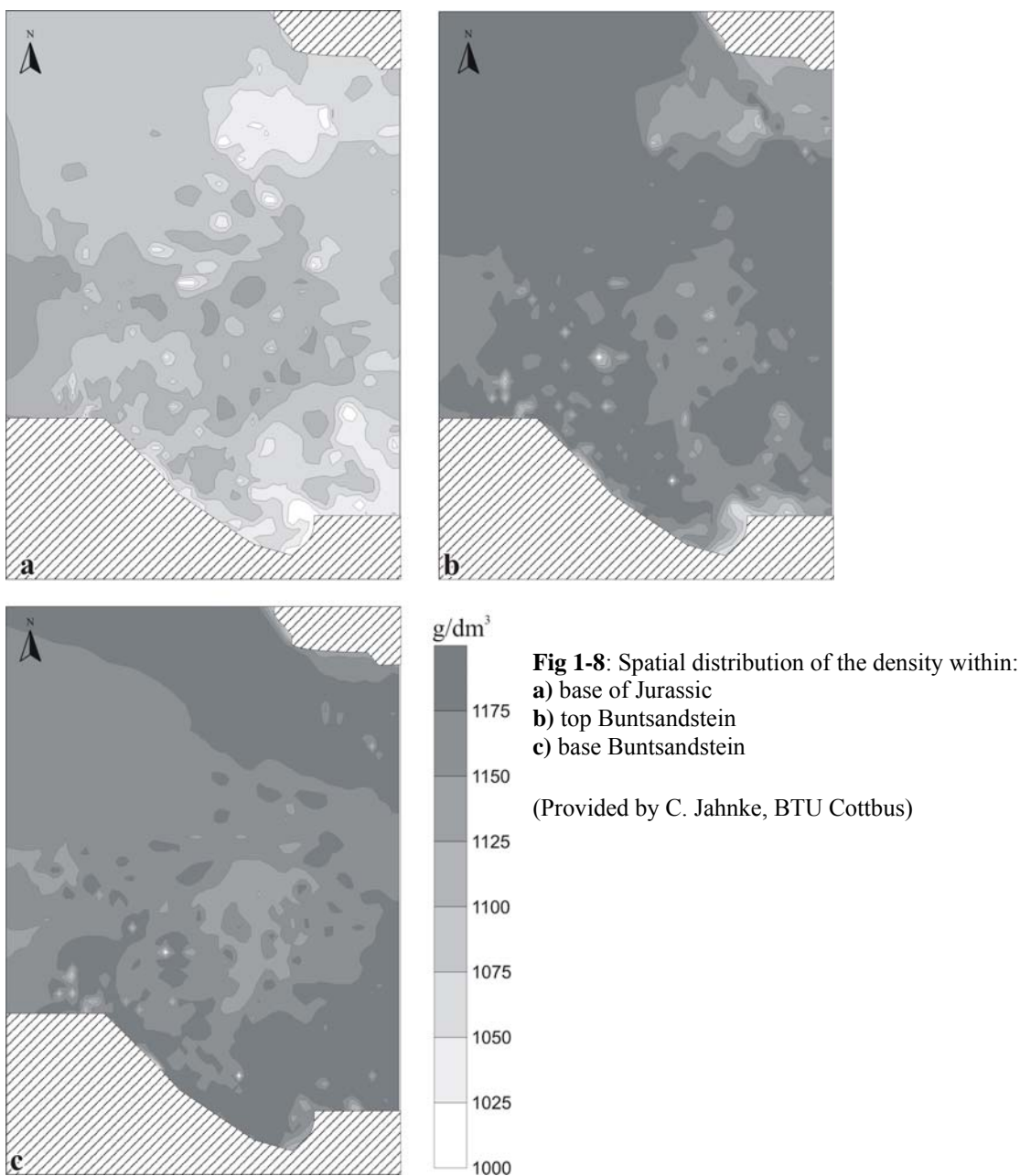


**Fig. 1-7:** T-p corrected in-situ brine densities for the stratigraphic units  
 (a) Cretaceous-Keuper  
 (b) Buntsandstein  
 (c) Zechstein  
 (Provided by C. Jahnke, BTU Cottbus)

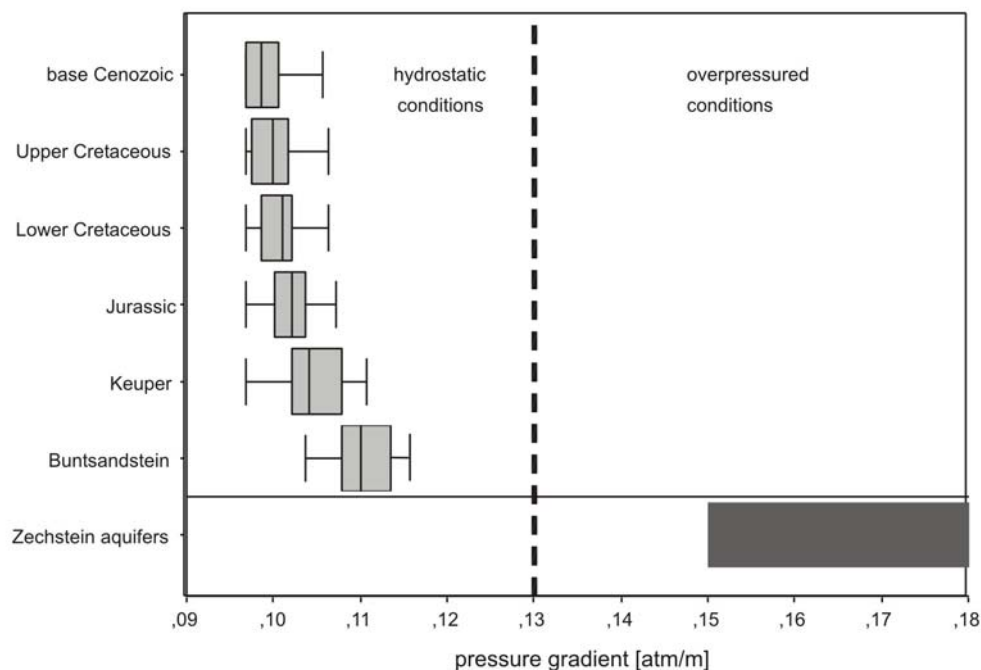


Fig.1-8 provides an overview about the spatial distribution of the density in some subsurface aquifers. For the Cretaceous to Keuper the density increases from the borders of the basin towards its centre, paralleling depth. The base of Jurassic shows also this typical trend (Fig.1-8a). Spatial deviations exist due to salt diapir occurrence. The Top Buntsandstein, however, shows a very different behaviour (Fig. 1-8b). At lower depth the density increases from the border to the centre due to an increase of salt content. Once NaCl saturation is reached, the density decreases according to the temperature effect. Therefore, the centre of the basin contains fluids with lower density surrounded by a ring of denser waters. This effect becomes stronger with depth and it is more distinctive at the base of the Buntsandstein (Fig.1-8c).



In summary, the density data point toward a profile sensitive to temperature variations and an unstable condition in the deepest stratigraphic units. Consequently, it can be presumed that thermal buoyant effects are among the major driving forces eventually generating convective flow. Moreover the regional variable density stratification is also unstable and can lead to upward fluid flow depending on the permeabilities of the aquifers.

Fig.1-9 illustrates the pressure gradients within different stratigraphic units of the NEGB. The horizontal intervals depicted in Fig. 1-9 represents the hydrostatic pressure ranges. The pressure gradients above the Zechstein were derived from in situ-densities and correspond well to experimentally obtained data from hydraulic tests (Neumann 1975; Voigt 1975; Rutter 1988). In all stratigraphic units above the Zechstein the pressures are hydrostatic. Therefore the aquifers above the Zechstein can be considered intercommunicating and inter-aquifer flows can occur. Pressures above the hydrostatic level arise only in the Zechstein and in some local zones in the Rotliegend (Voigt 1975).



**Fig 1-9:** Corrected pressure gradients in the different stratigraphic units of the NEGB. (Provided by C. Jahnke, BTU Cottbus)

### **1.3. Discussion and approaches**

The data provide a regional picture of the dominating processes affecting solute transport within the NEGB as well as input parameters for the numerical simulations. The influence of a topography-induced flow regime on salt migration is supported by observations considerations and by isotopic content analysis. These hydrochemical analysis indicate that the regional groundwater flow affects the water cycle down to a depth of at least -500 m. Furthermore the REY patterns highlighted the existence of upward directed inter-aquifer flow even at depth below -1500 m. Therefore intrinsic basin-system mechanisms must exist to exceed the gravity field that would keep dense salt-laden waters in deep seated aquifers. Hydrostatic pressures arise in all stratigraphic units above the Zechstein, suggesting that ascending flows are not due to the existence of any over-pressured aquifers. On the other hand, the fluid density analysis proved that temperature effects lead to a highly unstable density stratification in which denser fluids overly lighter fluids. Consequently thermally induced convective flows are likely favoured. In summary, the data point toward mixed convection.

The data allow to make some preliminary assumptions for the numerical simulations. In the numerical model the brine can be considered pure NaCl solution resulting from halite dissolution. The saturation concentration of the fluid is reached at 345 g/L of dissolved halite which corresponds to a brine density of 1220 g/L. Furthermore, topography-induced flow and fluid density variations described in 1.2.3 must be incorporated.

The thesis will supply insight on the dynamic aspects of geothermal reservoir such as the interaction of the structural setting, the thermal field and fluid-dynamics within the different strata of the basin.

Since this research is centered on the understanding of the system dynamics rather than the development of modelling tools, the strongly coupled non linear equations governing thermohaline convection in porous media will be solved by the use of the commercial Finite Element (FE) program FEFLOW<sup>®</sup> (Finite Element subsurface FLOW system), WASY GmbH (Diersch 2002).

Thermohaline simulations of different conceptual models of the NEGB shall provide a sufficiently deep understanding of the physics and the numerical modelling of non-linear transport in a given geological system. Moreover, an adequate modelling strategy will be helpful to identify numerical problems and to develop stable numerical solutions.

Finally, using the experience from a stable 2-D model, an effort in building a 3-D model will be made.

This thesis is an attempt to describe in detail the steps taken to tackle the problem.. This applicative work shall present the computational modelling of convective dynamics in the NEGB by undertaking the following steps:

- Integration of the NEGB digital structural model and its related physical parameters by use of FEFLOW<sup>®</sup>. From this 3-D structural and physical model, a representative 2-D vertical cross-section of the basin will be obtained.
- The transient thermohaline simulations will comprise:
  - 1) The implementation in FEFLOW of an appropriate equation of state for the density brine that takes in account the effect of pressure, heat and salt.
  - 2) Stability analysis of the non-linear coupling process by testing different finite element grids.
  - 3) Testing an alternative set of boundary conditions with the attempt to reproduce observed data.
  - 4) A successful strategy in developing numerical stable solutions will be tracked down and the computed results will be analysed in order to highlight which factors and geological units allow or prevent convective flow within the basin.
- The 2-D modelling approach will yield fundamental informations concerning the limits and expenses of large scale numerical simulation of density driven fluid-flow with regards to mesh resolution. The knowledge acquired from these 2-D simulations will be used for numerically modelling 3-D thermohaline convection in the NEGB.

For this purpose two different FE mesh are applied:

- 1) A first rough numerical model scenario will be defined on the whole studied area.
- 2) A highly refined grid resolution will be applied on a reduced part of the model.

Finally the results of the simulations will be summarized and discussed.



## **Chapter 2. 2D thermohaline approach: model scenario and preliminary simulations**

In this chapter the available NEGB structural model (Scheck 1997) will be integrated in the FEFLOW database. Then a representative cross-section of the basin will be obtained from this three dimensional structural model and used as model scenario for the 2D thermohaline simulations. In order to approach numerical simulations of coupled fluid flow, mass and heat transfer, based on the NEGB, a proper grid resolution has to be defined. The preliminary numerical simulations described here are aimed to build up a finite element mesh suitable for the thermohaline problem.

### ***2.1 Definition of the two-dimensional model scenario for thermohaline simulations by use of FEFLOW®***

#### ***2.1.1 The need of a two-dimensional approach***

The basic problems in solving the coupled non-linear equations of fluid flow, heat and mass transport are due to numerical instabilities which arise during the simulation process. Numerical thermohaline simulations based on real geothermal systems are hindered by the highly deformed mesh geometry resulting from the complex geological structure. Consequently, a certain degree of mesh refinement is required in order to solve the density-dependent problems (Gresho and Sani 2000; Diersch and Kolditz 2002). However, mesh refinement increases the numerical complexity of the problem. Moreover, the different spatially varying physical parameters involved in the equations, provide additional difficulties in solving the thermohaline flow problem. Transport phenomena in sedimentary basin are controlled by the spatial variation in heterogeneous conductivity fields (Dagan 1989). As discussed by Simmons et al. (2001) heterogeneity of hydraulic properties can even perturb flow over regional length scales and generate instabilities especially in systems where density stratifications are encountered. These considerations summarize the major drawbacks concerning the numerical approach for thermohaline flow in geothermal system. In summary, from a numerical point of view, the complicated geometry of the basin fill, together with the

heterogeneity of physical parameters, and fluid density variations lead to self-perturbing natural systems.

Although fluid flow and transport processes in sedimentary basins occur in a three-dimensional environment, the study of a two-dimensional thermohaline problem is necessary in order to obtain more details with regard to numerical features of the non-linear coupled system. In a vertical profile ( $x,z$ ) the number of independent spatial variables of the problem is reduced by one degree of freedom. Therefore a highly refined mesh can be defined in a cross-section model scenario by use of much less active nodes. Consequently the computational time decreases drastically. This allows to estimate a proper cell dimension for thermohaline flow simulation. Once the model robustness is achieved it is possible to define proper boundary conditions in order to reproduce observed data.

Therefore, the 2D approach provides a series of advantages in successfully tracking down a simulation-based method for developing stable solutions with regard to the given geometrical (structural) resolution, the physical equations and the numerical approximation. The method then can be used to tackle a three-dimensional thermohaline model scenario.

In order to create a cross section of the NEGB, with all spatial and physical characteristics preserved, the three-dimensional structural model of the basin had to be integrated into FEFLOW.

### **2.1.2    *Integration of the structural model of the NEGB into FEFLOW®***

FEFLOW is a software conceived for the modelling of flow and/or transport processes in natural porous media. FEFLOW has been chosen for this study for several reasons. The code is based on the Finite Element technique and it is one of the few commercial softwares which can handle two-dimensional and three-dimensional thermohaline flow. The finite element method is suitable for defining grids which can be easily adapted to the complicated structure of a sedimentary basin such as the NEGB. Moreover FEFLOW offers a Geographic Information System interface (GIS) whereby data integration and regionalization can be applied. These components ensure an efficient working tool in building the finite element mesh, integrating structural model data, and assigning model properties.

The first step for building the numerical model scenario is to define a so called superelement. The superelement delimits the horizontal extension ( $x,y$  direction) of the 3D finite element mesh within the working window of FEFLOW. For constructing the finite element mesh, the grid resolution has to be defined within the superelement. The discretized





The actually implemented model consists of the first eight layers of the given geological model (from Top Cenozoic down to the base Zechstein Salt) and of an additional slice located at 5 km depth, acting as the model basement. This picture emphasizes the highly complicated structure of the layers especially in salt domes and uplifted areas. In Fig. 2-1, the finite element mesh used to define the top slice of all layers is shown for the topography. Each model slice consists of 4071 (59 x 69) rectangular elements. The 3D finite elements used to discretize the whole basin volume are eight-nodes quadrilateral prisms. Since 9 layers have been incorporated, the total number of 3D finite elements is 36639 corresponding to 42000 active nodes. In Fig. 2-1 a sketch of a 3D finite element representing a salt dome area is depicted. In this particular setting, finite elements are highly distorted since the height of the elements can drastically vary within few kilometres.

The physical parameters of all stratigraphic units, given in Tab. 1-1, can be stored in the FEFLOW database by assigning each layer the related parameter value. At this point the available 3-D structural model of the NEGB and the physical parameters are fully adapted to the simulation program. Cross-section modelling scenarios can be created from the 3-D structural model simply by taking a vertical profile through the structural model along a surface line as depicted in Fig. 2-1. The resulting cross-section will comprise the finite element mesh as well as the different physical parameters of each layer. In the next paragraph the selected representative cross-section will be described.

### **2.1.3    *The representative NEGB cross-section***

Two-dimensional investigation of thermohaline flow in the NEGB basin requires the choice of a proper model scenario. Indeed, as mentioned in the previous chapter, in the NEGB there is some topographical variations and particular geological structures such as salt pillows and diapirs. At a regional scale, topographical variations induce regional flow that can enhance hydrodynamic mixing and affect solute transport in the shallow aquifer. The steep flanks of the salt diapirs can further induce gravitational driven flow, also referred to as non-Rayleigh convection (Bjorlykke et al. 1988). Moreover, because of the high thermal conductivity of salt diapirs the temperature fields can be strongly disturbed favouring thermally induced flow and salt dissolution (Evans and Nunn 1989). Therefore, topographical variations and salt-tectonic structures must be comprised in the cross-section in order to gain insights in their interaction with other fluid-dynamics, affecting solute transport within the basin. Additionally the vertical profile must cross areas where observed data, such as salty plumes and saline springs

are observed. A cross-section in which all these features are comprised can be considered as a “good” or representative 2D model scenario for the NEGB.

In Fig. 2-2 (a) the location of the cross-section is shown on the NEGB topography together with the salty groundwater distribution (Grube et al. 2000) and the observed saline springs (Schirrmeister 1996). From this figure it can be seen that the chosen cross section slices the study area along the whole West-East basin extent. The cross-section cuts the main regions where topographical variations arise as well as a wide area of salty groundwater plumes. Some of the observed saline springs are located along the profile. The cross section does not intersect the uplifted area delimited by the southern margin since this region corresponds to eroded layers where fluid flow and mass transport play a minor role.

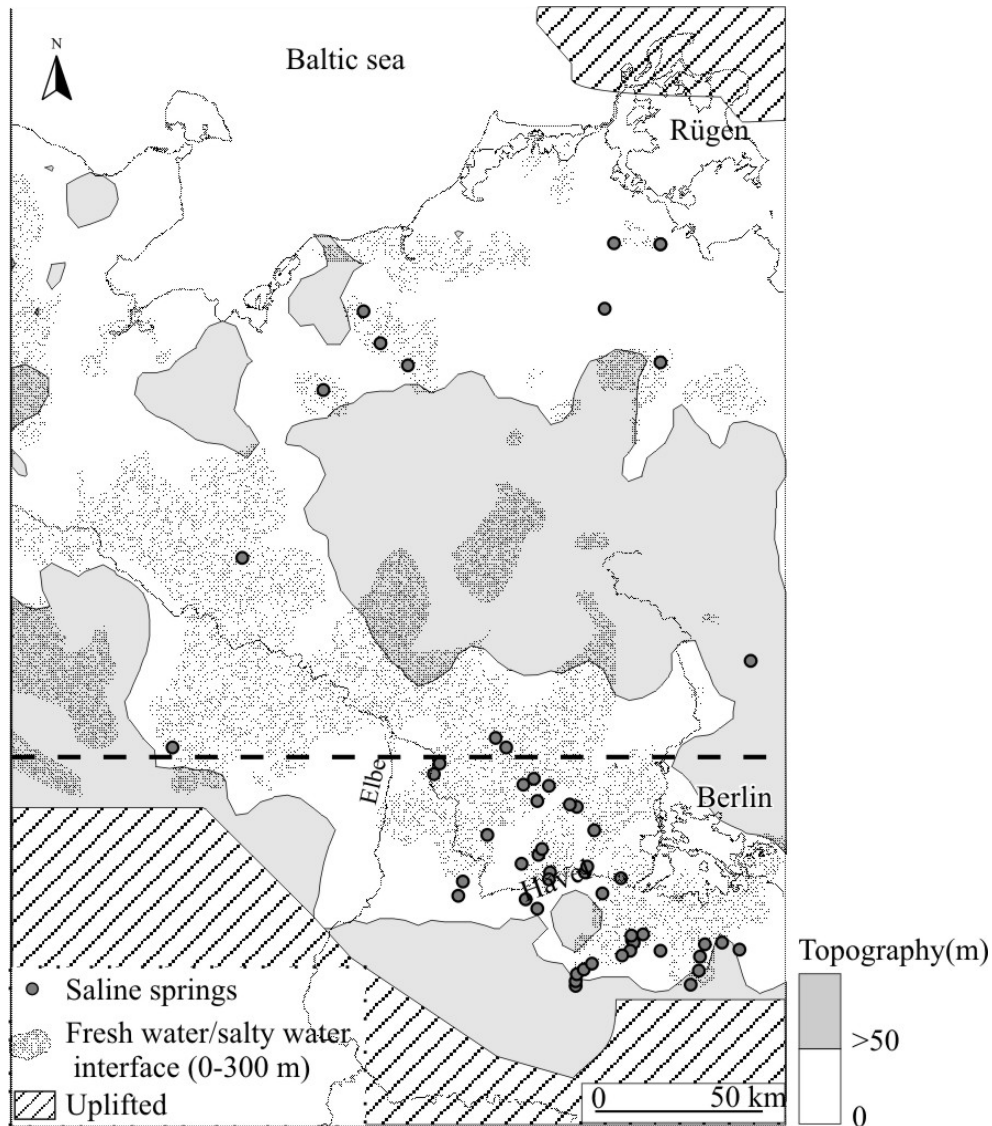


**Fig. 2-2 a:** Location of the 2D cross-section together with the fresh/salty water interface and saline springs as shown in Fig. 1-5

Fig. 2-2 (b) illustrates the geological structures of the chosen cross-section. Shallow salt-structures are comprised within the resulting profile area.

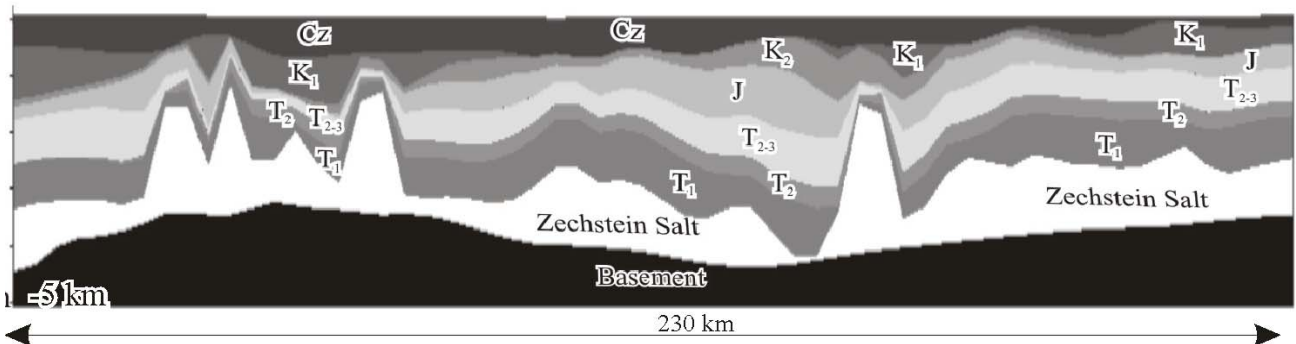


**Fig. 2-2 b:** Stratigraphic units of the 2D cross-section. The stratigraphic unit abbreviations are given in Tab. 1-1.

This cross section will be used as a representative model scenario for carrying out thermohaline simulations based on the NEGB as described in the next chapters. According to the geological features, the cross-section will allow to test and identify the different flow regimes within the NEGB (forced versus free convection). This purpose can be achieved only by use of a numerically stable solution. Therefore an adequate grid refinement will be essential in order to define a cell resolution which resolves short wavelength interactions of the coupled system. A robust 2D finite element mesh will be defined in the next paragraph by performing preliminary transient thermohaline simulations

## **2.2. Preliminary 2D thermohaline simulations**

### **2.2.1. Governing equations and assumptions**

The governing equations of thermohaline convection in a saturated porous media are derived from the conservation principles for linear momentum, mass and energy (e.g. Bear 1991; Kolditz et al. 1998; Nield and Bejan 1999). A description of the equations and parameters can be found in Appendix 1. The resulting system is fully implemented in FEFLOW and is briefly reported here by the following set of differential equations (ref. Appendix 1: Eq. 1.2; Eq. 1.5; Eq. 1.9; Eq. 1.16)

$$S_0 \frac{\partial \varphi}{\partial t} + \text{div}(\mathbf{q}) = Q_{\text{Boussinesq}} \quad (2.1)$$

$$\mathbf{q} = -\mathbf{K} \text{grad} \left( \varphi + \frac{\rho_f - \rho_{0f}}{\rho_{0f}} \right) \quad (2.2)$$

$$\frac{\partial \phi C}{\partial t} + \text{div}(\rho_f \mathbf{q} C) - \text{div}(\mathbf{D} \text{grad}(C)) = Q_C \quad (2.3)$$

$$\frac{\partial}{\partial t} \left( (\phi \rho_f c_f + (1 - \phi) \rho_s c_s) T \right) + \text{div}(\rho_f c_f T \mathbf{q}) - \text{div}(\lambda \text{grad}(T)) = Q^T \quad (2.4)$$

Eq.(2.1) is the equation of fluid mass conservation.  $S_0$  is the medium storativity which physically represents the volume of water released (or added to) from storage in the aquifer per unit volume of aquifer and per unit decline (or rise) of head  $\varphi$ .  $Q_{\text{Boussinesq}}$  is the Boussinesq term which incorporates first order derivatives of mass-dependent and temperature-dependent compression effects.  $\mathbf{q}$  is the Darcy (or volumetric flux density) velocity defining the specific discharge of the fluid. The Darcy's law is expressed by Eq.(2.2) where  $\mathbf{K}$  is the hydraulic conductivity tensor. Eq.(2.3) is the equation of solute mass conservation where  $\phi$  is the porosity of the porous medium,  $C$  is the mass concentration,  $\mathbf{D}$  is the tensor of hydrodynamic dispersion and  $Q^C$  is a mass supply. Eq.(2.4) is the energy balance equation of the fluid and the porous media.  $c_f$  and  $c_s$  is the heat capacity of the fluid and solid respectively,  $T$  is the temperature,  $\lambda$  is the thermal conductivity of the saturated porous medium as a whole.

From Eq.(2.1) and Eq.(2.2) it can be seen that FEFLOW uses a hydraulic head-formulation. This approach is usually preferred since it allows more convenient formulations of boundary conditions and parameters relations for shallow aquifers.

As mentioned in Appendix 1, constitutive and phenomenological relations of the different physical parameters involved in the equations are needed to close this coupled system. Here the hydraulic conductivity relation and the Equation Of State (EOS) for the fluid density are recalled (see Appendix 1 for details):

$$\mathbf{K} = \frac{\mathbf{k} \rho_{0f} g}{\mu_f(C, T)} \quad (2.5)$$

$$\rho^f = \rho_0^f \left( 1 - \bar{\beta}(T, p)(T - T_0) + \bar{\gamma}(T, p)(p - p_0) + \frac{\bar{\alpha}}{C_s - C_0}(C - C_0) \right) \quad (2.6)$$

The hydraulic conductivity tensor  $\mathbf{K}$  is related to the reference fluid density  $\rho_{0f}$ ,  $g$  is the gravitational acceleration,  $\mathbf{k}$  is the tensor of permeability,  $\mu_f(C, T)$  takes into account the

fluid viscosity effects due to temperature and concentration variations. The EOS for the fluid density is related to the reference temperature  $T_0$ , pressure  $p_0$  and concentration  $C_0$ ,

Eq.(2.6).  $\bar{\alpha}$  is the mass concentration ratio,  $\bar{\beta}$  is the coefficient of thermal expansion and  $\bar{\gamma}$  is the coefficient of compressibility.

The flow and transport equations (Eq.(2.2), Eq.(2.3), Eq.(2.4)) for thermohaline convection are non-linear and strongly coupled since temperature and salinity control the fluid density  $\rho^f$  and dynamic viscosity  $\mu_f$ . The variation of fluid density is essential for the modelling of thermohaline convection because of its primary importance for calculating the correct buoyant force included in the equation of motion (i.e. generalized Darcy's law Eq.(2.2)). Fitted polynomial expressions are commonly used for temperature, pressure and salinity dependences of the fluid density (Sorey 1976). In order to reproduce the density model described in paragraph 1.2.3, all the mentioned dependences are accounted for FEFLOW. For this purpose, two polynomial expressions which accurately represents the coefficient of thermal expansion  $\bar{\beta}(T, p)$  and compressibility  $\bar{\gamma}(T, p)$  for the fluid density (Eq.(2.6)) have been derived and coded as an extension to the simulation program. A detailed description of these polynomial functions and the implemented code is reported in Appendix 2 and Appendix 3 respectively. The method has been approved by WASY and can also be found in Magri (2004). As seen in the paragraph 1.2.3, the density of the saturated brine is 1220g/L. The fluid density  $\rho_f^0$  is referred to freshwater conditions and set equal to 1000 g/L.

Therefore the density ratio  $\bar{\alpha} = \frac{\rho_f^s - \rho_f^0}{\rho_f^0}$ , appearing in Eq.(2.6), is set equal to 0.22.

Since the main goal of this chapter is the definition of a robust 2D finite element mesh a number of simplifying assumptions are required.

No coefficient of mechanical dispersion is included in the dispersive flux of the solute. This means that the coefficient of hydrodynamic dispersion  $\mathbf{D}$  appearing in Eq.(2.3) is equal to the molecular diffusivity of solute in the saturated porous medium  $\mathbf{D}_{\text{diff}}$  (Eq.(1.6) Appendix 1). In the specific case, such simplification may introduce differences in the resulting solute field (Nield 1974; Rubin 1975)). The mechanical dispersion takes into account the structure of the porous medium. As described in Appendix 1, the mechanical dispersion causes the flow streamlines to divide in the longitudinal direction. Consequently, this additional spreading enhances solute mixing with freshwater and the resulting fluid density differences become smoothed. Therefore, in the case where no coefficient of mechanical dispersion is considered

the solute field will be less homogenous and more saline. Nevertheless, as proved in Rosenberg and Spera (1992), neglecting the coefficient of mechanical dispersion does not affect the basic character of the fluid dynamics of the system. Therefore, this simplifying assumption will also be used for the thermohaline simulations described in the next chapter.

Another approximation which will be considered henceforth is the so called Oberdeck-Boussinesq approximation OB. The OB approximation consists in neglecting the density dependences included in the term  $Q_{\text{Boussinesq}}$  in the LHS of the fluid balance equation (Eq.(2.1) and explicitly detailed in Eq.(1.43), Appendix 1), i.e.  $Q_{\text{Boussinesq}} = 0$ . Kolditz et al. (1998) evaluated the OB approximation for different convection problems. Their studies proved that the differences in the concentration field resulting from the OB approximation on a long term simulation are negligible and the fluid-dynamics is not affected.

Additionally, fluid viscosity is considered constant and referred to freshwater conditions. Viscosity effects on the flow regime will be evaluated only on a robust thermohaline model. In the next chapter the concentration and temperature dependences of viscosity will be incorporated in the thermohaline simulations. Other fluid properties such as heat capacity and conductivity are considered constant.

To complete the set of differential equations defining the thermohaline problem appropriate initial and boundary conditions for the hydraulic head, the temperature and the concentration must be defined.

### **2.2.2. Boundary and initial conditions**

The boundary conditions used in this preliminary thermohaline approach are first and second type boundary conditions. A set of boundary conditions which can reproduce observed data such as mass and temperature distribution at the surface can be defined once a suitable grid for thermohaline flow is built. The boundary conditions used here are schematically illustrated as follows (Fig. 2-3 A.):

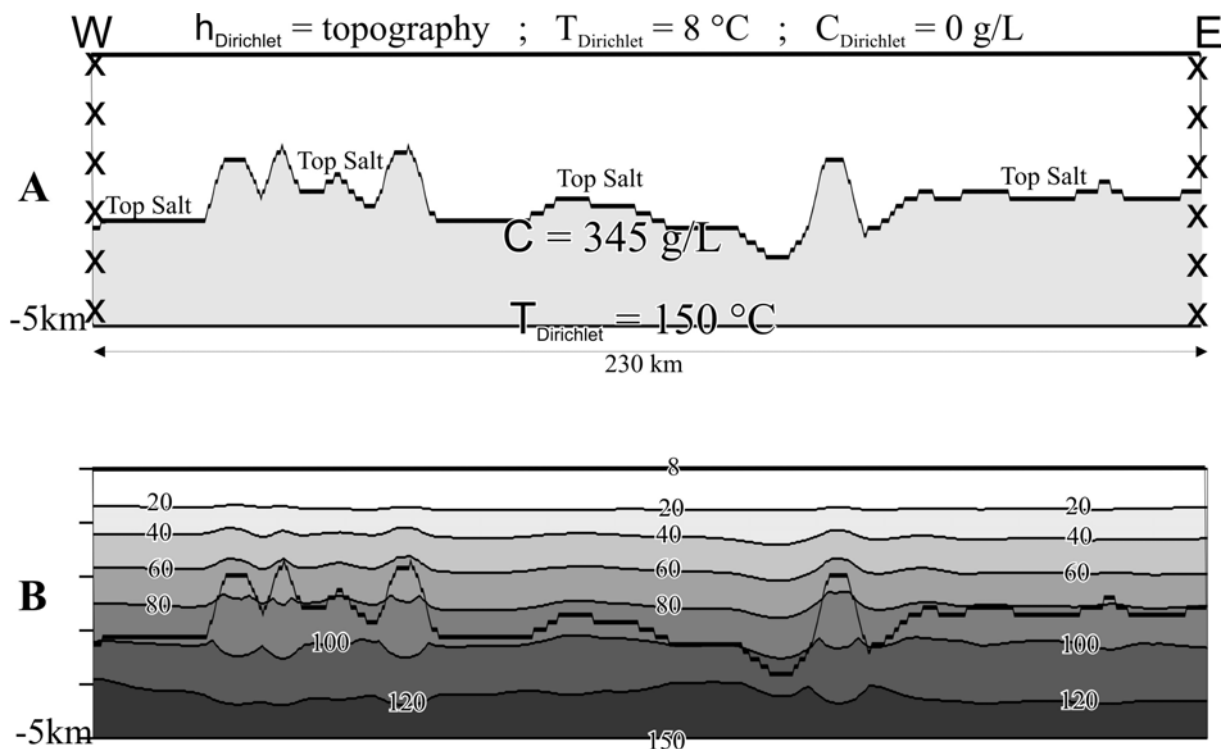


**Fig.2-3: A:** Boundary conditions of the preliminary thermohaline simulations and, **B:** Initial temperature distribution (°C) derived from a steady-state heat transport problem. The bold line delimits the Top Salt. Temperature values have been interpolated with a Kriging gridding method by use of the commercial software Surfer 8.

- At the surface the hydraulic head, fluid temperature and concentration have to be defined. The head is set equal to the topographical elevation. The fluid temperature and concentration values are fixed to 8°C and 0 g/L respectively.
- At the Top Salt a fixed concentration value of 345.2 g/L has been set. As seen in the paragraph 1.2.3 this value corresponds to the saturation concentration of the fluid at the depth of interest. Even though salt dissolves with time and produces brine, the shape of the salt layer does not change. In their study, Ranganathan and Hanor (1988) made a similar assumption for salt domes.
- At the basement a constant temperature boundary condition is defined. The value is set to 150 °C which corresponds to a linear vertical gradient of 30 °C/km.
- The lateral boundaries are closed to fluid, heat, and mass flow.

The simulation of transient flow requires a priori knowledge of physically meaningful initial conditions, which can be obtained from a steady-state calculation of the problem or from the interpolation of observed data. Initial conditions derived from observed data introduce perturbations to the parameters field which immediately initializes high numerical instabilities. Therefore the numerical system will need a large number of time steps for calculating the solution and in some cases will not converge at all.

On the other hand, using initial conditions derived from steady-state solutions of the considered problem guarantees a higher stability of the simulations and increases the rate of convergence of the coupled equations (Ortega and Rheinboldt 1970). Nevertheless, obtaining steady state solutions for coupled nonlinear systems as in the thermo-convective case is in most cases impossible. Therefore, the initial pressure and temperature distributions are obtained from the numerical solution of uncoupled steady-state fluid flow and heat transport models. The resulting pressure profile is not disturbed, it is hydrostatic. In order to calculate the initial temperature distribution, the hydraulic conductivity value of each layer has been set close to 0. Therefore the resulting temperature profile is purely conductive. The initial temperature field prescribed for the thermohaline simulations is illustrated in Fig. 2-3B. For presentation, the temperature values have been interpolated with a Kriging gridding method by use of the commercial software Surfer 8. This figure illustrates the well-known thermal anomalies around salt domes. Concave isothermal lines are associated with the salt domes whereas above these structures the isothermal lines are convex. Such anomalies are due to the high thermal conductivity of the salt domes with regard to the thermal conductivity of the surrounding sediments.

The initial salt concentration is homogenous and set to fresh water condition (0 g/L) everywhere above the Top Salt.

### ***2.2.3. Numerical and time step schemes***

As mentioned in paragraph 2.1.1, the physical perturbations which arise during the simulation of thermohaline flow are caused by heterogeneous physical parameters which are encountered in all hydrothermal systems. Additionally, strong buoyancy forces together with steep gradients dramatically trigger the numerical instabilities of the system. These instabilities, also referred to as wiggles, are manifested by negative values of nonnegative properties such as fluid density or concentration. Wiggles have a numerical nature. They signal that the gradients are insufficiently resolved by the mesh. As a result, numerical errors are generated. In density plume problems the perturbations created by the propagation of these numerical errors are virtually uncontrollable (Schincariol et al. 1994). To prevent such wiggles an extremely refined mesh is required. Unfortunately, such a grid resolution cannot be achieved at the basin-scale ( $1 \times 10^2$  km) with regard to the computational power of the available software and hardware. The numerical compromise is the use of a full upwind scheme. This



numerical scheme introduces a balancing tensor diffusivity term to stabilize the solution. This is equivalent to an increase the coefficient of molecular diffusivity  $\mathbf{D}_{\text{diff}}$  appearing in Eq.(2.3) according to Diersch and Kolditz (2002):

$$\mathbf{D}^{\text{num}} = \mathbf{D}_{\text{diff}} + \frac{v\Delta l}{2} + o(\Delta l^2), \quad (2.7)$$

where  $v$  is the fluid pore velocity and  $\Delta l$  the characteristic element length. Such numerical diffusion (or artificial dissipation) is represented by the second term in the right hand side of Eq.(2.7),  $\frac{v\Delta l}{2}$ . From this relation, it can be inferred that the physics of the problem is highly changed if a too coarse mesh (i.e., large  $\Delta l$ ) is used. At large  $\Delta l$  an overestimated numerical diffusion will be introduced and will govern the whole transport process. Therefore the resulting over-dispersive smoothing will overwhelm thermally buoyant induced flow. Consequently no temperature effects on the flow regime can be taken into account. Particular attention must be made in defining a correct space gridding that prevents the upwinding scheme to introduce dominant over-dissipative terms.

Transient simulation of convective processes also requires proper time schemes. Here a predictor-corrector time integrator (Gresho and Sani 2000) advances the balance equations in time. Specifically, the second order Trapezoid Rule scheme (TR) with automatically controlled time-stepping is used. This scheme has been proved to be an accurate strategy especially for strong nonlinearities (Diersch and Kolditz 1998). At each time step a convergence tolerance factor directly controls the time-step size. If the error estimates do not violate the constraints, the time step is increased, otherwise the time-step is reduced. Fig.2-4 illustrates the adaptive time scheme strategy. More details about this temporal discretization can be found in the WASY white papers (WASY-GmbH 2002).

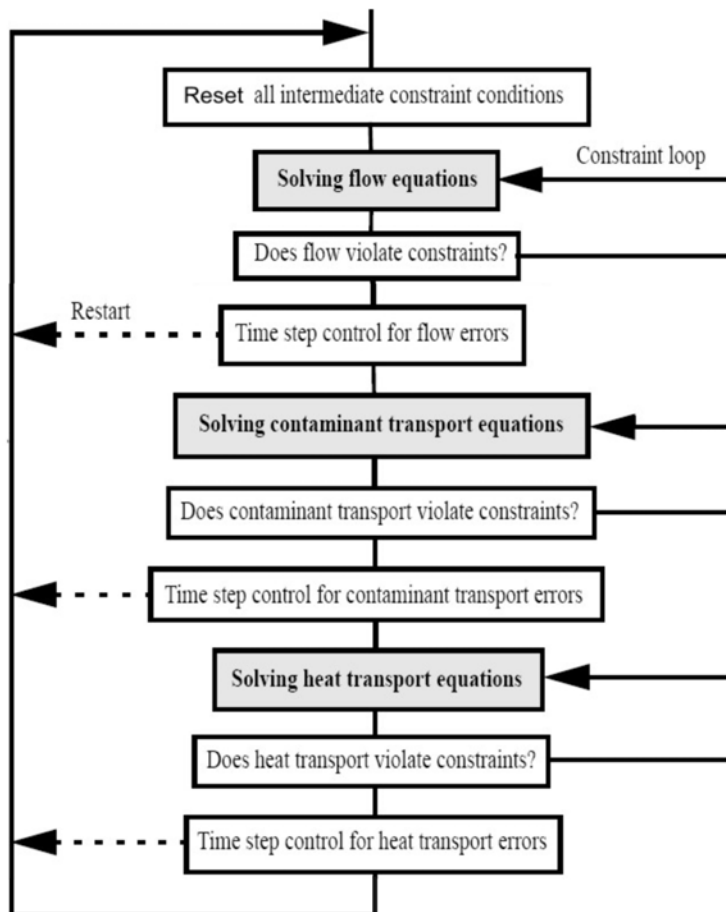


**Fig.2-4:** Adaptive time scheme strategy for coupled transient flow, mass and heat transport.(Modified from Diersch and Kolditz 1998).

In order to gain insights into the temporal evolution of the studied system a reasonable computing time interval has to be set. For the problem considered here, such an interval is strictly artificial, having no relation to any geological timescale. Nevertheless, the computing time interval should not be too low with regard to the geological time-range of flow processes in sedimentary basin (i.e. ka or Ma). Here a computing time interval of 200 ka has been set. When a time scale will be mentioned in the description of the results, it will be referred to computing time with no regard to a particular geological timescale.

In bad-posed problems the predicted time-step size decreases asymptotically at a certain moment of the numerical simulation process. Consequently the numerical problem cannot be solved within the appointed computing time interval. During the iterative process this behaviour indicates that the constraints cannot be satisfied. This is likely due to an insufficient mesh definition. In other words, the finite elements of the grid simply do not work.

#### **2.2.4. Building a mesh suitable for the thermohaline approach**

According to the previous considerations, a mesh suitable for thermohaline flow can be defined. The finite element composing the mesh should be constructed so that an asymptotic decrease of the time-step will not arise. The iterative time scheme will then run over the prescribed computing time-scale (200 ka) and a preliminary solution of the transient problem can be obtained. Moreover temperature effects on the flow regime must be taken into account. Therefore the mesh must be sufficiently refined in order to avoid over-dissipative terms introduced by the upwinding scheme (Eq.(2.7)). The last requirement is that mesh convergence is achieved. This implies that further refinement of the spatial discretizations will not introduce discrepancies in the results, i.e. the numerical calculations are independent from additional mesh refinements.

Fig 2-5 illustrates the finite element mesh of the representative cross-section obtained from the integrated 3D structural model. For pictorial needs a 10:1 vertical exaggeration is used. The mesh density is derived by the original resolution of the structural model.

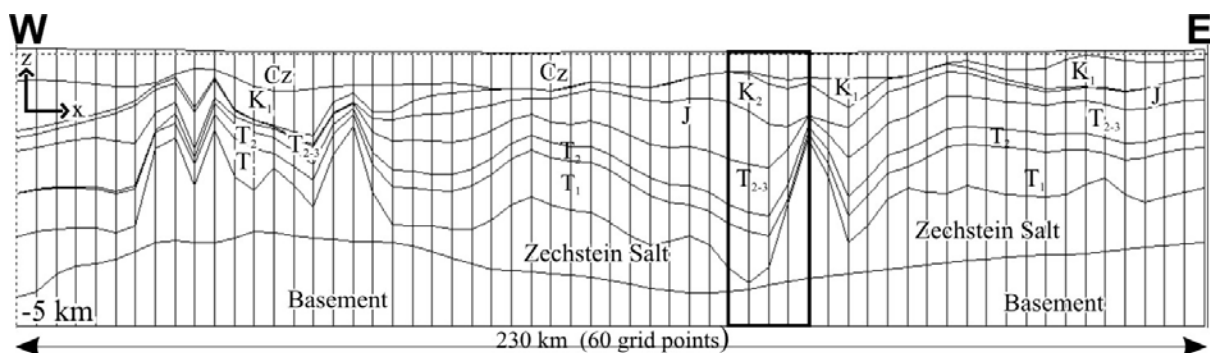


**Fig.2-5:** Initial finite element mesh obtained from the original 3D structural model of the NEGB. For pictorial needs a 10:1 vertical exaggeration is used. 60 grid points discretize each model slices. The rectangle delimits a salt dome environment which is illustrated in Fig.2-6 and Fig.2-7 with no vertical exaggeration.

As mentioned in paragraph 2.1.2. each model slice is discretized by 60 nodes and every layer is composed of 59 quadrilateral elements. The mesh resolution is 3.9 km in the horizontal direction ( $x$ ). The vertical mesh resolution is determined by the layer thickness and can span from few meters up to 1 km. The morphology of all stratigraphic units in the neighbouring of salt diapirs is highly deformed. The finite elements geometry is extremely distorted especially in the vertical direction ( $z$ ). The elements taper at the salt dome crests, i.e. the quadrilaterals are narrow trapezoids.

It turned out that the time-step size decreased asymptotically when this finite element mesh was used to solve the thermohaline problem. Moreover this problem arose as soon as

the simulation was initialized. Therefore the simulated computing time could not cover 200 ka.

All 2D finite elements are formulated such that a perfect equilateral triangle or square give the best answers. As elements deviate from these perfect shapes, there is a corresponding degradation in the computed results (MacNeal 1990). The element aspect ratio is an helpful indicator of the element performance. This ratio is defined as the value obtained by dividing the maximum length of the element in the horizontal direction ( $x$ ) by the maximum length in the vertical direction ( $z$ ). Square mesh elements are associated to unitary aspect ratio. At the resolution of 60 grid points per slices all elements discretizing the model area present an aspect ratio higher than one, i.e. the quadrilaterals are elongated in the horizontal direction ( $x$ ). A mesh refinement applied in the vertical direction ( $z$ ) increases the density of nodes in the  $x$  direction. Consequently, vertical refinements can lead to an element aspect ratio value close to one. Fig. 2-6 illustrates a zoom of the finite element discretizing a salt dome. No vertical exaggeration is used.

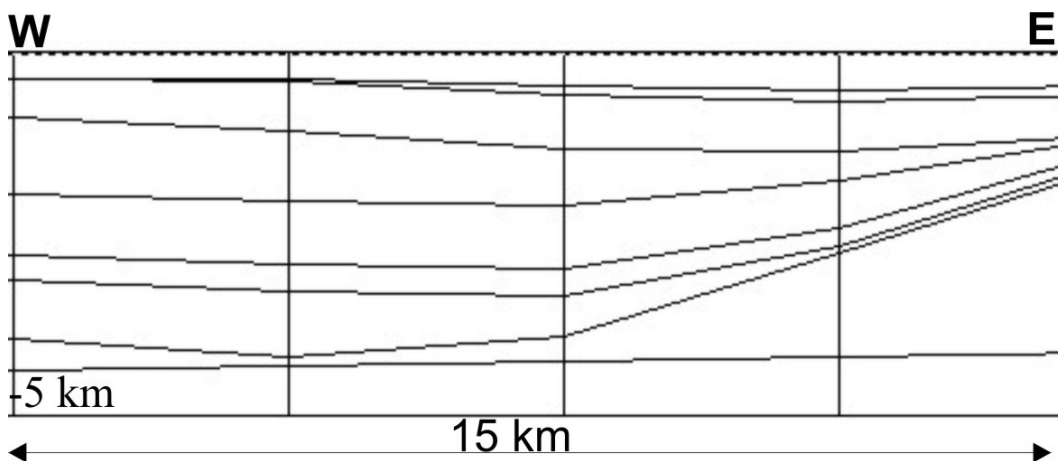
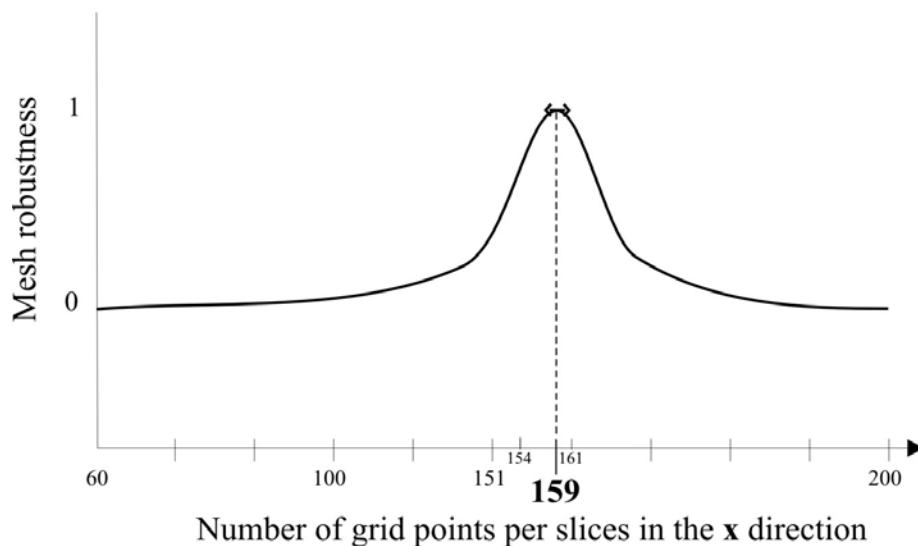


**Fig.2-6:** Zoom of the initial finite element mesh in salt a dome environment. No vertical exaggeration. The mesh resolution of the cross-section from which this zoom is obtained is 60 grid points per slice. The chosen salt dome is localized in the rectangle depicted in Fig.2-5.

The finite elements taper along the steep salt flanks. No vertical refinement can possibly transform these distorted elements to squares. Since many salt domes are included in the domain, perfect square elements cannot be obtained throughout the whole model area. A compromise has to be found. In this context, the only way to obtain “good” elements that will work for the simulation process, is to apply a vertical refinement on the whole mesh and test whether the simulation based on this denser mesh can run over the appointed computing-time or not. If an asymptotical decrease of the time-step occurs during the simulation it is probably because most of the elements do not work properly. A denser vertical refinement is then

necessary. Eventually a correct mesh discretization is obtained by repeatedly applying the described procedure. The refinement can be easily applied on the original structural model by the use of the FEFLOW mesh editor interface. This pragmatic approach can hopefully be successful in building a robust finite element mesh suitable for thermohaline problem. If so, the simulation will run over the computing time interval and a preliminary “solution” can be achieved.

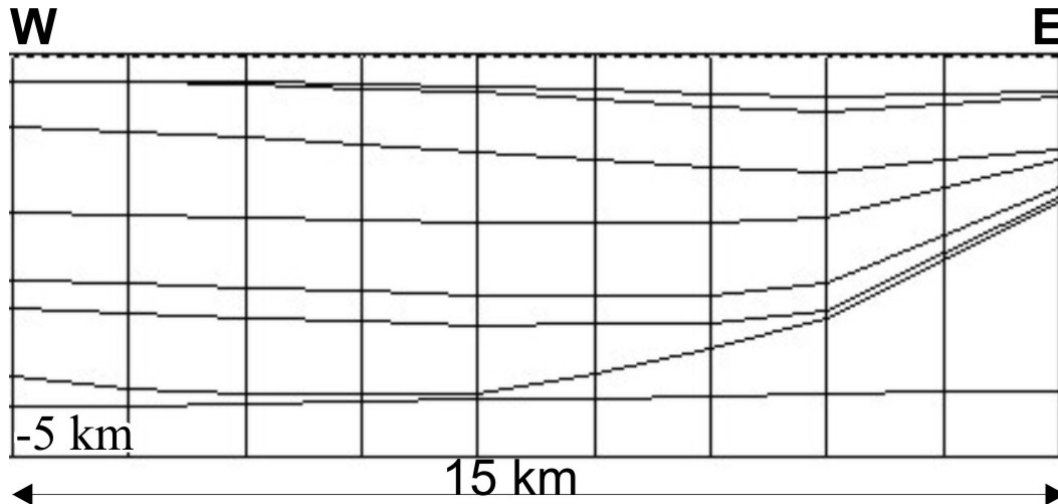
Fig.2-7 is a sketch illustrating the mesh robustness as a function of the number of grid points discretizing the model slices. The robustness index is “0” when asymptotical decrease of the time-step has occurred during the simulation and the calculations could not be completed. “1” indicates that the simulation ran successfully over the computing time interval of 200 ka. Vertical refinements have been applied up to 200 nodes per slices. It can be seen that a successful simulation has been carried out on a mesh having 159 grid points per slices. An interesting feature of the mesh robustness can be inferred by from Fig.2-7.



**Fig. 2-7:** Sketch illustrating the mesh robustness as a function of the number of grid points discretizing the model slices in the horizontal direction (x).

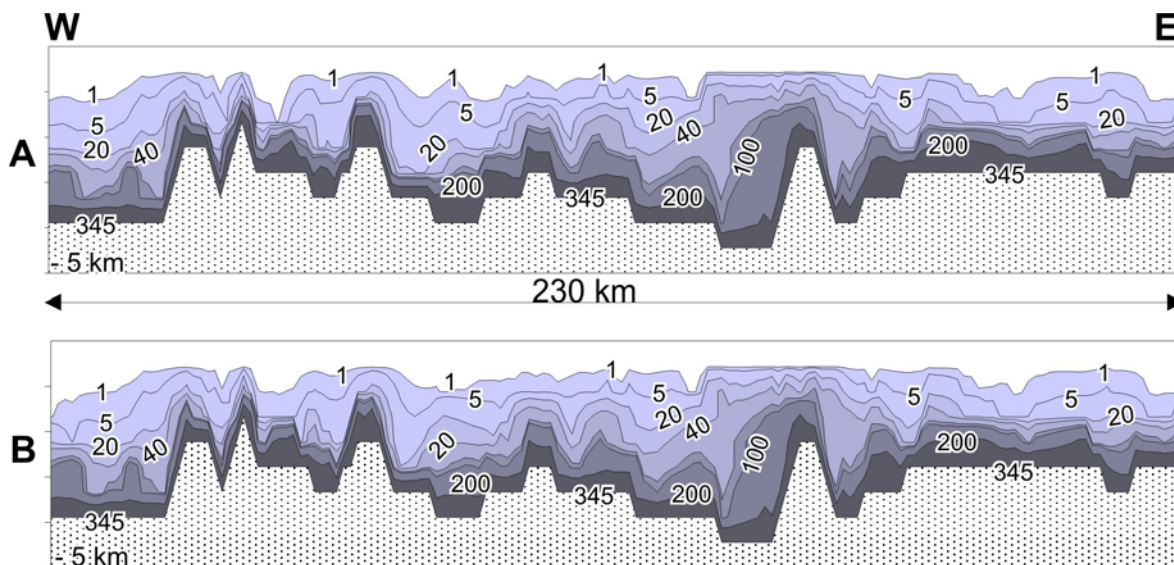
The simulation process is very sensitive to the number of grid points discretizing the slices. As long as this number is far from 159 the simulations could not be completed: numerical oscillations occurred immediately after the process was initialized and the predicted time-step decreased asymptotically. On the other hand, simulations based on meshes having a grid density very close to 159 points per slices could run over 200 ka although with some time-step oscillations. Higher vertical mesh refinements did not improve the simulation stability, in contrary it is declining.

Fig.2-8 illustrates the resulting refined finite element mesh in a salt dome environment (cf. Fig.2-6) No pictorial vertical exaggeration is used. The thicker quadrilaterals are less elongated and are slightly close to square shape in some distance from the salt flanks.



**Fig.2-8:** Zoom of the refined finite element mesh in salt a dome environment. No vertical exaggeration. The mesh resolution of the cross-section from which this zoom is obtained is 159 grid points per slice. The chosen salt dome is localized in the rectangle depicted in Fig.2-5.

At this point a mesh allowing a complete simulation run over the computing time (200 ka) has been obtained. Longer term calculations have been successfully performed on this mesh up to 400 ka. The whole model area is now composed of 1422 elements, each slice being discretized by 158 nodes. This value corresponds to a mesh resolution of 1.45 km in the horizontal direction. However, numerical dissipative terms introduced by the upwind balancing tensor diffusivity (Eq.(2.7) can still be dominant at this mesh resolution. If this is the case, only the numerical diffusivity governs the transport process. As a result, thermohaline and coupled fluid flow-mass transport simulations lead to the same mass profile. In order to check whether this is the case or not the mass profile resulting from a coupled fluid flow-mass transport problem has been compared to the mass profile obtained from a thermohaline simulation. The results are illustrated in Fig.2-9.



**Fig.2-9:** Mass distribution obtained from: a thermohaline simulation (A), and from a coupled fluid flow and mass transport simulation (B).

No significant variation can be observed by comparing the mass distribution obtained from thermohaline simulation (Fig.2-9A) with the mass distribution derived from a coupled fluid flow and mass transport problem (Fig. 2-9B). The transport process is dominated by the over-estimated numerical dissipation and the resulting mass profile has no physical meaning. Temperature effects on solute transport are overwhelmed and cannot be taken into account at this mesh resolution. The actual mesh is surely robust, providing a “solution” of the problem. Nevertheless, robustness alone is not sufficient. Indeed the solution is only mathematically correct but physically unlikely. At this mesh resolution, the numerical scheme defines a problem which is completely different from the real natural system. Therefore the mesh has to be further refined.

In order to preserve the global aspect ratio of the finite elements, which has until now ensured the mesh robustness, vertical and horizontal mesh refinements are performed simultaneously. In this way, an element will be subdivided in 4 new elements having the aspect ratio of the original element. This refinement procedure has been repeatedly applied until both thermohaline and coupled fluid flow-mass transport simulations have provided different mass patterns. It turned out that two consecutive refinements were necessary in order to observe substantial differences in the mass profiles of the two different problems. Each finite element is therefore subdivided in 16 new elements. The whole model consists of 22752 elements (1422 x 16). The total number of slices is 37, each of them being discretized by 633 nodes. The mesh resolution is 364 m in the horizontal direction (x). Fig.2-10 illustrates the resulting mesh in a salt dome environment. At this resolution, temperature effects on the

transport process can be taken into account. The simulation results based on this refined mesh will be shown in the next chapter.

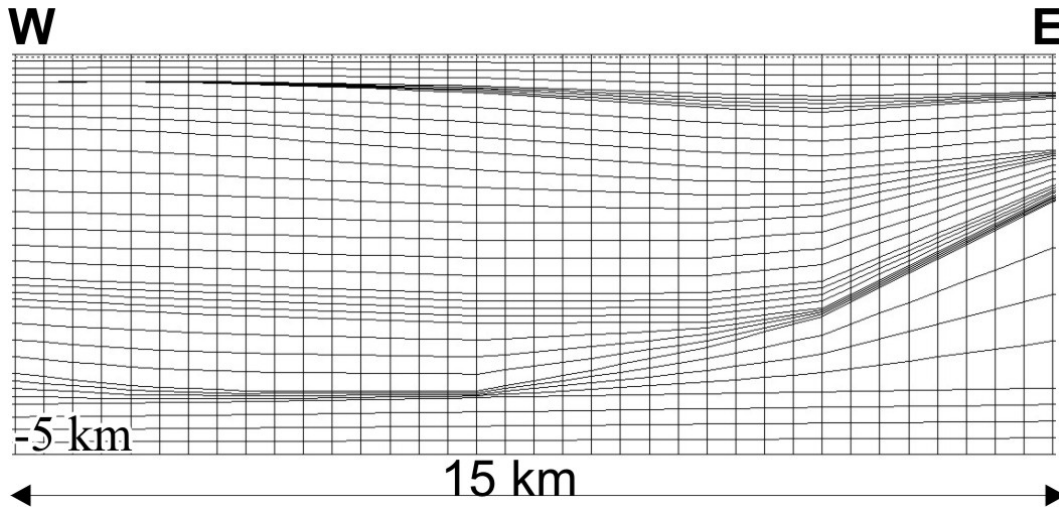


**Fig.2-10:** Zoom of the final finite element mesh in salt a dome environment. No vertical exaggeration. The final mesh resolution of the cross-section from which this zoom is obtained is 633 grid points per slice. The chosen salt dome is localized in the rectangle depicted in Fig.2-5.

With the purpose of testing the grid convergence an additional refinement has been applied. No spatial discretization effects were observed with regard to the mass patterns of the thermohaline problem. The results are independent from further mesh refinements. This proves that the actual resolution the finite element mesh ensures convergence.

## 2.3. Discussion

In this chapter a representative cross-section of the NEBG has been obtained. The initial mesh resolution of the original structural model has been refined so that:

- A preliminary solution can be calculated over a prescribed computational time of 200 ka, or even longer.
- The numerical scheme approximations do not dominate the transport processes. Brine flow induced by concentration and temperature gradients can be taken into account by the mesh.
- The grid convergence is achieved.

The final mesh consists of 23421 nodes (22752 elements) with a resolution of 364 m in the horizontal direction.



Fluid flow, heat and mass transport simulations will be henceforth based on this finite element mesh. In the next chapter the mechanisms driving salt within the NEGB will be investigated. A new set of boundary conditions will be defined in order to reproduce observed data such as brine and fluid temperature distribution at the surface. The interaction between topography driven flow and solute transport will be quantified (forced versus free convection). The main fluid-dynamics of salt migration throughout the sediments fill will be inferred from evolution analysis of the transport processes. Furthermore, viscosity effects will be taken into account and evaluated. Based on these 2D numerical results, a regional picture of the transport processes affecting the NEGB will be tracked down.

## **Chapter 3. Mechanisms driving brines within the NEGB.**

### **Results from 2D coupled fluid flow-mass transport and thermohaline simulations**

In this chapter the various components involved in brine transport within the NEGB are described. For this purpose, the chapter has been structured in two parts. In the first part, diffusive brine transport is studied. Subsequently, the advective mass flux induced by topography-driven fluid flow (variable hydraulic head) is also taken into account. In the second part, temperature effects are investigated by simulating thermohaline convection. When the regional flow is excluded or included in the thermohaline model the regime is respectively referred to as free or mixed convection. In order to allow mass and heat outflow through the surface, open boundary conditions for fluid concentration and temperature are defined. Initial conditions for head, mass and temperature distribution are those illustrated in Chapter 2, paragraph 2.2.2.

The evolution of temperature and mass patterns are shown at two time steps. In all the pictures, the label “A” and “B” refer to a computing time of  $t = 30$  ka and  $t = 200$  ka respectively. It is worth recall that these time steps are not referred to any geological timescales but present computing time (paragraph 2.2.3). Accordingly, the patterns shown here depict “snapshots” in time. The results will indicate the possible mechanisms leading to near-surface salt water occurrences.

### **3.1 Diffusive brine transport**

In this first part, the heat flux balance equation (Eq.(2.4)) is not solved since temperature gradients are neglected. Therefore, the EOS for the fluid density (Eq.2.6)) is a function of pressure and concentration with no temperature dependency (i.e.  $\beta = 0$ ).

#### **3.1.1 Boundary conditions**

The boundary conditions defined for the diffusive brine transport problem are the following:

- The surface is permeable to solute outflow while the head boundary conditions will be discussed separately in the next paragraphs for the case in which the regional flow is excluded or included in the model.
- At the Top Salt a fixed concentration value of 345.2 g/L is set,
- The lateral boundaries are closed to fluid and mass flow.

In the NEGB the advected solute can flow out of the basin through the upper surface. For that reason, an open boundary condition allowing solute outflow (i.e. permeable) is needed at the top surface of the model domain. This boundary condition, referred to as Cauchy type boundary condition, is defined by the following relation:

$$\mathbf{q}_C(t) = -\Phi_C(C^* - C)\mathbf{n} \quad (3.1)$$

where  $\mathbf{q}_C$  is the solute flux,  $\Phi_C$  is a mass transfer coefficient,  $C^*$  is the prescribed boundary condition value for the solute concentration  $C$  at the surface, and  $\mathbf{n}$  is the vector normal to the top surface of the domain. By setting a natural boundary condition for the solute at the top slice of the model, the concentration  $C$  is solved at each node of the boundary: a solute flow through the top surface of the domain is computed. The transfer coefficient  $\Phi_C$  appearing in Eq.(3.1) can be regarded as a leaching parameter which governs the mass flux through the boundary. The two limiting cases for  $\Phi_C$  are  $\Phi_C = 0$  and  $\Phi_C \rightarrow \infty$ . In the first case, the surface is impervious to solute flux since  $\mathbf{q}_C = 0$ . For a very large value of  $\Phi_C$ ,  $C \rightarrow C^*$  and therefore the Cauchy boundary condition is reduced to a Dirichlet-type. The mass transfer is a numerical coefficient allowing the definition of an open boundary condition in the form of Eq.(3.1) rather than a real measurable parameter. Nevertheless a reasonable value of the mass transfer coefficient can be estimated by rewriting Eq.(3.1) in a Fickian form, viz.:

$$q_C(t) \approx -D_{\text{leak}} \frac{C^* - C}{d} \quad (3.2)$$

where  $d$  is the thickness of a thin stratum in contact with the top surface of the domain through which the solute leaches. The mass transfer coefficient then becomes:

$$\Phi_C \approx \frac{D_{\text{leak}}}{d} \quad \text{in } [ms^{-1}] \quad (3.3)$$

where  $D_{\text{leak}}$  is a representative molecular diffusion coefficient of the thin stratum.  $D_{\text{leak}}$  can be considered more or less equal to the molecular diffusivity of the bordering stratigraphic unit (i.e. Cenozoic,  $D_{\text{leak}} \approx 2 \times 10^{-9} \text{ ms}^{-2}$  Table 1.1). A stratum thickness in the range of a meter can be regarded as relatively thin with respect to the basin scale. Hence, from Eq.(3.3)  $\Phi_C \approx 2 \times 10^{-9} \text{ ms}^{-1}$ . The prescribed surface boundary condition  $C^*$  has been set equal to the reference concentration value, i.e.  $C^* = 0 \text{ g/L}$ .

### **3.1.2 Diffusive brine transport without regional flow**

In this paragraph, the regional flow is not taken into account in the simulation of brine transport. By ignoring topography-induced fluid flow the resulting brine patterns are not affected by advective flux and salt dissolution is not enhanced by any external factor. Therefore the major sources of salinity can be directly inferred.

In order to exclude the regional flow from the simulation, the head has been referred to a constant value of 25 m at the upper boundary. This value corresponds to the minimum surface elevation of the study area so that the head level cannot exceed the topography.

Fig.3-1 A, B illustrate the resulting mass patterns at the computing time of 30 ka and at the end of the simulation run ( $t = 200 \text{ ka}$ ) respectively. In these figures a 10:1 vertical exaggeration is used. P1 and P2 indicate two profiles in which the results will be illustrated afterwards with no vertical exaggeration. At  $t = 30 \text{ ka}$  (Fig.3-1 A) brine plumes with 1 g/L form on the salt diapirs crest and sinks along the domes flanks into the deeper sediments. Additionally, a strong concentration gradient develops within the whole Buntsandstein unit. The concentration values range from 200 g/L at its surface to 345 g/L which is the halite fluid saturation at the top salt. The interface fresh water/brine is well defined and located above the Buntsandstein surface within the Muschelkalk. This feature is explained as follows: starting from the initial mass concentration, a transition zone between fresh water and highly concentrated brine diffuses throughout the Buntsandstein as a result of salt dissolution. Due to its very low permeability, the Muschelkalk inhibits the motion and sharply shapes the interface of this transition zone. Accordingly, a very high concentration gradient is formed within this unit. At  $t = 200 \text{ ka}$  (Fig.3-1 B) the salt distribution within the Buntsandstein remains unchanged which proves that a steady concentration gradient has been reached herein. On the other hand, above the Buntsandstein, dissolved halite continues diffusing in the neighbourhood of salt domes. Layered brine plumes spread at both sides of the salt diapirs (Fig.3-1 B). The salt dome environment is hydrologically unique, i.e. groundwater is

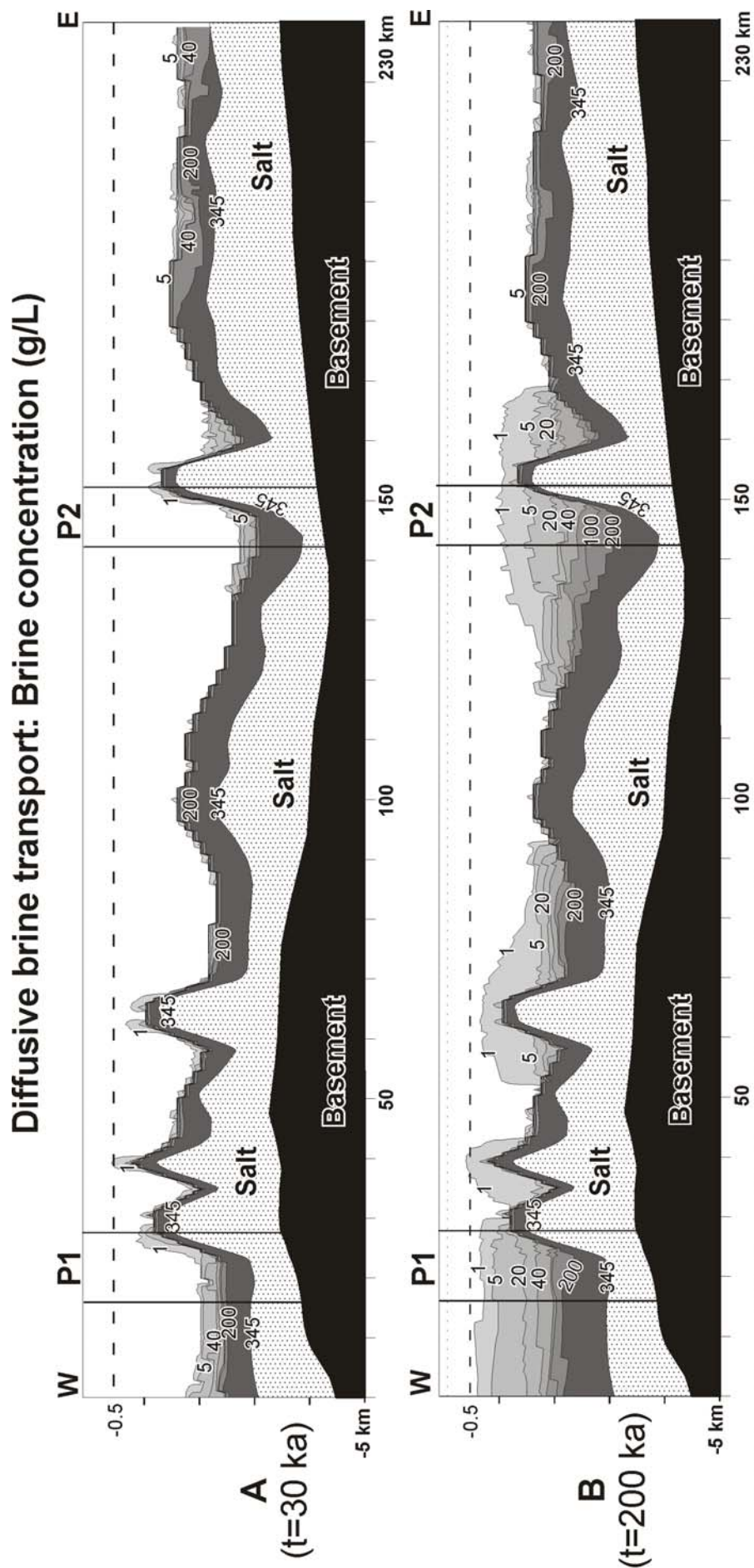


**Fig.3-1: A and B** mass distribution resulting from coupled fluid flow and mass transport simulation at  $t = 30$  ka and  $t = 200$  ka respectively. The regional flow is excluded from the numerical computation. Salt concentrations are expressed in g/L. The snapshots are interpolated by the use of Surfer 8® and illustrated with a 10:1 vertical exaggeration. Two profiles P1 and P2 are located within the cross-section. The simulation results for these two profiles are shown with no vertical exaggeration in Fig.3.2 and Fig.3.3

subjected to large lateral salinity gradients. Along salt dome flanks the density gradient drives groundwater flow laterally into the basin. The dissolved halite spreads away from salt bodies by diffusion and increases rapidly the salinity of the pore water throughout the sediments. The resulting brine plumes extend over 30 km in the lateral directions. As a result, dissolved halite concentration around salt domes increases with depth. Above salt diapir crests, brackish water with 1 g/L of dissolved salt can reach a depth between one and half kilometre. Far from salt domes, the salty plumes do not develop as it is the case in the central and eastern part of the basin.

In Fig.3-2 A, B the velocity field (label 1) and the formation of brine (label 2) are illustrated along the diapir “P1”. No vertical exaggeration is used and two simulation stages are depicted (label A:  $t = 30 \text{ ka}$ , label B:  $t = 200 \text{ ka}$ ). Brine density flow develops rapidly and the highly concentrated salty groundwater forming near the flank of the diapir sinks due to gravity (Fig.3-2 A). Downward brine flow generates a clockwise convective cell of fresh water above the salt dome which recharges the sediments (Fig.3-2 A1). After 30 ka, the pore velocities range from  $2 \text{ cm yr}^{-1}$  to few millimeters per year. Maximum flow velocity occurs adjacent to the dome edge. By comparing Fig.3-2 A with Fig.3-2 B it turns out that, as time progresses, the velocities decrease and the convective cell breaks apart (Fig.3-2 B1). This occurs since halite diffuses from the salt flanks into the overlying sediments and brines fill up more of the sediments surrounding the salt dome (Fig.3-2 B2). Peak velocities still occur along the salt diapirs flank. Since a constant salt concentration is used as boundary condition for the solute at the salt surface there is a lateral density gradient at all times near the salt dome. Therefore, downward solute motion continues even after the surrounding sediments are filled with brine. The observations pertaining to this salt dome environment hold for all salt domes present in the section. For the sake of completeness, velocities and mass patterns are also shown for another salt flank in Fig.3-3. The location is indicated with “P2” in Fig.3-1. At the beginning of the process, a fresh water convective cell forms above the salt dome as a result of dissolved halite sinking along the salt flanks (Fig 3.3 A1). The pore velocities span the same range as in profile 1, i.e. from  $2 \text{ cm yr}^{-1}$  to few millimeters per year. At the end of the simulation process, sediments are filled with more brine and flow velocities decrease (Fig.3-3 B). All the described features have also been attained by Evans et al. (1991), who investigated the mechanisms driving groundwater flow near salt domes.

Diffusive brine transport: Profile P1

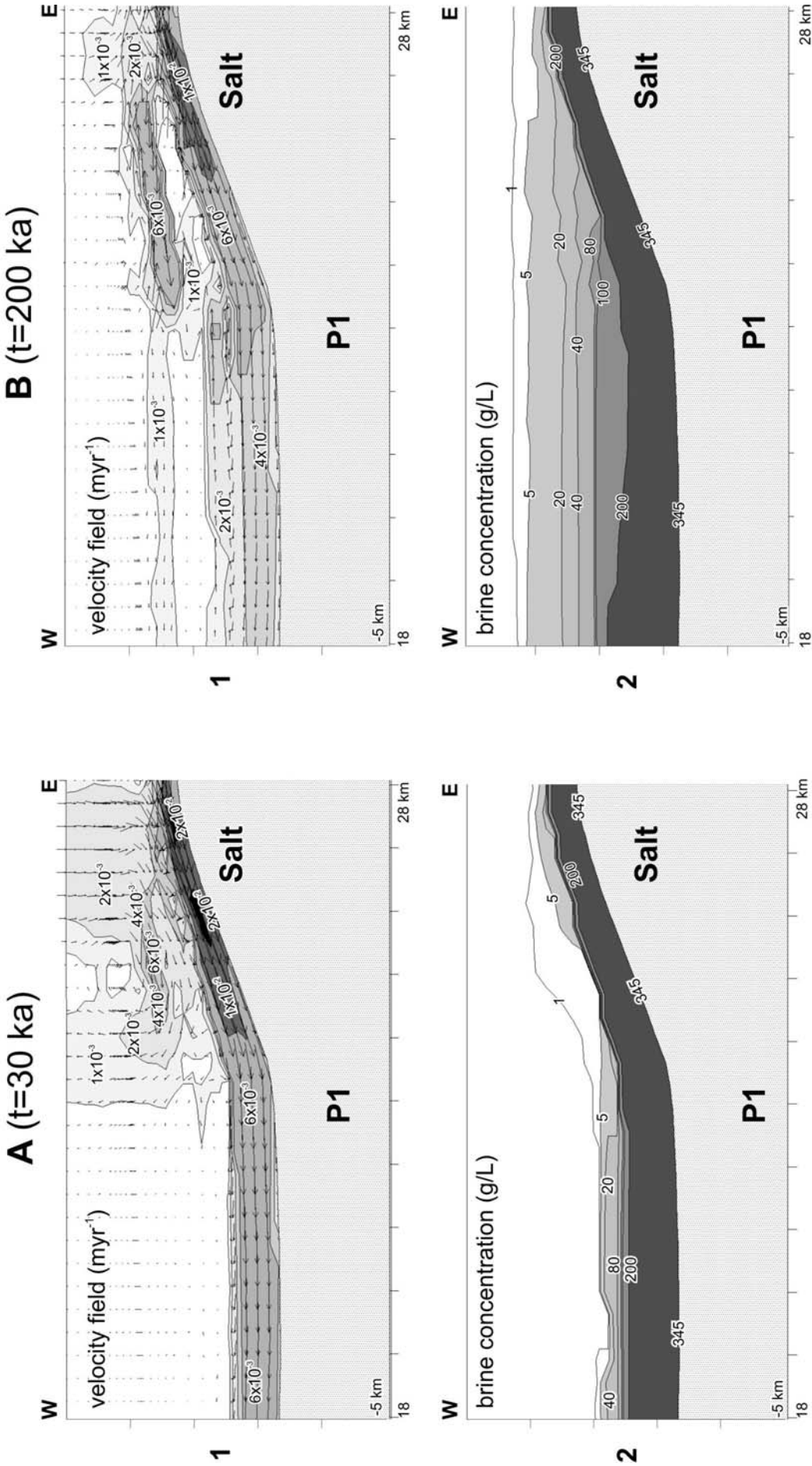


**Fig.3-2: A and B:** Zoom of the diffusive brine transport simulation results for profile P1 as located in Fig.3.1 at  $t = 30$  ka and at  $t = 200$  ka respectively. No vertical exaggeration is used. **1:** pore water velocity field in  $\text{myr}^{-1}$ . Pore vector linearly scaled to the largest flow arrow. **2:** Salt concentration distribution in g/L.

## Diffusive brine transport: Profile P2

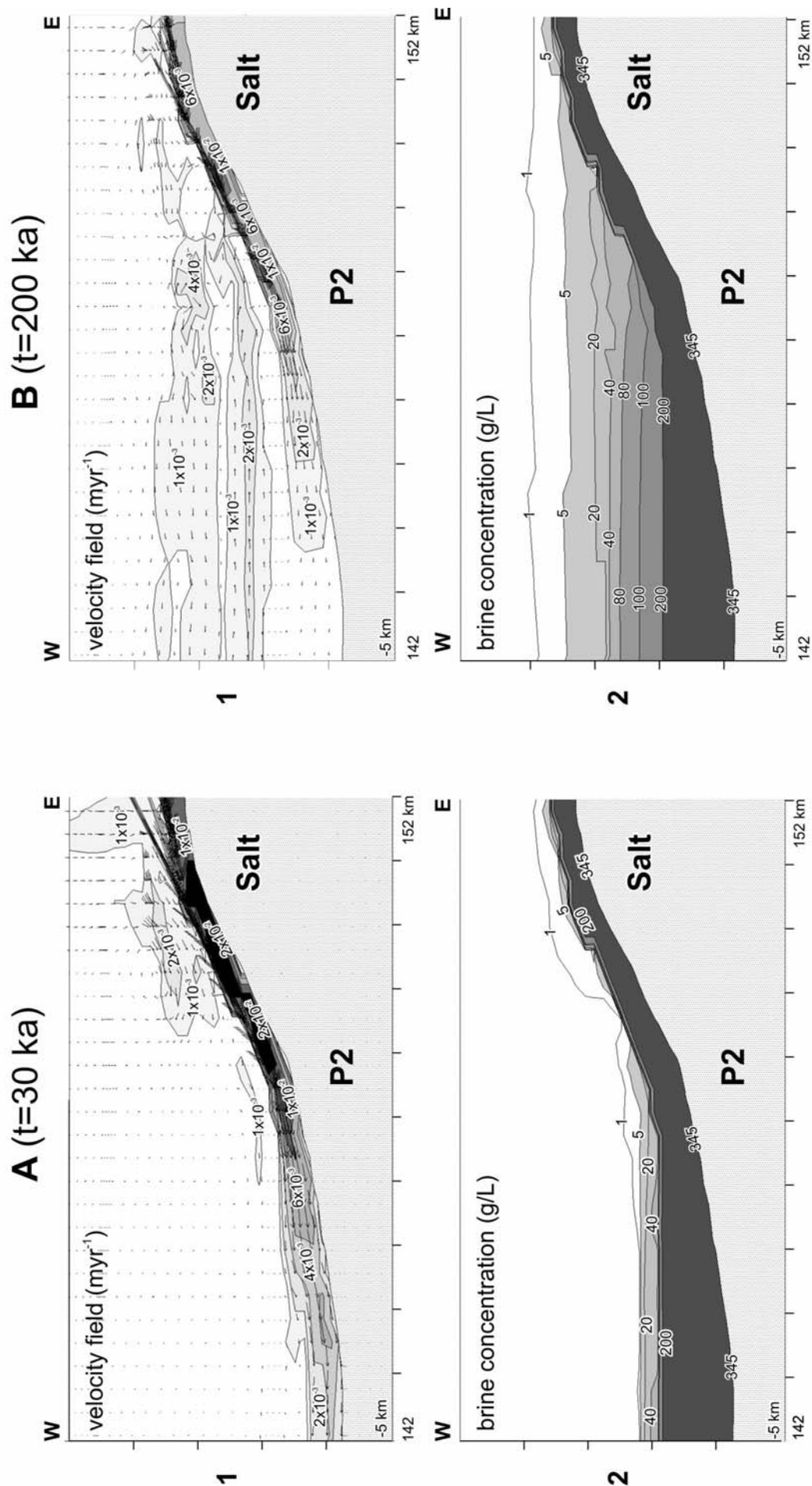


**Fig.3.-3: A and B:** Zoom of the diffusive brine transport simulation results for profile P2 as located in Fig.3.1 at  $t = 30$  ka and  $t = 200$  ka. No vertical exaggeration is used. **1:** pore water velocity field in  $\text{myr}^{-1}$ . Pore vector linearly scaled to the largest flow arrow. **2:** Salt concentration distribution in g/L

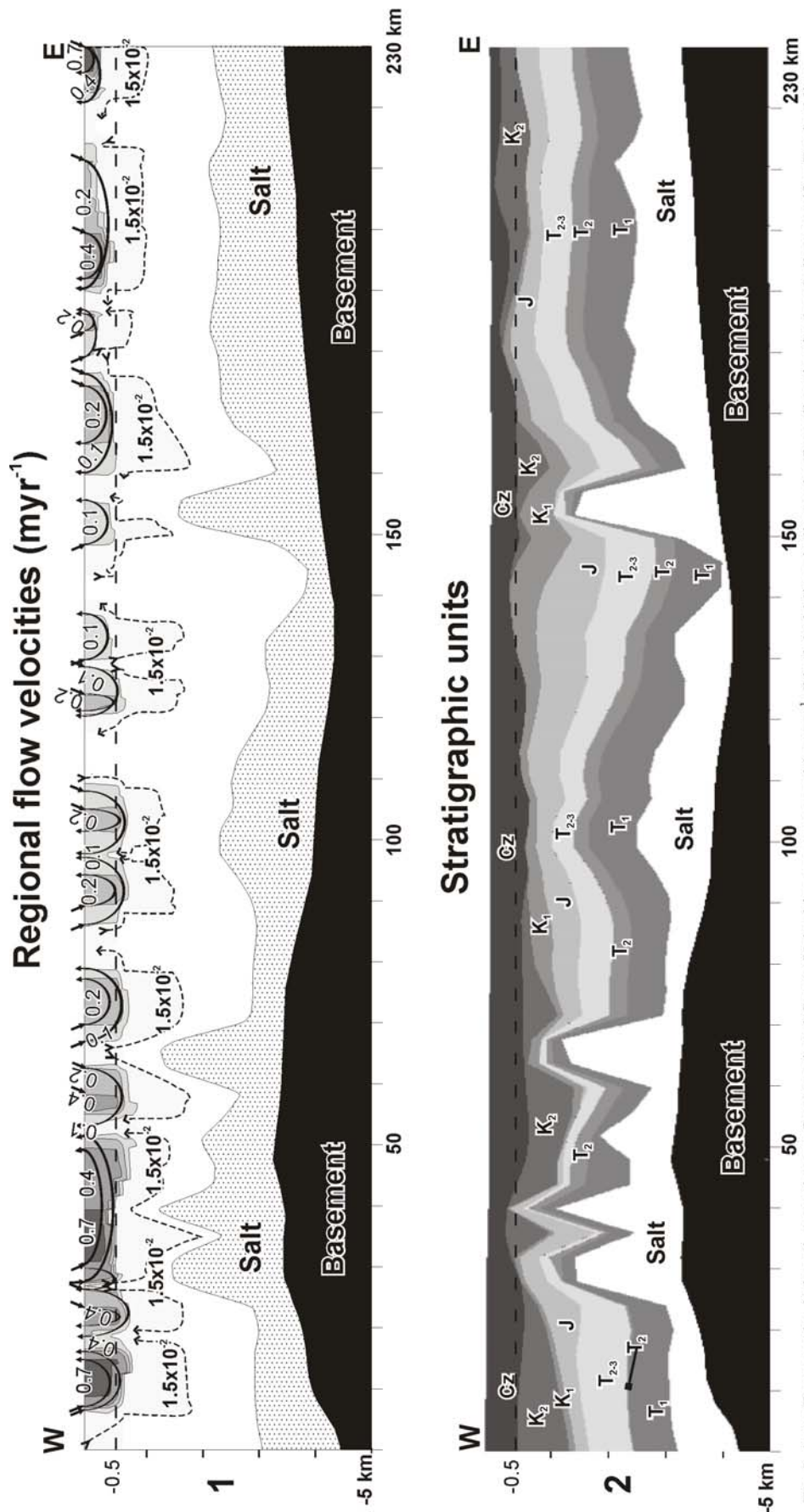


In summary, the numerical results show that in the Buntsandstein a steady state concentration profile is already achieved at an early simulation stage ( $t = 30 \text{ ka}$ ). As time progresses, the mass pattern within this unit does not undergo significant variation. On the other hand, around the salt diapirs, halite continues diffusing and salty water fills the surrounding sediments in the lateral direction. In salt dome environments, active halite dissolution occurs and density driven fluid flow is the major transport mechanism. Steep salt structures supply a continuous halite replenishment. Downward motion of dissolved halite, due to the gravity, is dominant along salt flanks. The calculated velocity peak is  $2 \text{ cm yr}^{-1}$ . The resulting drag forces generate localized convective cells in the overlying sediments which provides the main recharge of fresh water. As heavier salt-laden water is produced, velocities decrease and the convective cells weaken or disappear. Brackish water with  $1 \text{ g/L}$  of dissolved salt occurs at depths between half and  $1 \text{ km}$  in the surrounding of shallow salt structures.

### **3.1.3 Diffusive brine transport and regional flow**

Numerous factors influence the transport of salt and groundwater flow near salt domes. In sedimentary basins, forced advective flux provided by the regional flow cannot be overlooked (Bodenlos 1970; Posey and Kyle 1988). Regional flow enhances fluid circulation due to the viscous drag, promotes salt dissolution and extend salinity plumes away from the salt domes (Evans et al. 1991). As mentioned in paragraph 1.2.3, the fresh meteoric water infiltrates into the sediments induced by topographical variation. The mixing processes between regional and groundwater flow are supposed to reach approximately a depth of half a kilometer. In the NEGB most of the salt domes penetrate nearly to the basin surface and therefore are exposed to, and affected by topography-driven inflow of fresh water.

Numerically, the regional flow is taken into account by setting the head level equal to the topographic relief. Under these hydraulic boundary conditions, groundwater recharges the basin in the highlands while discharge areas occur in the lowlands. The rate of flow is controlled by the topographic relief and the patterns of flow mostly by the permeability, and the geometry of the stratigraphic units. Fig.3-4 (1) illustrates the regional flow patterns together with the computed velocity field. The stratigraphic units of the cross section are shown below (Fig.3-4 2). In the shallow aquifer (i.e. down to  $500 \text{ m}$  depth) the fluid flow direction is schematically represented by bold arrows while dashed arrows are used for the deeper part of the basin. The more intense regional flow is confined in the Cenozoic unit where the sediments have the highest hydraulic conductivity.



The fluid velocities range from  $0.7 \text{ m yr}^{-1}$  to  $0.1 \text{ m yr}^{-1}$  whereas at a depth of 2 km fluid motion occurs at a velocity of few centimeters per year. These strong variations in the velocity range reflect the high heterogeneity of the sediments.

The calculated mass distribution is illustrated in Fig.3-5 A, B at the beginning and at the end of the simulation process ( $t = 30 \text{ ka}$  and  $t = 200 \text{ ka}$  respectively). The regional fluid flow streamlines (as shown in Fig.3-4) are depicted as well. At  $t = 30 \text{ ka}$  (Fig.3-5 A) the Buntsandstein is saturated with heavy brine, as already discussed in the previous paragraph. On the other hand, at the western part of the basin, the concentration isopleths are convex: salt water upwelling begins near the salt dome. An elongated plume of brackish water is found in association with upward fluid motion supplied by the topography-induced flow. As time progresses, the salty plume extends up to the surface (Fig.3-5 B). Brackish water with more than  $1 \text{ g/L}$  of salt spreads in the discharge area. Throughout the rest of the basin, brine transport is also strongly affected by regional fluid circulation in the neighborhood of salt domes. Salt downwellings (concave solutal isopleths) occur where fluid descend in the basin since fresh water infiltrates into the sediments. On the other hand, salt upconings (convex solutal isopleths) arise where fluid ascends. Nevertheless no brine outflow occurs with the exception of the western part of the basin where brine leaches through the surface. In general, the salty plumes reach a depth of approximately half a kilometer. The causes leading to surface salt occurrence in the western part of the basin can be inferred by observing the regional flow intensity (Fig.3-4 (1)) and the mass patterns resulting from salt diffusion (Fig.3-1). At the western part of the basin, groundwater is released at high velocities (Fig.3-4 (1)). Moreover, in that area of the basin, shallow salt dissolution is favored (Fig.3-1 B). As a result, the regional flow discharges in the lowlands at rates high enough to advect dissolved halite close to the surface. The brackish water leaches through the sediments and spreads at the surface.

In order to gain insights into the influence of topography-induced flow on salt transfer, the velocity field of the regional flow and the calculated salt concentrations are illustrated with no vertical exaggeration in two areas of the basin. The two profiles P3 and P4 associated with salt domes are indicated on the cross-section in Fig.3-5.

## Diffusive brine transport with regional flow: Brine concentration (g/L)

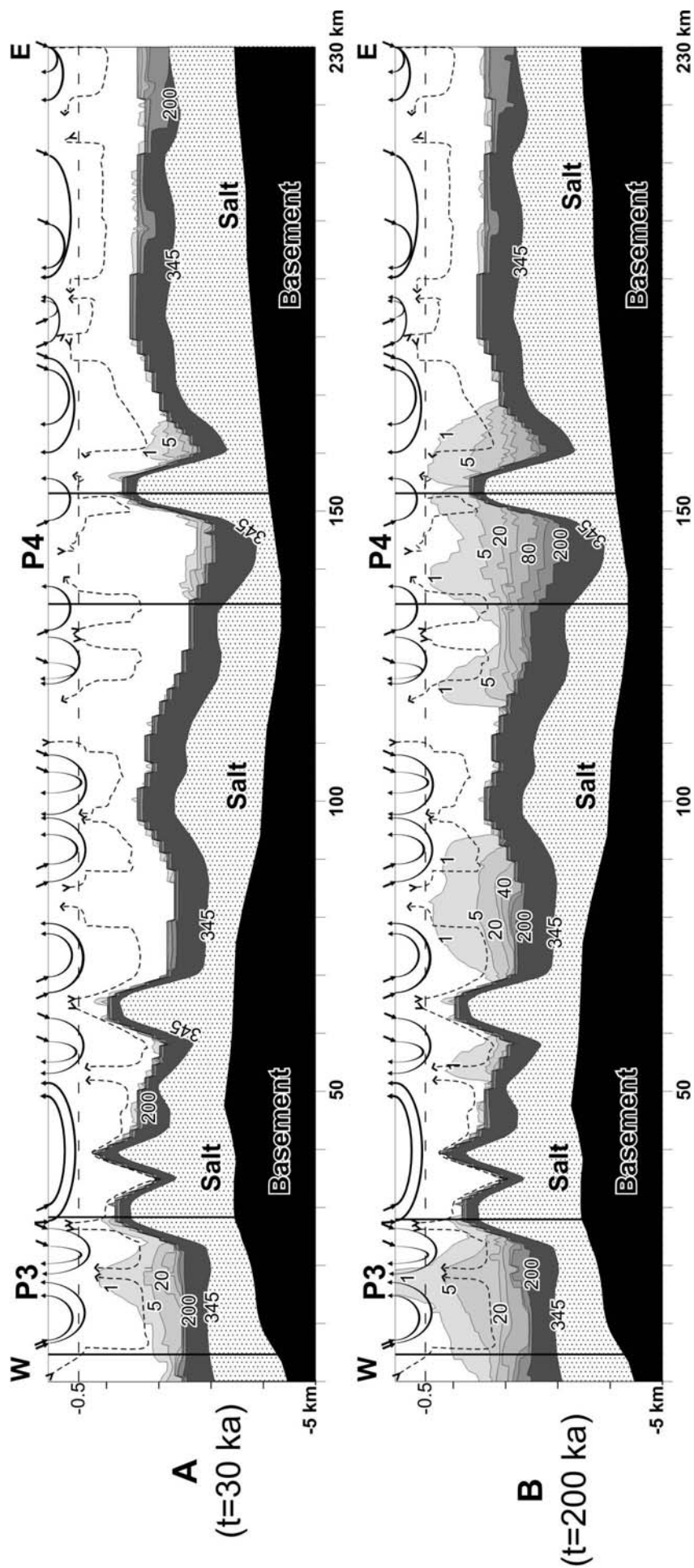


**Fig.3-5: A and B:** Mass distribution resulting from coupled brine transport and regional flow simulation at  $t = 30$  ka and  $t = 200$  ka respectively. Salt concentrations are expressed in g/L. Two profiles P3 and P4 are located within the cross-section. The simulation results for these two profiles are shown with no vertical exaggeration in Fig.3.6 and Fig.3.7

In profile P3 (Fig.3-6), the regional flow shows a marked confluence of pore water vectors 9 km from the eastern end of the section at the 19<sup>th</sup> km mark (Fig.3-6.A1). The peak pore water velocity is 0.7 m yr<sup>-1</sup> which is a very high value with regard to the range of the velocity flow field in the shallow aquifer (i.e. 0.1 to 0.4 m yr<sup>-1</sup>). Consequently, in the deeper part of the basin groundwater flows at higher velocities in relation to this intense regional flow. At 2 km depth, groundwater ascends in the upper aquifer at velocities of about 3-5 cm yr<sup>-1</sup>. As a result, the dissolved halite is advected upward within the basin and salt upconing begins at an early simulation stage ( $t = 30$  ka, Fig.3-6.A2). Additionally, upward halite migration is enhanced farther east by the confluent regional flow. On the other hand, downward flow of brine occurs along the salt flank at approximately 1.5 cm yr<sup>-1</sup> as already discussed in the previous paragraph. At the end of the simulation run, pore water velocities decrease slightly in the deeper part of the basin and along the salt flank since more dissolved halite has filled the sediments (Fig.3-6 B1). At  $t = 200$  ka, salty water reaches the surface (Fig.3-6.B2) and leaches through the upper boundary 10 km away from the salt diapir crest in the W-E direction.

By contrast, profile P4 (Fig.3-7.A) shows lower velocities with a uniform flow direction along the entire profile. At 2 km depth the pore water velocity is only 1.5 cm yr<sup>-1</sup>. Therefore at the beginning of the process salt upconing does not occur ( $t = 30$  ka, compare Fig.3-6.A2 with Fig.3-5.A2). A larger period is needed to observe increased concentration gradients within the sediment fill. At  $t = 200$  ka (Fig.3-7.B2) brackish water with 1g/L of dissolved salt is found at a depth of 0.5 kilometer in the eastern part of the profile above the salt diapir crest.

In summary, the simulations have emphasized the importance of topography induced fluid flow in affecting salt transport within the basin. Upward or downward migration of dissolved halite is respectively found in relation to ascending or descending fluid circulation due to the regional flow. Salt water upconing occurs only when the regional flow is included in the simulations (compare Fig.3-5 with Fig.3-1). Groundwater flow discharging at high rates in salt diapir environments, where shallow halite dissolution takes place, can possibly lead to surface occurrence of salty water in the lowlands. Herbert et al. (1988) demonstrated that overturn of groundwater above a salt column can result from viscous drag induced by a shallow regional flow.

## Diffusive brine transport with regional flow: Profile P3

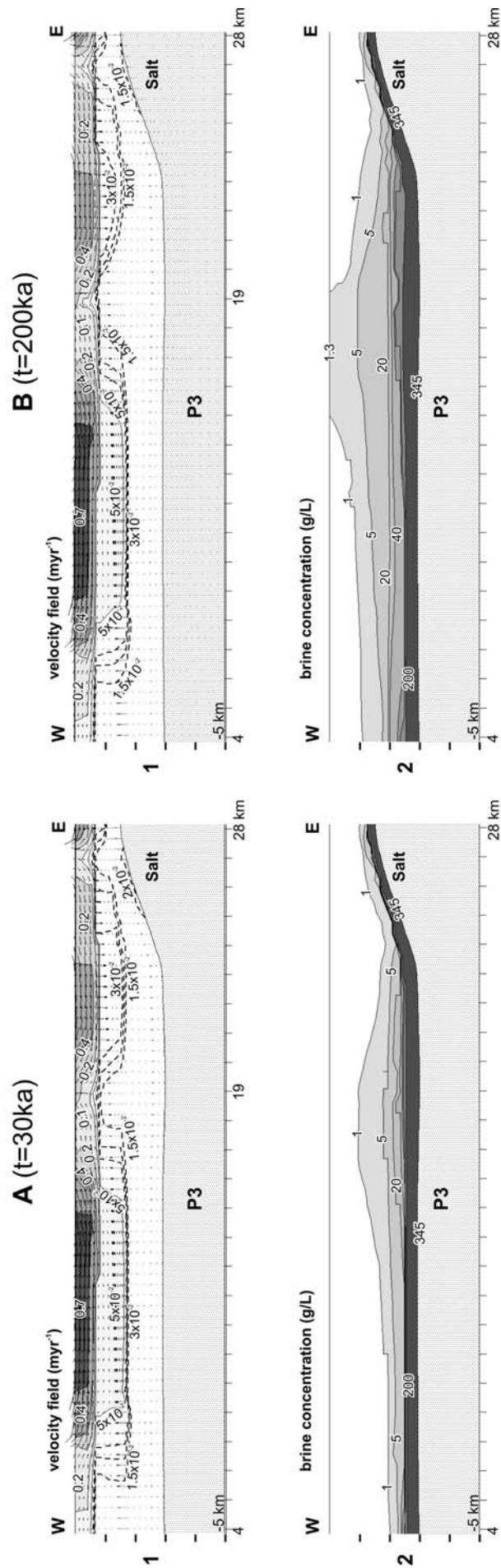


**Fig.3-6: A and B:** Zoom of the coupled brine transport and regional flow simulation results for profile P3 as located in Fig.3.4 at  $t = 30$  ka and  $t = 200$  ka respectively. No vertical exaggeration is used. **1:** Pore water velocity field in myr<sup>-1</sup>. Pore vector linearly scaled to the largest flow arrow. **2:** salt concentrations in g/L

## Diffusive brine transport with regional flow: Profile P4

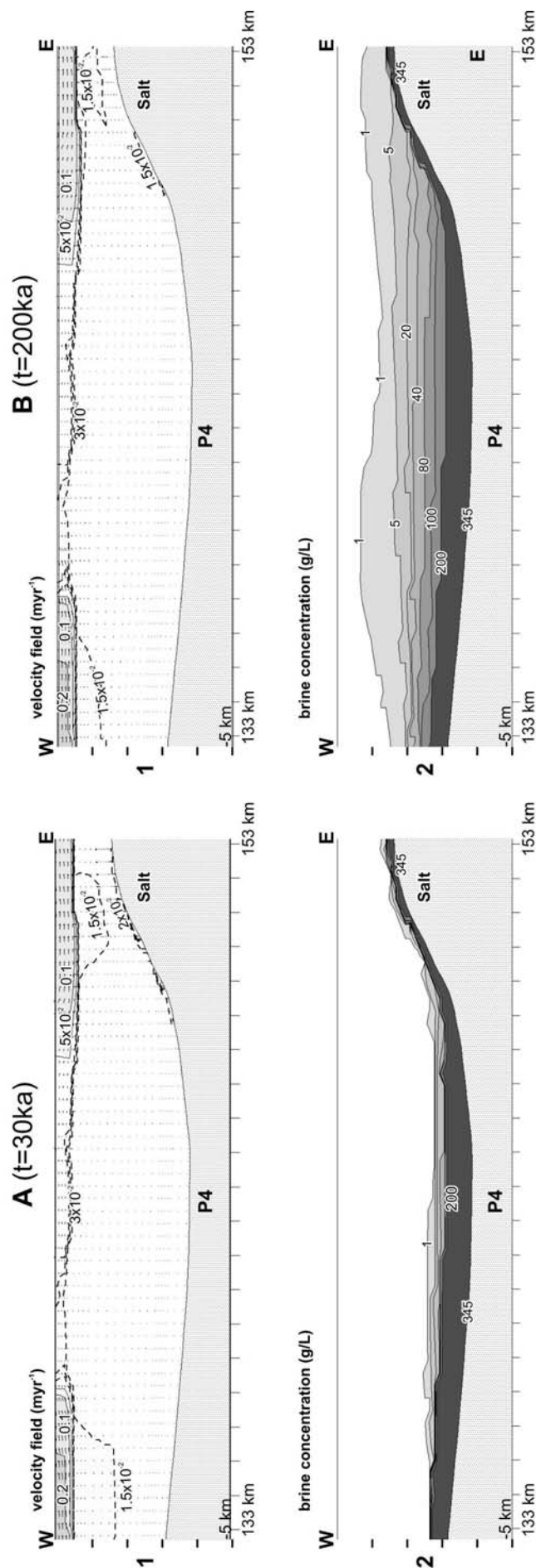


**Fig.3-7:** Zoom of the coupled brine transport and regional flow simulation results for profile P4 as located in Fig.3.4 at  $t = 30$  ka and  $t = 200$  ka respectively. No vertical exaggeration is used. **1:** Pore water velocity field in myr<sup>-1</sup>. **2:** salt concentrations in g/L.

### 3.2 *Thermohaline convection*

Thermohaline convective flows are driven by buoyant forces induced by temperature and concentration gradients. In this case, a criterion to predict the onset of instabilities is based on the Rayleigh theory. The key dimensionless number is the Rayleigh number ( $Ra$ ), which is the ratio between buoyancy-driven forces and resisting forces caused by diffusion and dispersion. For sufficiently high values of  $Ra$  greater than some critical  $Ra_c$  instabilities will occur in the form of fingers or plumes. This critical Rayleigh number defines the transition between dispersive/diffusive solute transport ( $Ra < Ra_c$ ) and convective transport by density-driven fingers ( $Ra > Ra_c$ ). The Rayleigh stability criterion is discussed in more detail in Appendix 4.

While Rayleigh theory can be successfully used for the study of convective flow in homogenous systems (e.g. at laboratory scale) its applicability for transport processes within geothermal system is seriously questioned (Simmons et al. 2001). This criterion assumes that a steady-state flow takes place in an homogeneous system. Furthermore stability analyses based on dimensionless numbers involve the definition of a characteristic length scale of the porous media through which the temperature and solute gradients are supposed to vary linearly. In all transport processes occurring within real basin systems, such as the NEGB, these conditions are not satisfied. The physical parameters of the basin are subject to large heterogeneities. The brine density model described in paragraph 1.2.3 displays an unstable density profile in which concentration gradients are not linear. The thicknesses of the stratigraphic units of the NEGB can vary from a few meters to some kilometers because of the strong salt tectonics. Therefore, the definition of a representative length scale is rather problematic. Moreover, owing to the steady-state flow assumption made in Rayleigh's theory, the critical number  $Ra_c$  cannot provide information about the temporal evolution of the convective flow regime. From these considerations, it follows that the Rayleigh criteria is not convenient (if not impossible) for analyzing density-driven flow within the NEGB. Therefore instead of this dimensionless approach, the fully dimensional equations are used (Eq.(2.1), to Eq.(2.6)).

Thermohaline convection can be either (Oldenburg and Pruess 1998): (1) fingered, where narrow, finger-shaped plumes protrude upwards and/or downwards within the system; (2) penetrative, where convection cells penetrate upwards from the bottom of the system to the



top; (3) layered where convection occurs in stacked convective cells. When there is no convection the system is termed static or conductive.

Since in the NEGB temperature and salinity increase with depth, the destabilizing potential comes from the temperature gradient while the concentration gradient is stabilizing. This regime, also referred to as (double-)diffusive, favors oscillatory instabilities (Nield 1968). Simulation results show that the NEGB system is static in the Buntsandstein and fingered convection occurs in the overburden.

### 3.2.1 Boundary conditions

The boundary conditions defined for the thermohaline problem are the followings:

- The surface is open to solute and heat outflow. The head boundary condition is either set to a constant value of 25 m in the free convection problem, so that the regional flow is effectively removed from the model, (paragraph 3.2.2) or to the topographic level, used for in the mixed convection (in the paragraph 3.3.3).
- At Top Salt a fixed concentration value of 345.2 g/L has been set.
- At the basement a constant temperature boundary condition is defined. The value is set to 150 °C which corresponds to a linear vertical gradient of 30 °C/km.
- The lateral boundaries are closed to fluid, heat and mass flow

The boundary condition for brine concentration at the surface allows solute outflow through a thin stratum in contact with the top surface of the domain, as defined in paragraph 3.1.1. Since in thermohaline convection solute and thermal effects are strongly coupled, an open boundary condition, allowing heat outflow through the domain surface, is defined in analogy to mass outflow:

$$\mathbf{q}_T(t) = -\Phi_T(T^* - T)\mathbf{n}, \quad (3.4)$$

where  $\mathbf{q}_T$  is the heat flux,  $\Phi_T$  is a heat transfer coefficient,  $T^*$  is the prescribed boundary condition value for the temperature  $T$  at the surface, and  $\mathbf{n}$  is the vector normal to the surface of the domain. If  $\Phi_T = 0$  the boundary is adiabatic while when  $\Phi_T \rightarrow \infty$ ,  $T \rightarrow T^*$  and therefore the Cauchy boundary condition is reduced to a Dirichlet-type. As for the mass transfer coefficient (Eq.(3.3)), the heat transfer coefficient  $\Phi_T$  can be estimated by rewriting Eq.(3.4) in a Fourier form, viz.:

$$q_T(t) \approx -\lambda_{tr} \frac{T^* - T}{d} \quad (3.5)$$

where  $d$  is the thickness of the heat transition layer. The heat transfer coefficient becomes:

$$\Phi_T \approx \frac{\lambda_{tr}}{d} \quad \text{in } [Jm^2s^{-1}K^{-1}] \quad (3.6)$$

where  $\lambda_{tr}$  represents a heat conduction coefficient of a thin transition stratum.  $\lambda_{tr}$  can be considered more or less equal to the thermal conductivity of the bordering stratigraphic unit (i.e. Cenozoic,  $\lambda_{tr} \approx 1.5 Jms^{-1}K^{-1}$ , Table 1.1). Assuming that surface heat and mass transfer occurs in the same thin stratum in contact with the top surface,  $d \sim 1$  m. Hence from Eq.(3.6)  $\lambda \approx 1.5 Jm^2s^{-1}K^{-1}$ . The prescribed surface boundary condition  $T^*$  has been set equal to the reference temperature value at the surface, i.e.  $T^* = 8$  °C.

### 3.2.2 Free convection

In this paragraph the results of free convection simulations are presented, in order to investigate the dynamics of thermohaline convection within the NEGB in the absence of regional flow. The numerical results will emphasize the importance of temperature gradients in driving saline water to the surface. Although concentration and temperature distribution are depicted separately, it is worth recalling that in thermohaline convective flow mass and heat transport are strongly coupled and therefore these processes must not be seen as independent.

Fig.3-8 shows the brine concentration at a computing time of 30 ka (A) and at 200 ka (B). While in the Buntsandstein the concentration profile varies linearly from 200 g/L to 345 g/L, as previously, in salt diapir environments brine plumes develop rapidly and penetrate the overburden (Fig.3-8A). Compared to the other part of the profile, a strong brine fingering affects the eastern end of the cross-section. This behaviour is particularly pronounced at the western part of the basin where narrow salty plumes with 1 g/L of dissolved halite are close to or reach the surface. At the end of the simulation (Fig.3-8B), the mass pattern above the Buntsandstein displays two different features:

## Free thermohaline convection: Brine concentration (g/L)

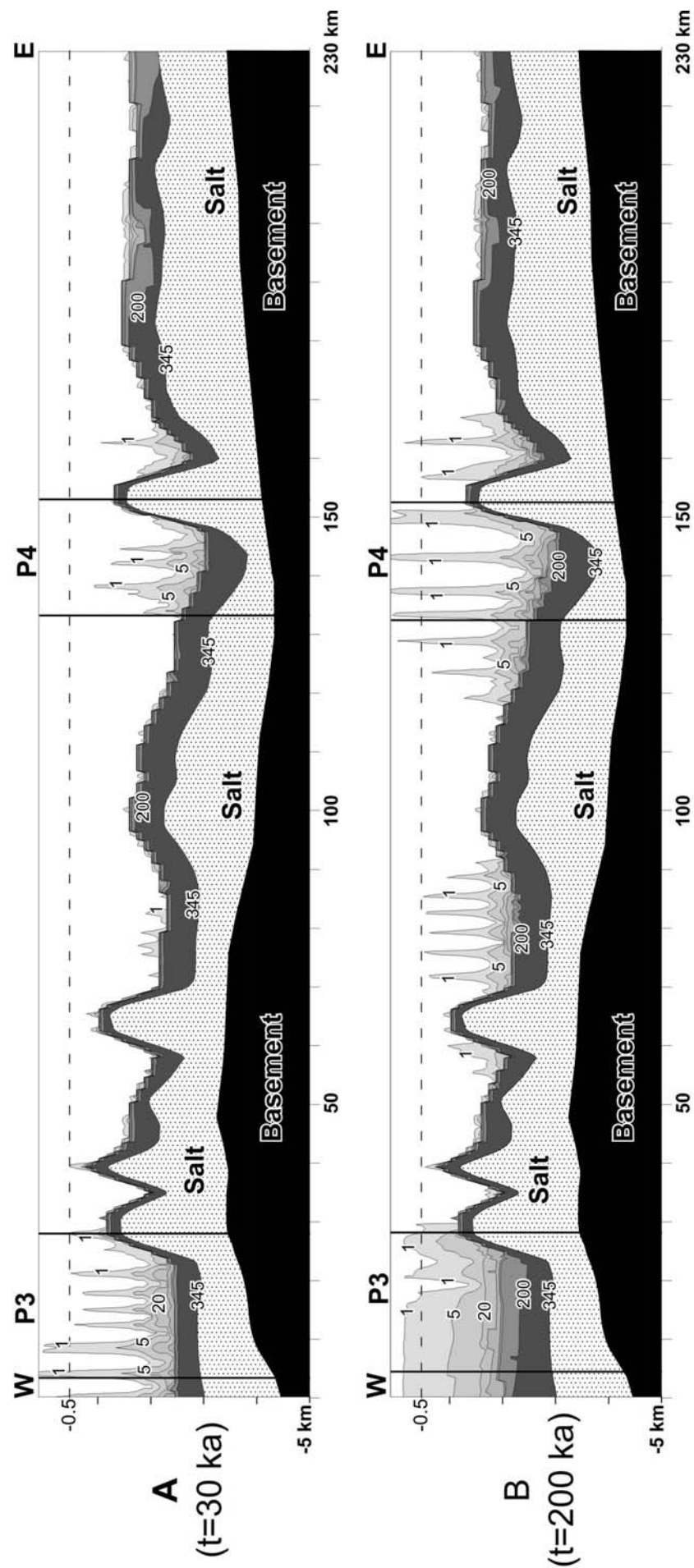


**Fig.3-8: A and B:** Mass distribution resulting from free thermohaline simulation at  $t = 30$  ka and  $t = 200$  ka respectively. Salt concentrations are expressed in g/L. Two profiles P3 and P4 are located within the cross-section. The simulation results for these two profiles are shown with no vertical exaggeration in Fig.3-10 and Fig.3-11

## Free thermohaline convection: Temperature (°C)

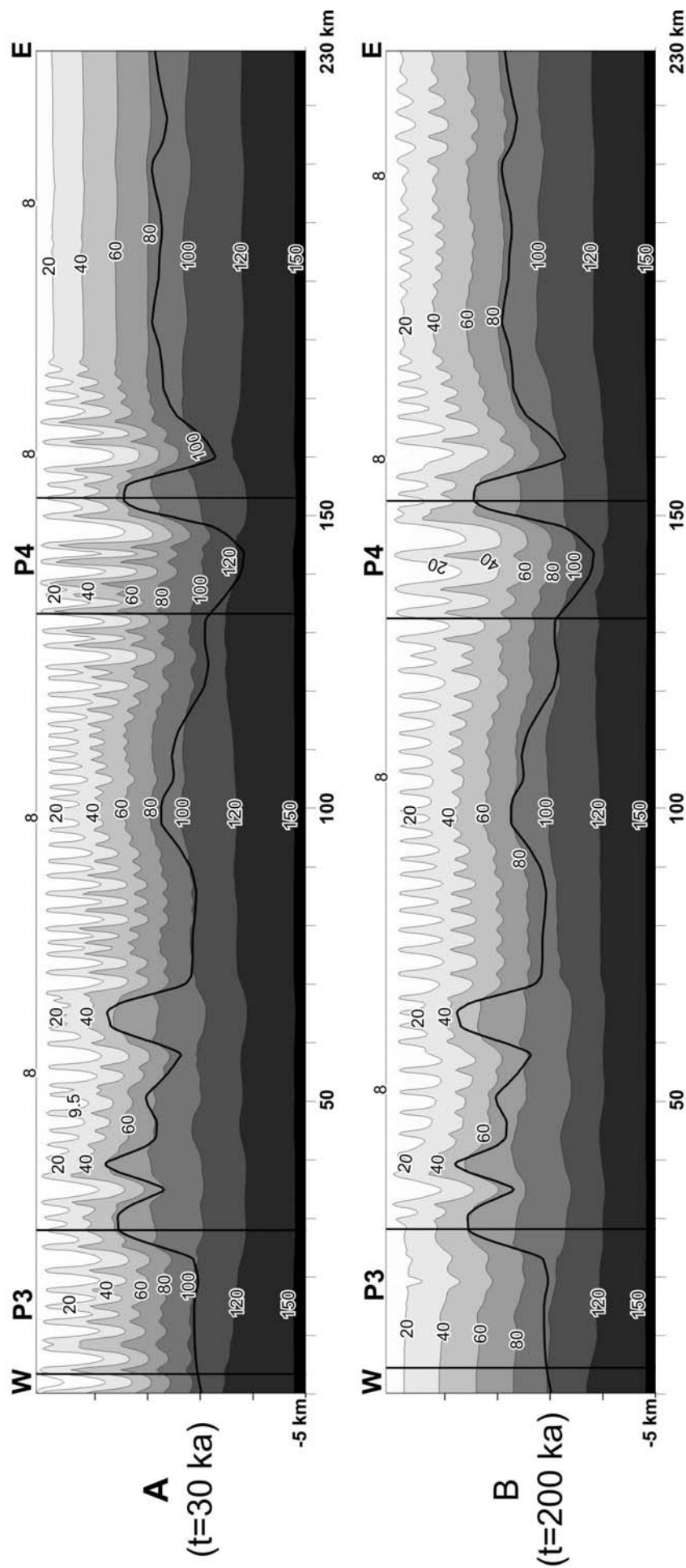


**Fig.3-9: A and B:** Temperature distribution resulting from free thermohaline simulation at  $t = 30$  ka and  $t = 200$  ka respectively. Temperatures are expressed in °C. Two profiles P3 and P4 are located within the cross-section. The simulation results for these two profiles are shown with no vertical exaggeration in Fig.3-10 and Fig.3-11

- At the western part of the basin, the finger regime disappears at the end of the simulation. Instead, the concentration isopleths are flat and the salt content increases almost linearly with depth. However, in the neighbourhood of the salt dome, a depressed concentration gradient is displayed. The layered brine stratification is likely a boundary effect. Since the lateral boundaries of the model are closed to fluid flow, mass and heat transfer, the dissolved halite cannot diffuse away in the western direction. Moreover, salt diffusion in the eastern direction is also prevented due to the presence of shallow salt diapirs. Therefore, as time progresses, the sediments are filled with halite. The finger regime evolves into a layered system in which concentration increases with depth.
- Within the rest of the basin, the fingers have kept on protruding even after 200 ka. The salty plumes have reached half a kilometre depth in the central part of the basin. At the 150<sup>th</sup> km mark near the salt diapir, slender brackish fingers extend over 3 km throughout the sediments up to the surface. On the other hand, at the eastern part of the basin, far from the salt dome, no salty plumes develop.

The temperature field (Fig.3-9) displays a disturbed profile throughout the sediment fill above the Zechstein unit. These oscillatory patterns are characteristic of a multicellular convective regime and already occur at early time stages (Fig.3-9 A,  $t = 30$  ka ). The waves are non-periodic and their amplitude decreases with depth. At the eastern part of the basin, far from the salt diapir the temperature distribution is not less disturbed. The temperature gradient did not diverge from the initial conditions and increases linearly with depth. Below the Zechstein unit the temperature profile is everywhere conductive showing the well-known thermal anomalies within the salt diapirs (i.e. concave temperature isopleths). At  $t = 200$  ka (Fig.3-9 B), the temperature profile still displays convective oscillations above the Zechstein. However, at the western part of the basin, the temperature isopleths are nearly flat presenting only one anomaly near the salt dome. Minor temperature oscillations have developed at the eastern part of the basin. On the other hand, the conductive regime dominates in the sediments below the Zechstein unit.

Fig 3.8 and 3.9 provided a regional picture of mass and temperature distribution within the whole cross section. The calculated patterns show both features of thermohaline and static regime: brine fingers penetrate in the sediments above the Buntsandstein unit, the thermal anomalies are manifested as non-periodic waves which intensity decreases with depth. As time progresses, a layered stratification of the brine concentration is achieved at the western part of the basin. On the other hand, the concentration profile within the Buntsandstein unit is steady and increases linearly up to the saturation value (345 g/L) at top salt. Therein the temperature profile is slightly disturbed and becomes conductive below the Zechstein unit.

In order to gain insights into the geometry of the convective cells and to quantify their effects on the mass and temperature field, the simulation results are illustrated with no vertical exaggeration for two profiles (denoted with “P3” and “P4” in Fig.3-8 and Fig.3-9) in Fig.3-10 and Fig.3-11 respectively. Early in the simulation process, the profile P3 is affected by a sequence of convective cells in the west-east direction (Fig.3-10 A). The cells extend from a depth of 2 km up to the surface. The cells geometry displays broad areas of recharge (2-3 km wide) with downward directed flow and narrow discharge areas (500 m) up to the surface. The pore water velocities range from  $1.5 \text{ cm yr}^{-1}$  at the bottom of the cell to  $0.3 \text{ m yr}^{-1}$  at the surface. Along the salt edge of the diapir, groundwater flows downward at  $1.5 \text{ cm yr}^{-1}$ . Throughout the profile, salty fingers develop in relation to upward convective flow (Fig.3-10 A2). At the western part of the basin, a salty plume reaches the surface. At that location, brine with 1.2 g/L of dissolved halite leaches throughout the surface at  $0.3 \text{ m yr}^{-1}$ . Within the Buntsandstein the concentration gradient is linear due to salt diffusion. The temperature field (Fig.3-10 A3) presents oscillatory thermal anomalies down to 2 km of depth because of the convective regime. The amplitude of the waves decreases with increasing depth. Below the Top Zechstein, the heat regime is conductive, presenting flat isopleths. Owing to the natural boundary condition at the surface, temperature values higher than the reference surface value (i.e.  $8^{\circ}\text{C}$ ) occur in association with increased temperature gradients. The temperature values at the surface span between  $8^{\circ}\text{C}$  and  $9.6^{\circ}\text{C}$ . A straightforward relation between the thermally induced convective cells, the mass and the temperature fields is inferred by comparing Fig.3-10 A1 with Fig.3-10 A2 and A3. Concentration and temperature distributions show broad areas of fresh and cooler water in the recharge zone while narrow salty and warmer plumes occur in the up-flows. Peak brine concentration and temperature values at the surface are associated with vigorous upward flow induced by thermal convection as it is the case at the western part of the basin.

At the end of the simulation run, the convective regime throughout the profile vanishes (Fig 3.10 B1). The vectors show stagnation zones with very low pore velocities in which a diffusive/conductive regime has been achieved. Only two weak convective cells recharge the sediments in the shallow aquifer at the eastern part of the profile. In relation to these downward freshwater flows, concentration and temperature display a depressed profile (Fig.3-10 B2, B3).

As in Profile 3, Profile 4 reveals an intense convective regime at early time stage (Fig.3-11 A). Here the recharge areas are larger (3-5 km wide) and upward flows discharge to the surface at higher rates ( $0.3\text{-}0.4 \text{ myr}^{-1}$ ). Thermally induced brine fingers begin to protrude within the sediment fill (Fig.3-11 A2), reaching a depth of approximately 1 km below the

surface. The temperature field presents the same features described previously: a non-periodic convective oscillatory regime affects the profile down to 2 km depth. The amplitudes decrease with depth and a conductive regime is achieved below the Zechstein Salt.

At  $t = 200 \text{ ka}$ , the thermohaline finger regime persists (Fig.3-11 B). The pore velocities have drastically decreased ( $7 \text{ cm yr}^{-1}$  to  $0.2 \text{ m yr}^{-1}$ ) as more saline and heavier water has been advected up to the surface (Fig.3-11 B2) by thermal buoyant forces. At the surface, brine concentrations range from 1 to 1.6 g/L. On the other hand, the downward flow forms broad areas of freshwater which shape the trough between the brine fingers. In relation to the narrow brine plumes and the wide freshwater cells, the subsurface temperature gradient is respectively increased or depressed (Fig.3-11 B3). Consequently, the surface temperature is higher than or equal to the reference temperature value ( $8^{\circ}\text{C}$ ). Peak values of discharge flow, brine concentration and fluid temperature at the surface occur at the eastern part of the profile.

From the numerical simulation, it turns out that saline and thermal plumes rose together spreading over the same areas within the sediment fill. This feature is displayed in Fig 3.10 A and in Fig.3-11 A and B. This phenomenon characterizes the strong coupling of heat and mass transfer in thermohaline convection and is explained by Oldenburg and Pruess (1998;1999): because of the thermal retardation factor (Eq.(1.18), Appendix 1) the concentration front tends to advance ahead of the temperature front; however, the increased salt concentration at the leading edge of the brine plume diminishes upward buoyancy force. Therefore, owing to this lack of positive buoyancy the brine cannot advance beyond the region of increased temperature. The brine and the temperature plume reach the same height occupying the same region. The heat retardation factor induces the formation of a “density lid” at the top of the brine plumes. Oldenburg and Pruess (1998;1999) suggest that the presence of density lids can promote lateral flow of the plume. Accordingly, in Fig.3-11 B2 the brine finger at the eastern part of the profile presents a bifurcated tip spreading laterally at both sides of the plume.

**Figure 10: Evolution of the subsurface system at 30 ka and 200 ka.**

The figure displays six panels arranged in a 3x2 grid, showing the evolution of the subsurface system at two different times:  $t=30\text{ka}$  (left column, A) and  $t=200\text{ka}$  (right column, B). The rows represent different variables:

- Row 1: Velocity field ( $\text{myr}^{-1}$ )**
  - Panel A (left): Shows velocity contours with values ranging from  $1.5 \times 10^{-3}$  to  $7 \times 10^{-3}$ . The contours are more complex and localized near the surface.
  - Panel B (right): Shows velocity contours with values ranging from  $1 \times 10^{-3}$  to  $2 \times 10^{-3}$ . The contours are more uniform and spread out.
- Row 2: Brine concentration (g/L)**
  - Panel A (left): Shows brine concentration contours with values ranging from 5 to 20 g/L. The contours are more irregular and localized.
  - Panel B (right): Shows brine concentration contours with values ranging from 5 to 20 g/L. The contours are more uniform and spread out.
- Row 3: Temperature ( $^{\circ}\text{C}$ )**
  - Panel A (left): Shows temperature contours with values ranging from 20 to 120  $^{\circ}\text{C}$ . The contours are more irregular and localized.
  - Panel B (right): Shows temperature contours with values ranging from 20 to 120  $^{\circ}\text{C}$ . The contours are more uniform and spread out.

Each panel includes a vertical axis for depth (0 to 28 km) and a horizontal axis for distance (0 to 4 km). The panels show the progression of the salt wedge and the development of the P3 zone over time.

GeoForschungsZentrum Potsdam  
Scientific Technical Report STR 05/12



# Free thermohaline convection: Profile P4

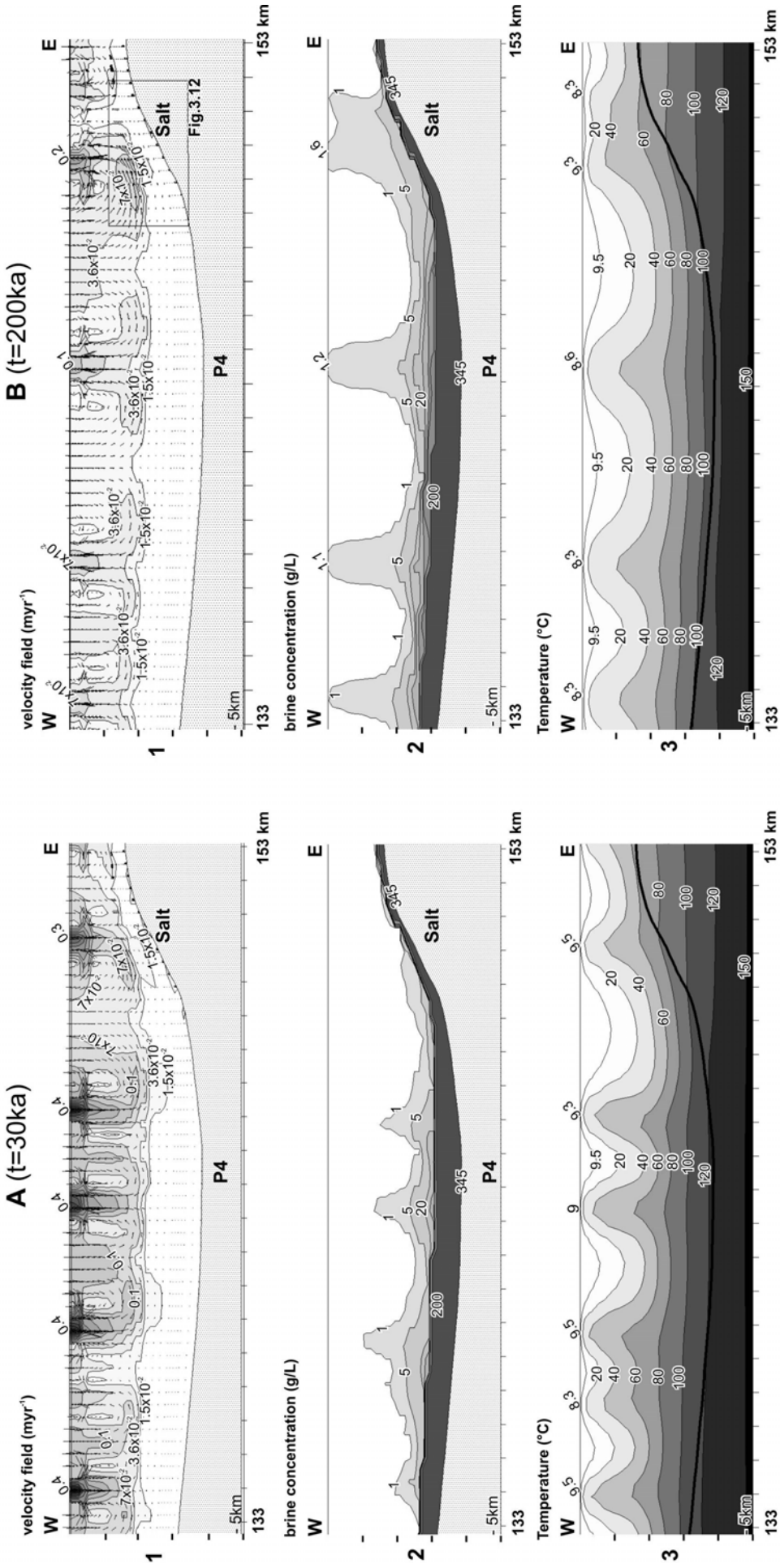


**Fig.3-11: A and B:** Zoom of the thermohaline simulation results for profile P4 as located in Fig.3-8 at  $t = 30\text{ ka}$  and  $t = 200\text{ ka}$  respectively. No vertical exaggeration is used. **1:** Pore water velocity field in  $\text{myr}^{-1}$ . Pore vector linearly scaled to the largest flow arrow. **2:** salt concentrations in g/L. **3:** temperature distribution in  $^{\circ}\text{C}$ . The rectangle locates a salt diapir flank. Velocity and temperature field within this salt diapir environment are further illustrated in Fig.3-12

An additional feature of thermohaline convection is the presence of an upward flow in the neighbourhood of salt diapirs. A zoom of the calculated pore velocity and temperature fields in a salt dome environment is shown in Fig.3-12. Downward forces resulting from the gravitational field control groundwater flow along salt diapirs flank. The salt-laden water sinks at approximately  $1.5 \text{ cm yr}^{-1}$  (Fig.3-11 (1)). However an upward flow paralleling this descending flow occurs in the overlying unit at approximately  $1 \text{ cm yr}^{-1}$ . This phenomenon can be explained by the temperature distribution (Fig.3-12 (2)). Because of the thermal conductivity contrast between salt and overlying sediments the isotherms are convex near the edge of the salt diapir. The increased temperature gradient causes a decrease in fluid density near the salt dome. This drives the groundwater flow toward the salt dome and initiates the uprising circulation of brine within the neighbouring sediments. The thermally induced upward flow counteracts the downward brine motion occurring along the salt edge. As a result, a thin boundary layer displaying zero pore water velocities develops between the two opposed flows. Free thermohaline convection near salt diapirs has been numerically investigated by Evans et al. (1989 ; 1991). In their studies, the authors tested the effects of different thermal conductivity ratio in the sediments overlying a salt diapir and found that elevated isotherms near salt diapirs can generate thermally induced upward brine circulation.

In summary, temperature effects on brine transport are inferred by comparing the results of pure diffusive brine transport (Fig.3-1) and free thermohaline simulations (Fig.3-8). At an early time stage of the pure diffusive regime (Fig.3-1 A) dissolved halite diffuses along the salt domes edges in the deep sediments. On the other hand, in free thermohaline convection (Fig.3-8 A) stretched salty plumes develop in salt dome environments and protrude vertically throughout the overburden. At the end of the simulation run, in the case of pure diffusive brine transport (Fig.3-1 B), the salty plumes are layered, extending laterally from the salt diapirs flanks over 30 km. Brines with 1 g/L of dissolved salt occur at a depth between 1 km and half a kilometre and do not reach the surface whereas the concentration field resulting from thermohaline simulations (Fig.3-8 B) reveals both subsurface brine occurrence and finger patterns leaching through the surface.

## Free thermohaline convection: Salt flank profile

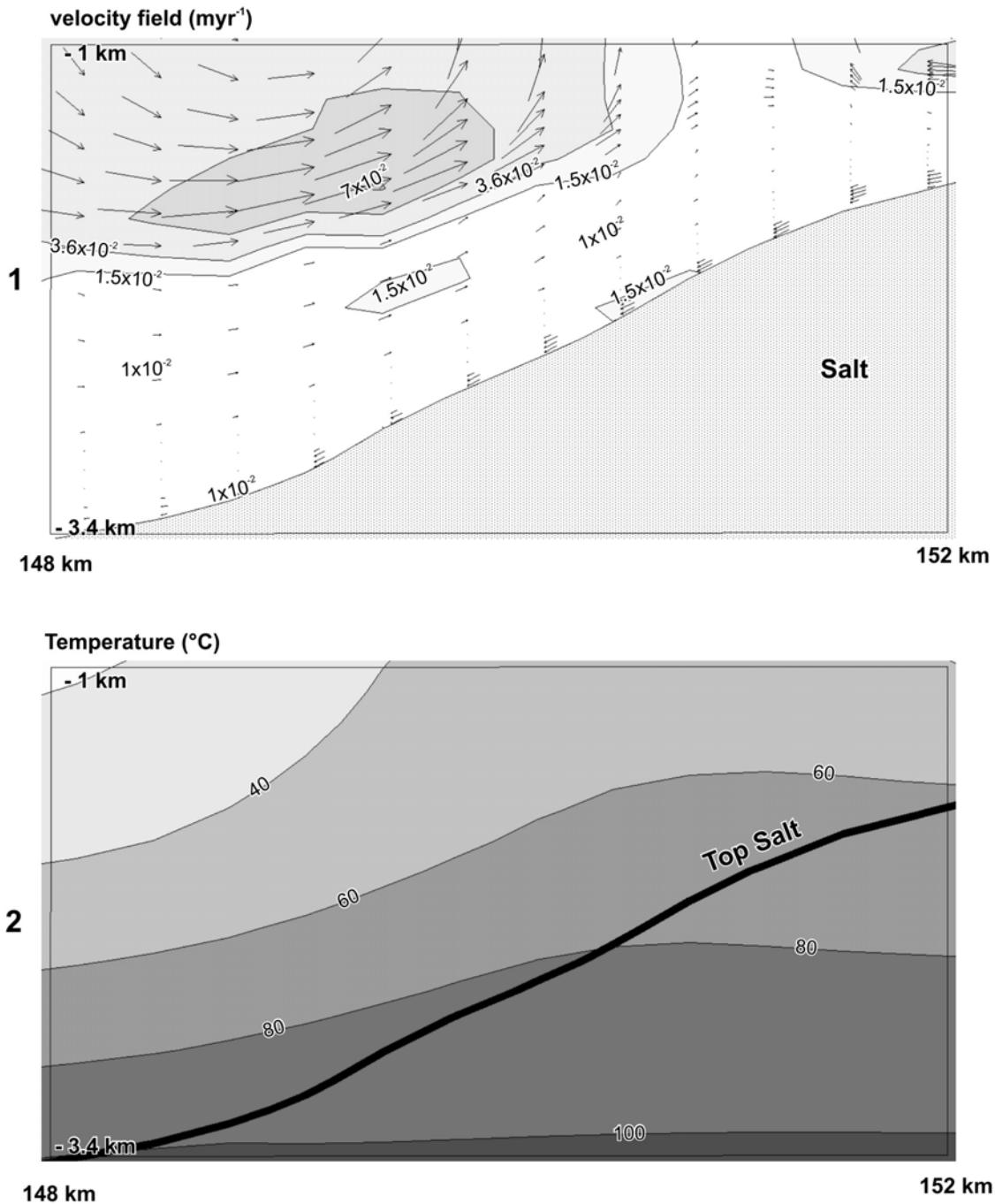


**Fig.3-12:** Zoom of thermohaline simulation results in the salt dome environment as located in Fig.3-11  
**1:** Pore water velocity field in myr<sup>-1</sup>. Pore vector linearly scaled to the largest flow arrow. **2:** temperature distribution in °C

In diffusive regimes, pore water velocities range between a few millimetres to 1.5 cm per year along salt diapir flanks (Fig.3-2 and Fig.3-3). Thermally buoyant forces instead generate convective cells advecting solute up to the surface at 10-20 cm yr<sup>-1</sup> (Fig.3-10 and Fig.3-11). Furthermore, the buoyant forces resulting from increased temperature gradients in the sediments overlying the edges of salt diapirs are strong enough to overcome the gravitational field. Consequently upward flow of deep seated salty water occur along salt domes (Fig.3-12),

These features do not occur in the pure diffusive case in which only downward and lateral brine migration can be observed (compare Fig.3-12 with Fig 3.3).

A general aspect of the thermohaline regime is the strong coupling of heat and mass transport which is manifested by salty and thermal plumes rising together and spreading over the same areas (Fig.3-10 and Fig.3-11)

### **3.2.3 Mixed convection**

When an external factor such as head-driven groundwater flow (forced convection) is imposed on a free thermohaline system the resulting regime is referred to as mixed convection. Here the head level is set equal to the topographic relief so that regional and thermally induced flow occur together. In this paragraph, the results from free thermohaline and mixed convection are compared in order to demonstrate the effects of the regional flow on the thermally induced flow.

In Fig.3-13, the brine concentration profile resulting from mixed convection is illustrated together with the simplified regional flowlines. The mass distribution shows significant differences with regard to the profile derived from the free thermohaline simulation (Fig.3-8).

In the mixed convection regime, the thermally induced brine patterns are affected by the regional flow: the narrow salty fingers observed in the free thermohaline regime (Fig.3-8) evolve into a smaller number but larger brine plumes which reach the surface at the discharge areas (Fig.3-13). On the other hand, the brine patterns display a truncated profile in direct relation to the downward flow of freshwater.

The regional flow strongly influences heat transport as well. The short wavelengths of the temperature oscillations characterizing the free thermohaline regime (Fig.3-9) are not preserved in the mixed convection system (Fig.3-14). The isotherms are shaped by the regional flow: in the recharge areas, the infiltration of cooler water depresses the temperature gradient whereas uprising of hot plumes occur in relation to the discharge areas.

## Mixed convection: Brine concentration (g/L)

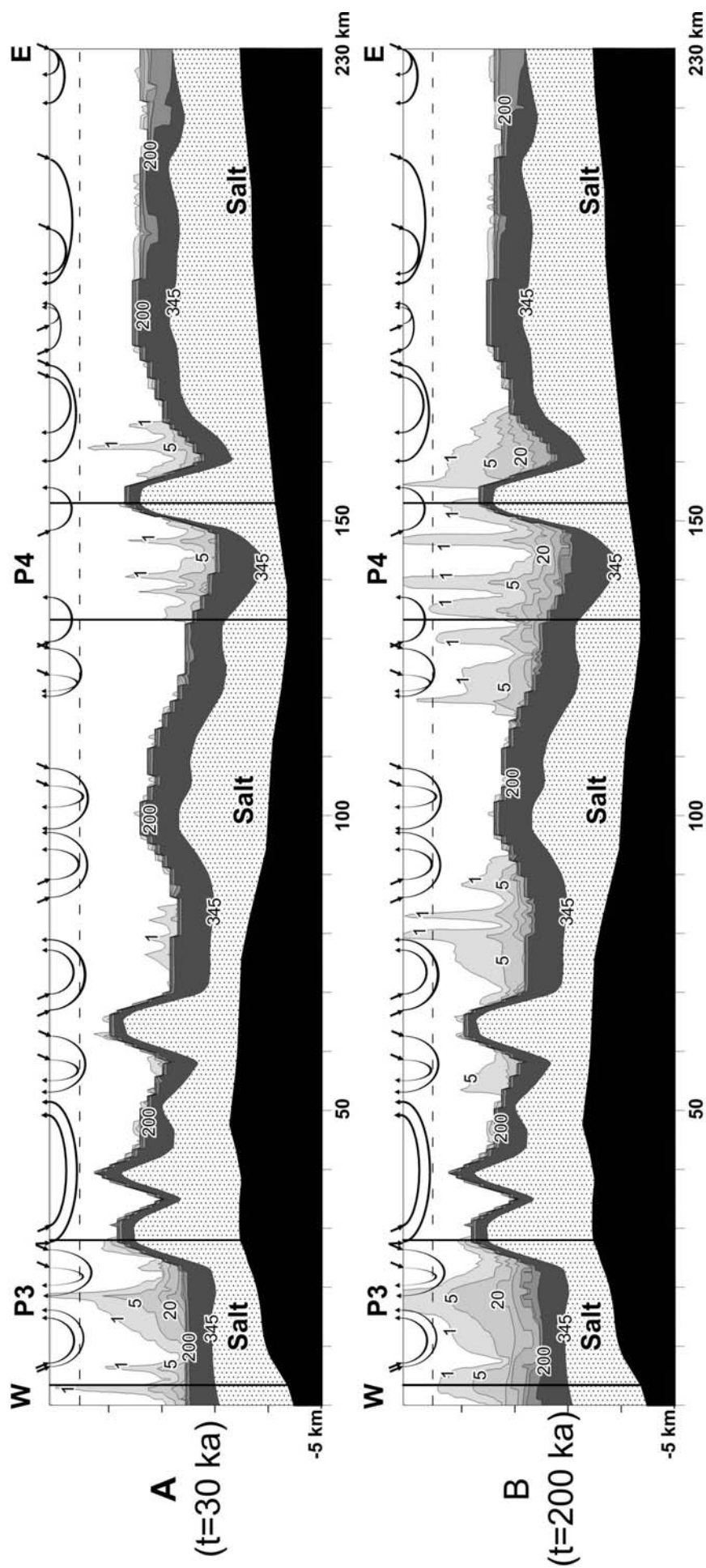


**Fig.3-13: A and B:** Mass distribution resulting from mixed convection simulation at  $t = 30$  ka and  $t = 200$  ka respectively. Salt concentrations are expressed in g/L. Two profiles P3 and P4 are located within the cross-section. The simulation results for these two profiles are shown with no vertical exaggeration in Fig.3-15 and Fig.3-16

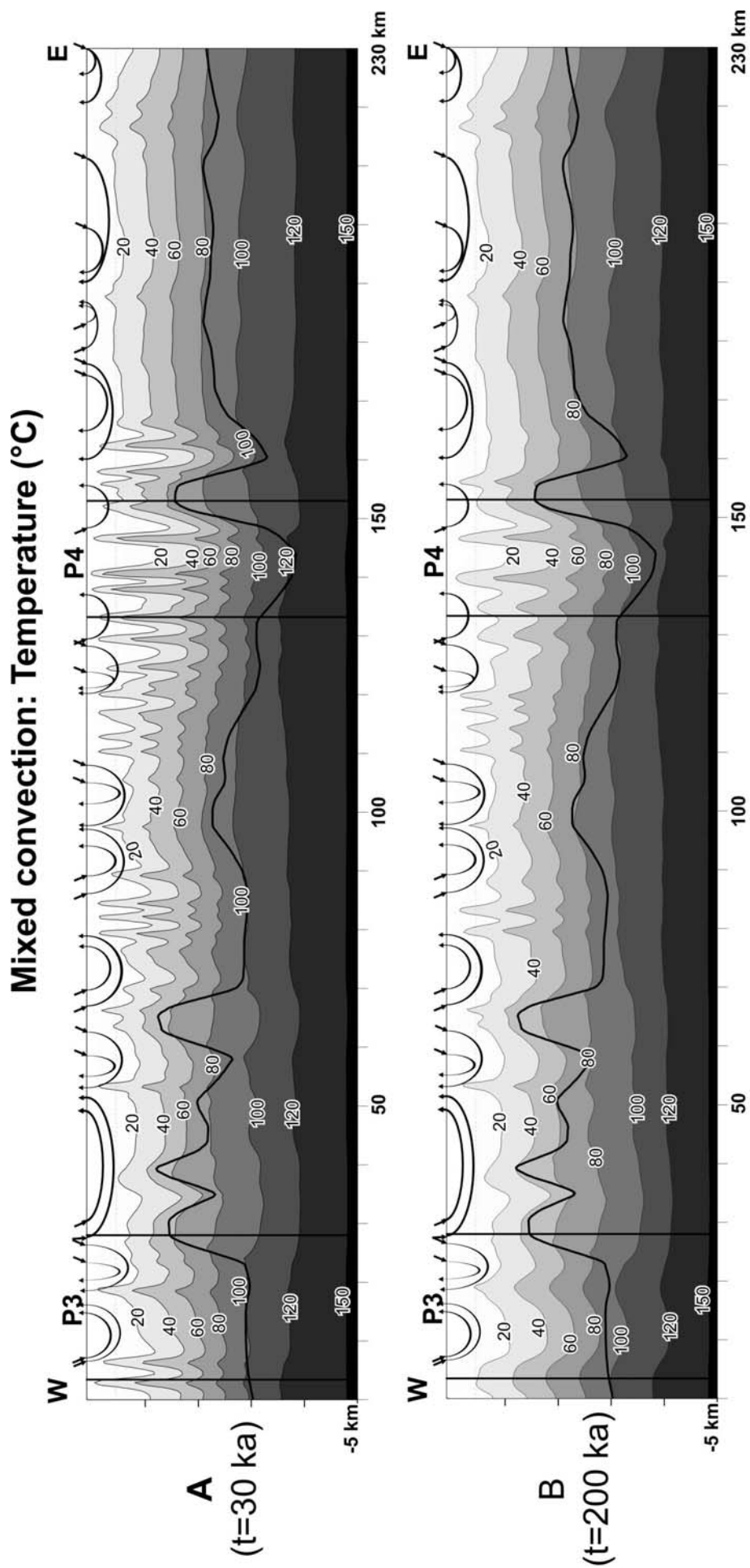


**Fig.3-14: A and B:** Temperature distribution resulting from mixed convection simulation at  $t = 30$  ka and  $t = 200$  ka respectively. Temperatures are expressed in °C. Two profiles P3 and P4 are located within the cross-section. The simulation results for these two profiles are shown with no vertical exaggeration in Fig.3-15 and Fig.3-16

Additional insights into these general features of the mixed convection regime are derived from the time dependent analysis of velocity, brine and temperature fields. The two profiles “P3” and “P4” are illustrated without vertical exaggeration in Fig.3-15 and Fig.3-16 respectively at two computing time steps (A:  $t = 30 \text{ ka}$  , B:  $t = 200 \text{ ka}$  ).

At the begin of the simulation process, the velocity field P3 (Fig.3-15 A1) displays thermally induced convective cells only at the western end of the section below the shallow regional flow. Elsewhere, the convective cells which affect the profile in the free thermohaline regime (Fig.3-10 A1) are overwhelmed by the more vigorous regional flow. In relation to the persisting convective regime, a thermally induced brine plume begins to form at the western end of the profile (Fig.3-15 A2 B2). On the other hand, in the central part of the basin, both saline and thermal plumes are advected by the strong regional flow toward the discharge area. As time progresses, the western convective cells vanish (Fig.3-15 B1). Throughout the whole profile, solute and temperature isopleths are dragged parallel to the regional streamlines (Fig.3-15 B2 B3) and brine with 2 g/L spreads over the area of flow confluence.

In profile P4 (Fig.3-16) topography induced flow occurs at the eastern and western end of the profile at  $0.1 \text{ m yr}^{-1}$ . This relatively small flow rates play a minor role at early time steps (Fig.3-16 A). The thermohaline cellular patterns develop through the whole profile as in the free thermohaline regime (Fig.3-11 A), however with a slightly different spatial distribution. At the end of the simulation run (Fig.3-16 B1), the thermally induced cells weaken since more heavy brine has been advected upward. Therefore the convective cells are swallowed up by the overlying stronger regional flow. Consequently, the growth of brine and thermal plumes is inhibited by the horizontal freshwater flow (Fig.3-16 B2). The resulting patterns display flat fronts adjacent to the regional streamlines. By contrast, finger plumes continue protruding up to the surface in the central part of the profile where the regional flow is almost absent. Therein, solute and thermal fingers spread over the same area within the sediments fill (Fig.3-16 B2 B3), as in the free thermohaline regime.

The numerical results show that in mixed convection, head-driven flow plays an important role in controlling both brine and heat transport. When the regional flow is stronger than thermally induced flow, the hot brine is advected toward the discharge area. As a result, the plumes are shaped by regional flow patterns. On the other hand, in the areas of the basin where the regional flow rates are smaller than the thermally induced velocities, brine and thermal fingers self-develop as in a free thermohaline regime.

## Mixed convection: Profile P3

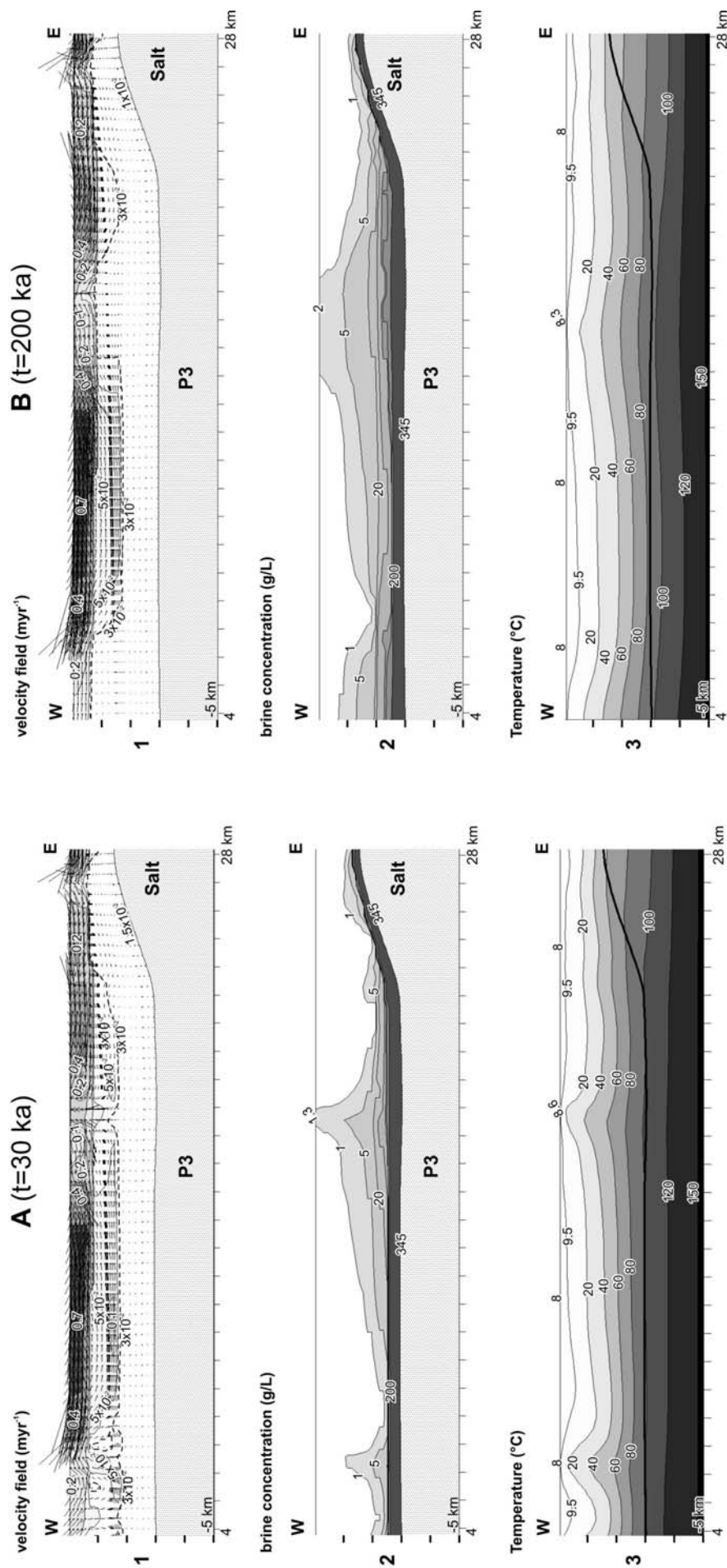


**Fig.3-15: A and B:** Zoom of the mixed convection results for profile P3 as located in Fig.3-12 at  $t = 30$  ka and  $t = 200$  ka respectively. No vertical exaggeration is used. **1:** Pore water velocity field in  $\text{myr}^{-1}$ . Pore vector linearly scaled to the largest flow arrow. **2:** salt concentrations in g/L. **3:** temperature distribution in  $^{\circ}\text{C}$



Mixed convection: Profile P4

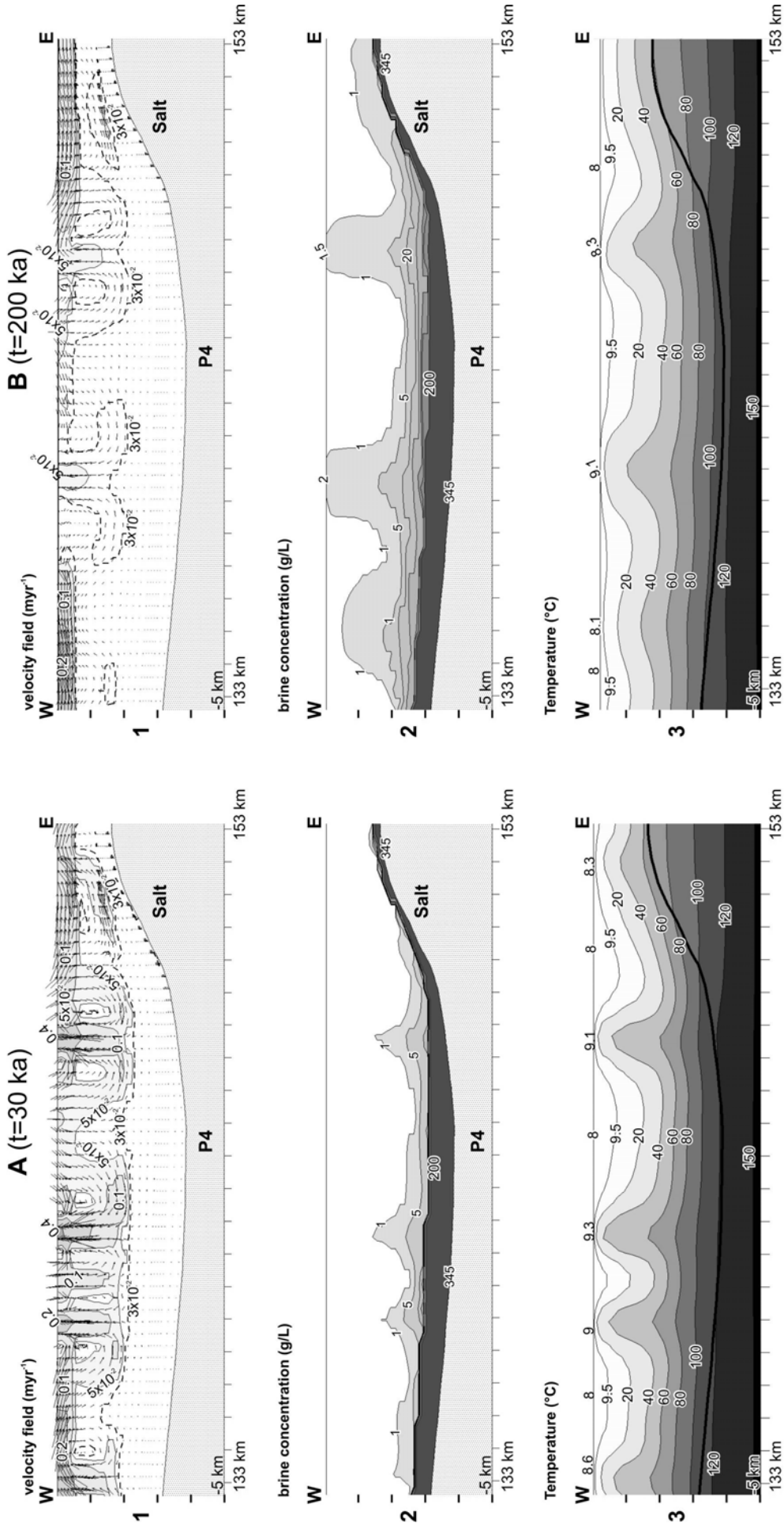
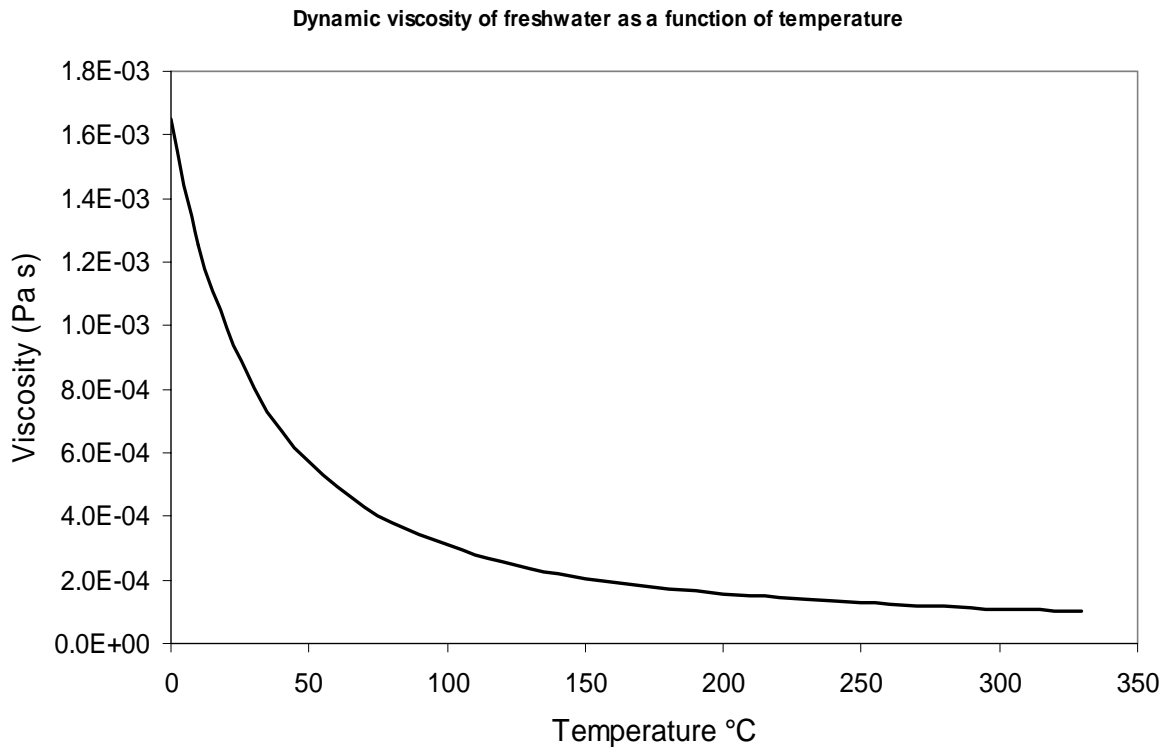


Fig.3-16: A and B: Zoom of the mixed convection results for profile P4 as located in Fig.3-12 at  $t = 30$  ka and  $t = 200$  ka respectively. No vertical exaggeration is used. 1: Pore water velocity field in  $\text{myr}^{-1}$ . Pore vector linearly scaled to the largest flow arrow. 2: salt concentrations in g/L. 3: temperature distribution in  $^{\circ}\text{C}$

### 3.2.4 Viscosity effects

Viscosity is a fluid property which strongly depends on temperature and salinity content. As shown in Fig.3.17, at freshwater condition an increase in temperature from 0 to 350 °C leads to a decrease in viscosity by over 1 order of magnitude.



**Fig.3.17:** Dynamic viscosity of freshwater as a function of temperature.

As seen in Eq.1.10 (Appendix 1), the hydraulic conductivity is inversely proportional to the fluid viscosity. Therefore the intrinsic hydraulic conductivity of the stratigraphic units increases with temperature. This enhances the instability of the layers and promotes thermal convection because of an increase of the Rayleigh number (Eq.4.1 and Eq.4.2, Appendix 4). Consequently, convective flows are more intense than in settings which neglect viscosity.

In this paragraph, viscosity effects on the mixed convective regime are investigated. In FEFLOW<sup>®</sup> 5 (WASY-GmbH 2002), concentration and temperature dependencies of the fluid viscosity can be included into the model by the use of empirical relationships as given by Lever and Jackson (1985) and by Mercer and Pinder (1974). The resulting brine patterns are illustrated in Fig.3.18 at two time steps (A:  $t = 30$  ka and B:  $t = 30$  ka ).

## Mixed convection and fluid viscosity: Brine concentration (g/L)

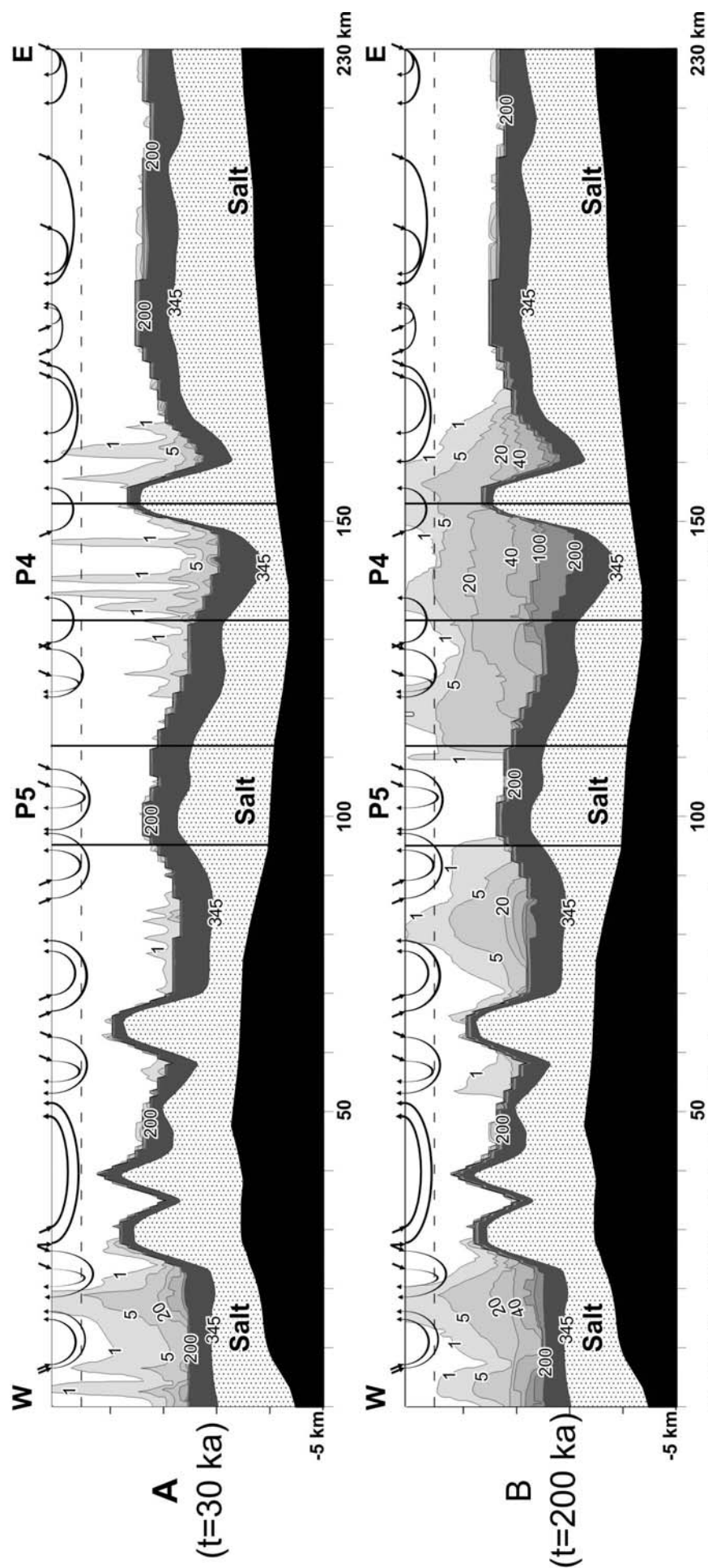


**Fig-3.18: A and B:** Mass distribution resulting from mixed convection and viscosity effects at t=30 ka and t=200 ka respectively. Salt concentrations are expressed in g/L. Two profiles P4 and P5 are located within the cross-section. The simulation results for these two profiles are shown with no vertical exaggeration in Fig.3.20 and Fig.3.21

## Mixed convection and fluid viscosity: Temperature (°C)

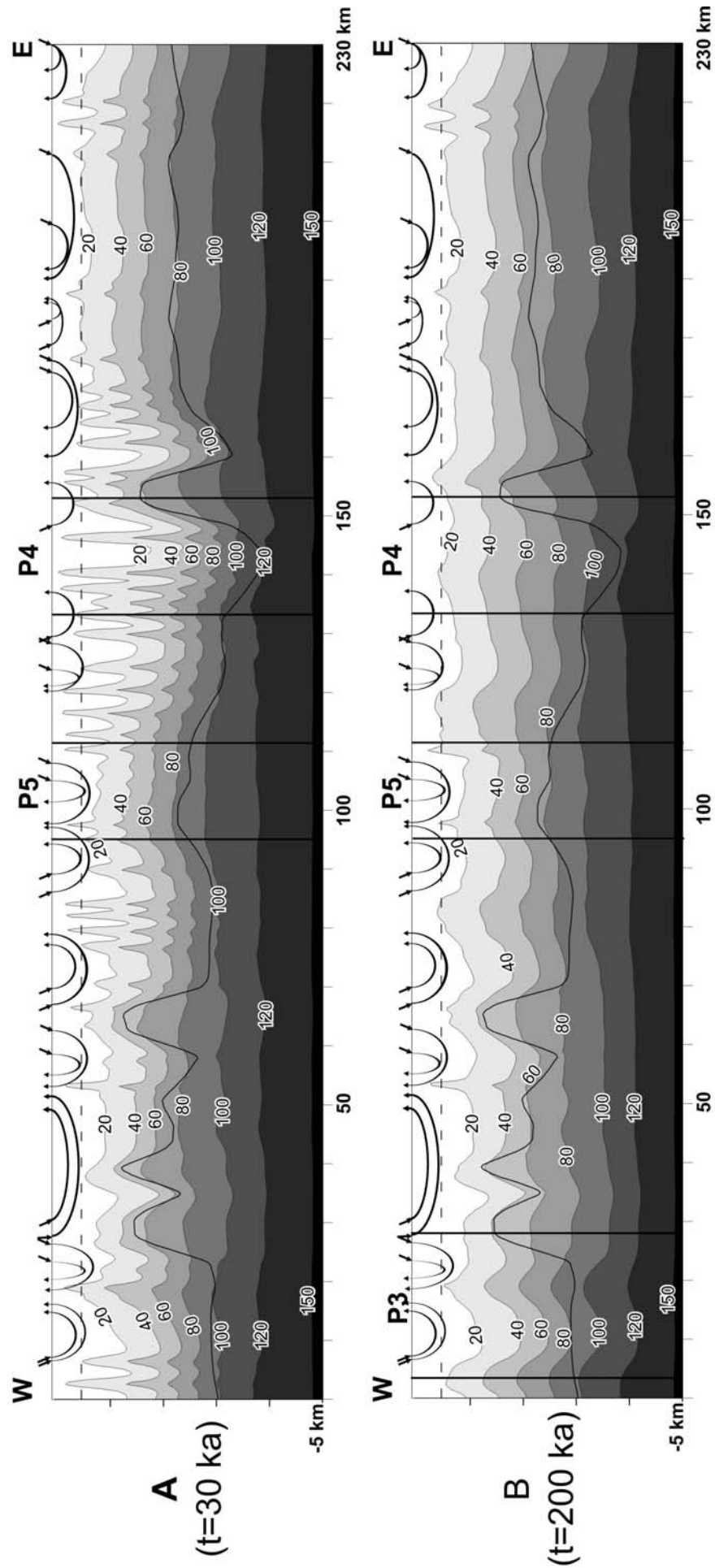


**Fig.3-19: A and B:** Temperature distribution resulting from mixed convection and viscosity effects at t=30 ka and t=200 ka respectively. Salt concentrations are expressed in g/L. Two profiles P4 and P5 are located within the cross-section. The simulation results for these two profiles are shown with no vertical exaggeration in Fig.3.20 and Fig.3.21

The effects of viscosity on the concentration field are inferred by comparing these patterns with those of the previous simulation in which viscosity dependencies are neglected (Fig.3.13 A, B). Viscosity variation strongly influences the salt concentration profile within the sediments. At early time stages, most of the brine fingers are stretched up to the surface (Fig.3.18 A) suggesting that a more vigorous upward brine flow takes place. As time progresses, the narrow brine fingers evolve in broader brine patterns shaped by the regional flow (Fig.3.18 B). Salty water with more than 2 g/L of dissolved halite spreads at the surface covering the discharge areas. The concentration isopleths are more pulled up when the viscosity is variable. Near the eastern salt diapir, waters with 20 g/L of dissolved halite reach 1 km depth (Fig.3.18B) whereas at constant viscosity these salty waters are embedded in the deeper part of the basin (Fig.3.13B). Furthermore, in the central part of the basin, the brine patterns display closer vertical fronts proving that viscosity variation can promote lateral brine flow as well. This area of the basin denoted by “P 5” will be illustrated in more details afterwards.

At early an time stage, the temperature profile displays oscillatory perturbations (Fig.3.19A) comparable to those observed with constant fluid viscosity (Fig.3.14 A). On the other hand, at the end of the simulation run (Fig.3.19 B), the isotherms are smoothed in association with a layered brine patterns.

Insights into the effects of viscosity on the flow regime are gained by comparing time dependent patterns for profile P4 in which viscosity is either constant (Fig.3.16) or variable (Fig.3.20). In the first case, at the begin of the simulation process, thermally induced brine plumes with 1 g/L of dissolved salt reach a depth of 1.5 km flowing at  $0.1 \text{ m yr}^{-1}$  (Fig.3.16 A1). On the other hand, at the same time step, when a variable viscosity is taken into account, brine plumes with 1g/L of dissolved salt flow through the surface at rates ranging from 0.2 to  $0.4 \text{ m yr}^{-1}$  (Fig.3.20 A1). This observation reflects the viscosity effects on the hydraulic conductivity. As previously explained, owing to the temperature dependence of the viscosity, the hydraulic conductivity increases with temperature. Therefore increased hydraulic conductivities occur in direct relation to the increased temperature gradients of the convective regime. Consequently, in these areas, the resulting flow is more intense. To some extent viscosity dependencies introduce permeability heterogeneities within the stratigraphic units of the basin. The sediments are locally more permeable where upward hot brine flows occur and the flow rates of thermally induced brine plumes are further enhanced.

## Mixed convection and fluid viscosity: Profile P4

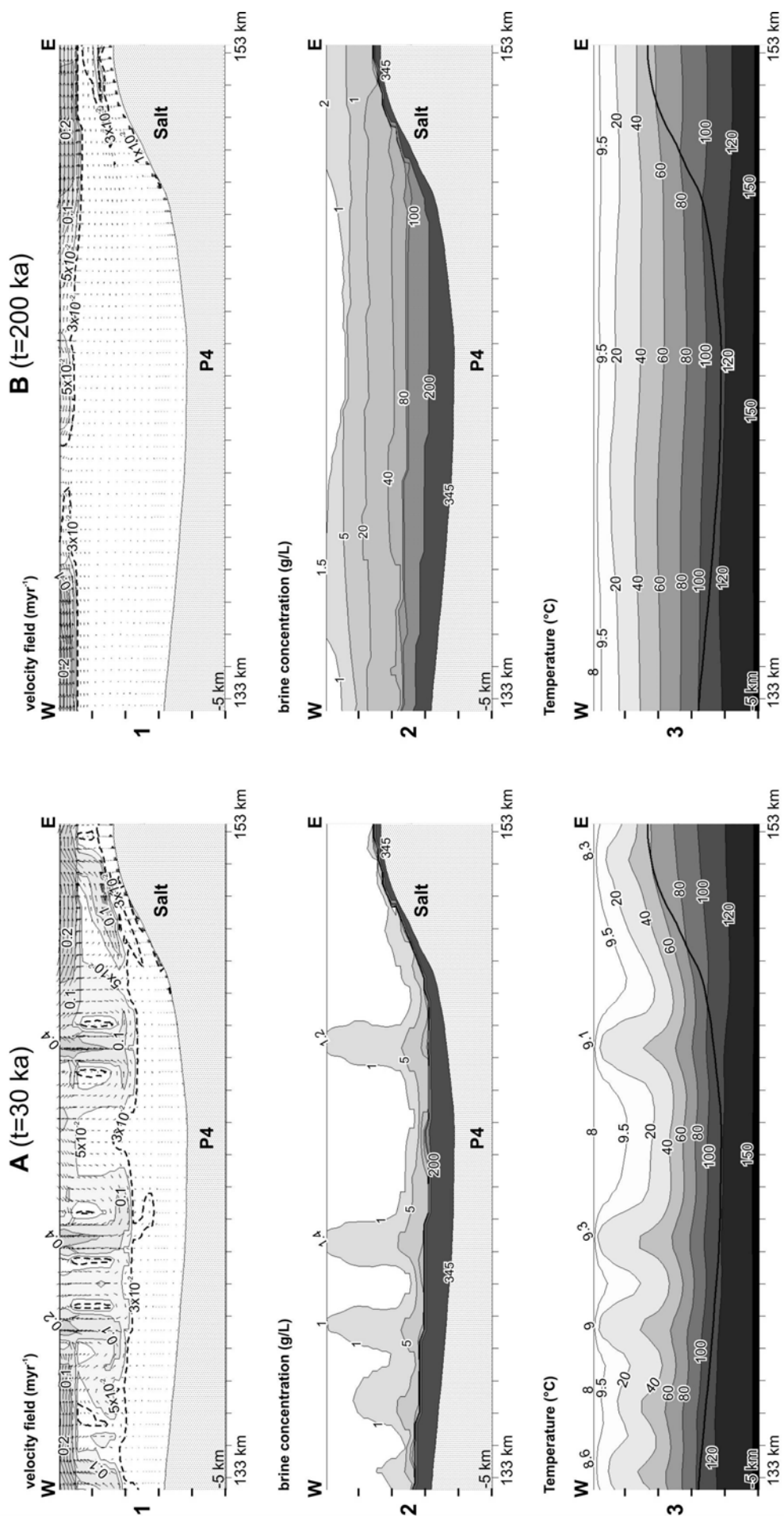


**Fig.3-20:** A and B: Zoom of the thermohaline simulation results for profile P4 as located in Fig.3.18 at  $t=30$  ka and  $t=200$  ka respectively. No vertical exaggeration is used. **1:** Pore water velocity field in myr<sup>-1</sup>. Pore vector linearly scaled to the largest flow arrow. **2:** salt concentrations in g/L. **3:** temperature distribution in °C.

By comparing Fig.3.16 A2 with Fig.3.20 A2 it turns out that at the begin of the simulation process, the viscosity does affect the spatial distribution of the brine plumes: finger patterns develop at the same locations. This feature is due to the early temperature oscillatory regime which is the same when viscosity is constant (Fig.3.16 A3) or variable (Fig.3.20 A3).

However, while in a constant viscosity regime the convective regime persists over time (Fig.3.16 B1), with a variable viscosity the convective cells disappear within P4 (Fig.3.20 B1). The velocity field displays broad stagnation areas except in the shallow aquifer where the regional flow takes place, and along the salt diapir flank where a mass Dirichlet boundary condition is set. The very low velocities are due to the high brine concentration values throughout the profile (Fig.3.20 B2). Owing to the intense brine flow rates enhanced by viscosity, as time progresses more saltier and heavier water fills the sediment. Consequently the pore velocities decrease faster. The mass profile evolves in a layered stratification in which concentration increases with depth. Freshwater conditions occur in association with the recharge area in the central part of the profile. Accordingly, the temperature field is slightly disturbed (Fig.3.20 B3).

On the other hand, the convective regime still occurs in the central part of the basin after 200 ka as shown in profile 5 (Fig.3.21). A thermally induced convective cell affects the eastern end of the section (Fig.3.21 1). In relation to the upward flow enhanced by the effects of viscosity, a vertical brine front with 1 g/L of dissolved halite develops adjacent to the west-east regional flow (Fig.3.21 2). As seen by the 0.5 g/L isopleth, a density lid forms at the top of the plume spreading laterally toward the regional flow. Consequently lateral directed brine flow is likely favored in that part of the basin. As more salt fills the sediment, the convective cell will break down and the brine plume will extend toward the center of the profile as it is the case at the western part of the section. This further suggests that the convective regime has not achieved a steady state.

## Mixed convection and fluid viscosity: Profile P5

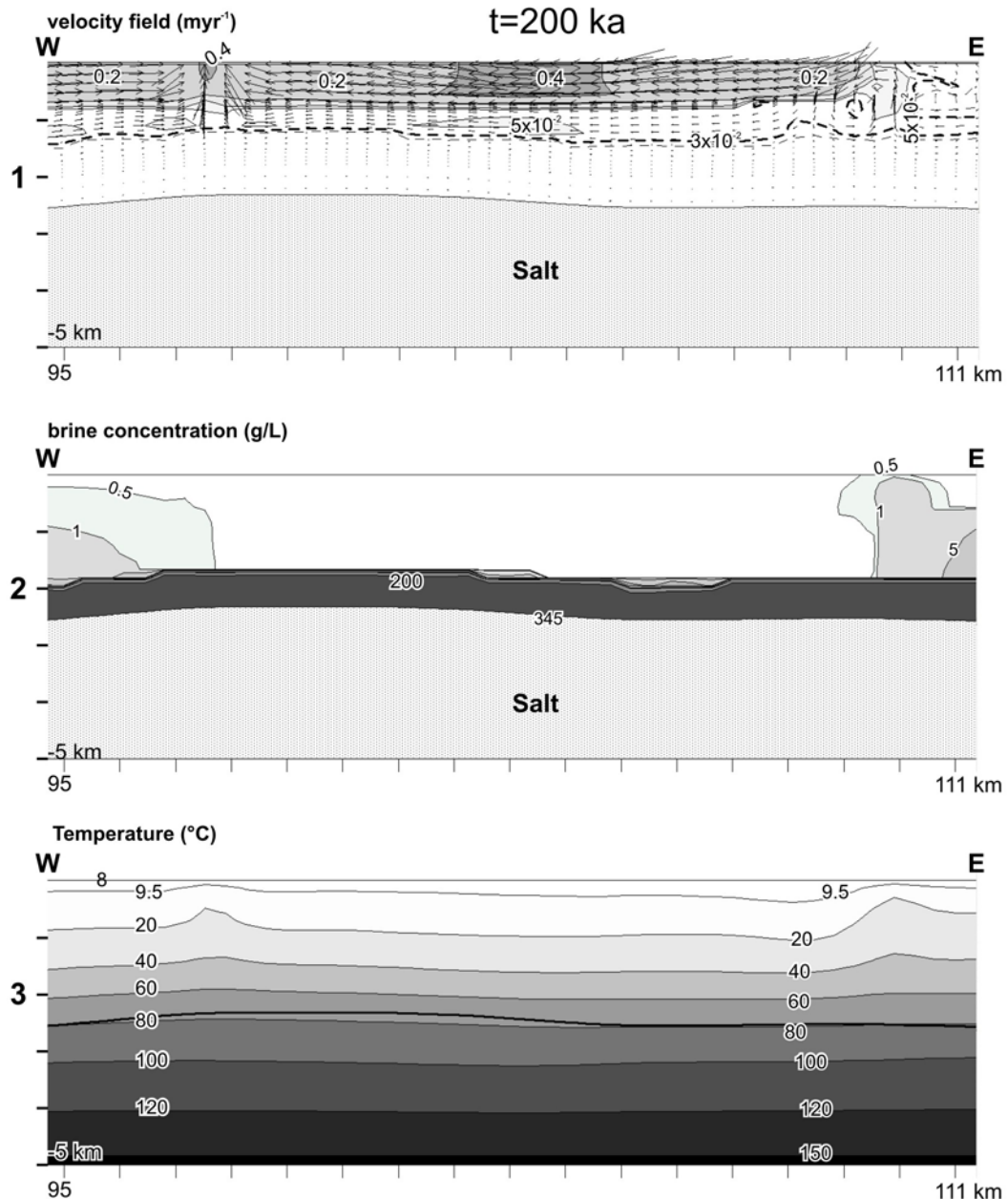


**Fig.3-21:** Zoom of the thermohaline simulation results for profile P5 as located in Fig.3-18 at  $t = 200$  ka . No vertical exaggeration is used. **1:** Pore water velocity field in  $\text{myr}^{-1}$ . Pore vector linearly scaled to the largest flow arrow. **2:** salt concentrations in g/L. **3:** temperature distribution in  $^{\circ}\text{C}$ .



### **3.3        *Discussion***

The different types of simulation have highlighted the major components involved in brine transport within the NEGB. Within the Buntsandstein the regime is purely diffusive, i.e. mass concentration increases linearly with depth. The fresh/salt water interface develops up to the Muschelkalk which shapes the brine front owing to its very low permeability. In salt diapir environments, pure diffusive brine transport is dominant. The large lateral salinity gradients supplied by the salt diapirs induce downward brine flow along the steep salt diapir flanks. The plumes are layered and extend away from the salt domes over 30 km in the lateral directions. In the free thermohaline regime, the flow is self-organized into several cells: their size is controlled by the aquifer thickness, basin geometry and permeability ratios. The thermal induced cells are more vigorous in the shallow aquifer where the layers are more permeable. In salt dome environments, the perturbed temperature field generates thermal buoyant forces stronger than the gravitational field. As a result, solute and thermal fingers develop over the same area and penetrate within the sediment fill up to the surface. The upward brine flow is also present in the sediments overlying steep salt diapirs.

The fundamental importance of temperature effects for surface brine occurrences is directly inferred by comparing the patterns for brine transport and regional flow (Fig.3-5) with those resulting from mixed convection (Fig.3-13). In the first case, the brine leaches through the surface only at the western part of the basin where shallow salt dissolution occurs in association with the strongest discharge flow rates. Throughout the rest of the basin salt upconing does not exceed half a kilometer depth. On the other hand, when the temperature effects are taken into account in the model, the brine patterns develop as salty fingers reaching the surface. The areas likely favored for surface salty water occurrences are the discharge areas (basin lowlands) in which solute and thermal plumes are advected by the regional flow and in flat areas in which the free thermohaline regime is dominant.

Furthermore the simulations have allowed to estimate the effects of viscosity on the velocity, mass, and temperature fields. Owing to the temperature dependence of the viscosity, thermally induced brine plumes flow at increased velocities. Consequently more dissolved halite is transported by the convective regime throughout the basin.

## Chapter 4. Three-dimensional thermohaline approach

Two-dimensional thermohaline simulations derived from a cross section through the NEGB provided convincing evidence for the existence of regional convective flow throughout the basin. The results have revealed that salty subsurface flow can be driven by thermally induced convection. However, it remained unclear whether the convective regime will be stable in three dimensions and to which degree the convection cells are directly related to salt structures. Moreover, a two-dimensional analysis alone is not sufficient to derive the observed solute distribution at the surface.

In this chapter, a three-dimensional analysis is attempted in order to further clarify which mechanisms underlie salt transport in the NEGB. 3D thermohaline simulations are carried out for two different scenarios. In the first part, a large scale regional model (230x330 km) indicates that salt water occurs close to the surface within the lowlands along the larger rivers. However, the coarse mesh resolution does not allow to quantify temperature effects on the mass distribution. In the second part, a smaller-scale model (10x10 km) is constructed with a grid resolution accounting for possible thermally induced convective flow. Initial and boundary conditions are those used in the two dimensional approach.

### 4.1 *Large-scale model scenario*

The study area covers 230 x 330 km in the horizontal and 5 km in the vertical direction (cf Chapter 1). The model scenario has been subdivided into a 3D finite-element mesh composed of triangular prisms. The defined grid provides an horizontal cell resolution of approximately 2.5 x 2.5 km while the vertical resolution is variable depending on the thickness of the layers. 340,000 grid points are used to discretize the balance equations of the numerical model. The mesh allows to incorporate the geological model (Scheck 1997; Scheck and Bayer 1999) into the FEFLOW database. Furthermore, the resolution ensures to keep computational time at a reasonable level in solving the bulk calculations. The choice of triangular cells has been dictated by the need for adapting the grid to the irregular shape of the natural boundary conditions imposed by the northern coast line and the basin margins. Especially at the southern margin the sedimentary fill does not exceed a total thickness of 40 m as shown schematically in Fig. 4.1. These regions correspond to eroded layers where fluid flow and mass transport play a minor role. In order to represent these no-flow zones in the numerical

model and to preserve the 3D geological structure, as well as the natural boundary conditions, very low permeability and diffusivity values (close to zero) are assigned throughout the uplifted area. Hence, in such areas, the calculated flow rates are almost equal to zero.

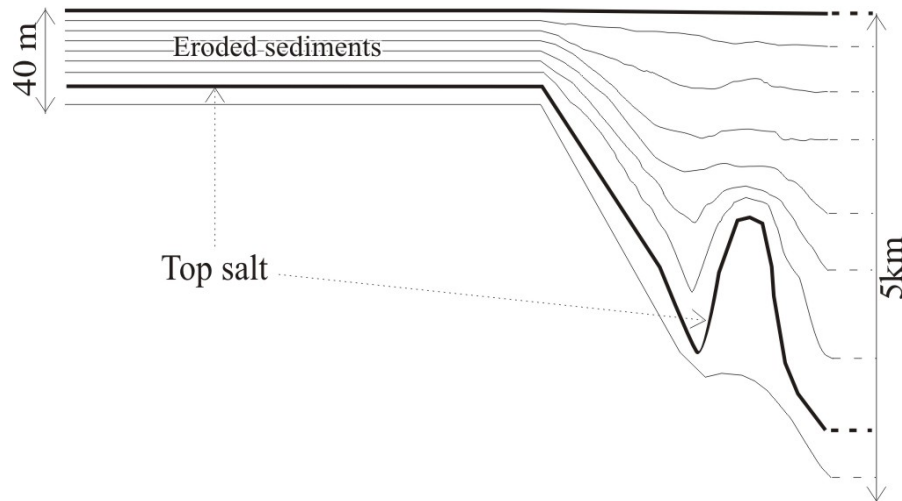


**Fig.4-1:** Sketch of the geological structure near the uplifted area.

Fig.4-2 illustrates the calculated salinity of the pore water at the surface at the end of the simulation run. The results indicate two wide areas where dissolved halite reaches the surface. A first plume extends over 100 km approximately, from the western limit of the study area to the southern basin margin while the other develops west of Berlin stretching over 140 km in the north-south direction. Few isolated and smaller patterns of salty water which reaches the surface (of the order of 10 km length) can also be observed along the Elbe river between the two main plumes and close to Berlin.

The calculated mass concentrations ranges from fresh water (0 g/l) to solute values (1.5 g/l), which are in good agreement with field measurements. The highest salt concentrations can be observed in the south-western area, near the basin margin. The concentration range provided by the numerical calculations points towards the existence of intrinsic system dynamics, such as upward saline flow.

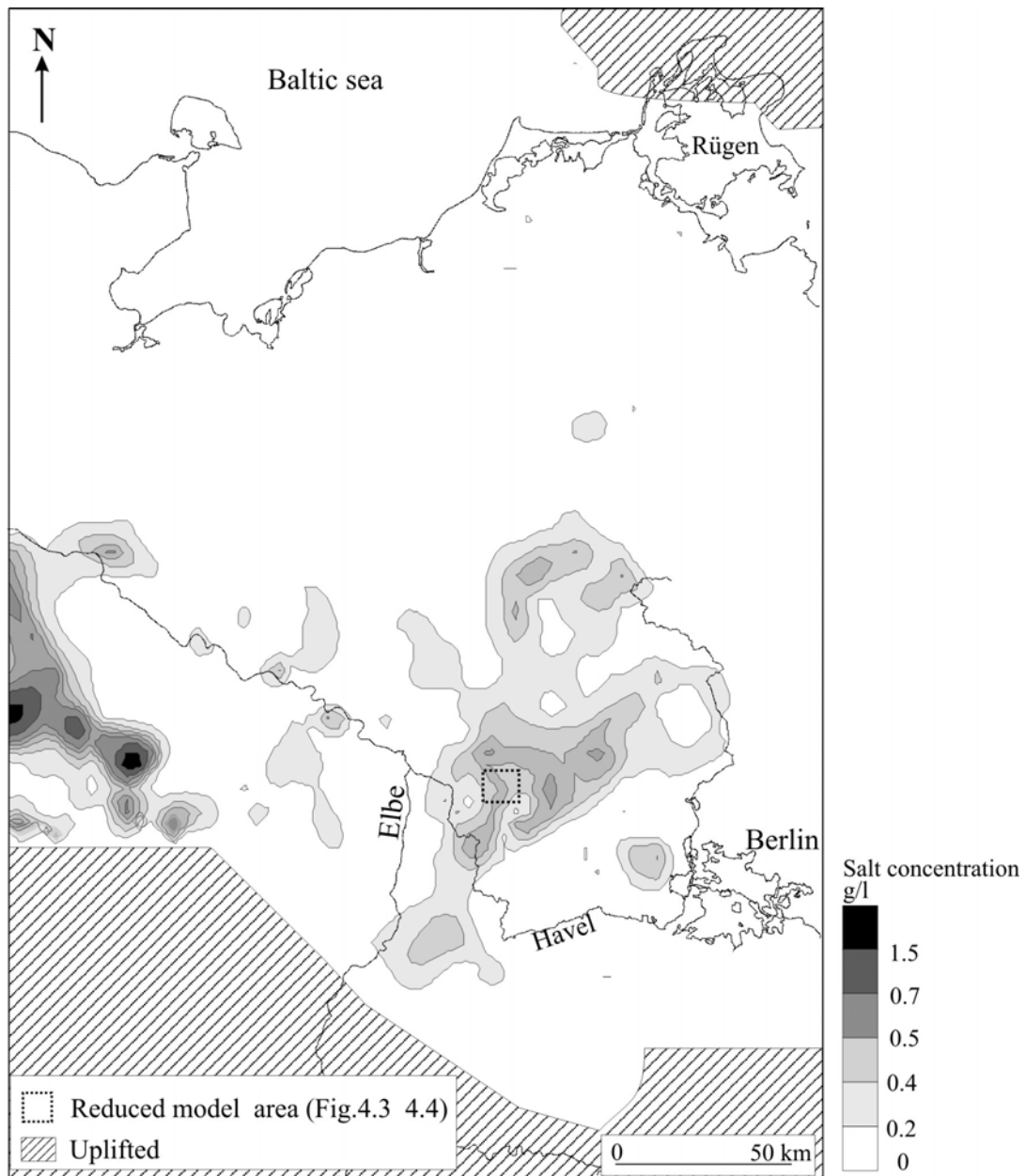


**Fig.4-2:** Large scale model scenario results. Calculated mass distribution at the surface at the end of the simulation run.

A comparison of Fig.1-1 (Chapter 1) with Fig.4-2 reveals similarities between the calculated salinity plumes at the surface (Fig.4-2) and the saline groundwater distribution as compiled by Grube et al. (2000) (Fig.1-1). In particular, in the south-western area (from the Elbe river to the basin margin) and in the central part of the basin the calculated brine patterns (Fig.4-2) are in agreement with the observed data (Fig.1-1). The data compiled by Grube et al. (2000) account for groundwater salinity profiles from the surface to a depth of 300 m whereas the numerical model provides solute distribution at the surface. Therefore the areas of Fig.4-2 which do not compare favourably with the data map (Fig.1-1) likely correspond to the occurrence of brines at deeper levels. Observations as well as modelling results indicate that

hydrostatic flow probably provides the dominant mechanism in the lowlands along the Elbe river.

Simulations of coupled fluid flow and solute transport, provides similar surface brine patterns obtained from the thermohaline simulations. The reason is that the selected grid resolution is not fine enough to account for thermohaline effects. In order to quantify temperature effects on the calculated solutal gradients, a higher cell resolution is required. Further mesh refinements have revealed a dramatical increase in computational time for the bulk calculations of the numerical balance equations. Therefore within the given modelling framework, a higher density of active nodes discretizing the large scale model cannot be realised together with long time simulations. Consequently, it is necessary to reduce the area of the study model in order to define a highly refined grid adapted to thermohaline convective flow.

## 4.2 *Square box model scenario*

The location of the detailed model is indicated in Fig.4-2. The area covers a square box of 10 km length. The location has been chosen because it is situated within one of the identified surface brine plumes, as shown in Fig.4-2. Fig.4-3 illustrates the topography of the study area without significant topographical variation. Consequently, hydrostatically driven flow should not be the primary force. Moreover, in this site, no diapir is present. Therefore, sub-surface brine occurrences are not related to strong lateral salinity gradients supplied by salt diapirs.

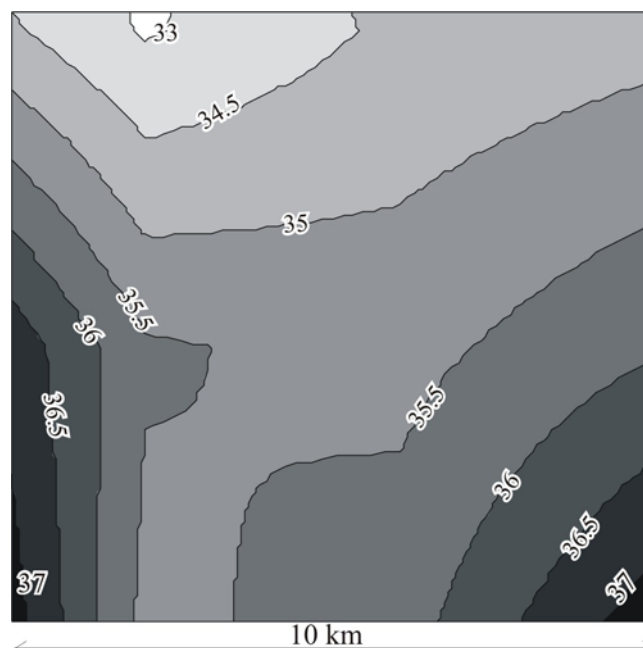


**Fig.4-3:** Topography (m) of the reduced model scenario

The domain has been subdivided into a rectangular mesh containing 34 x 34 grid points, resulting in a cell resolution of 290 m.

In order to provide an evolution analysis, the simulation results will be illustrated for two time steps. Solutions of the coupled balance equations will be shown at a computing time of 30 ka and at the end of the simulation run (200 ka).

Fig.4-4 shows the calculated solute (g/L) and temperature (°C) distribution at the surface of the model area at  $t = 30$  ka (A) and at the end of the simulation run (B). Solute and thermal plumes occur at the surface occupying identical regions. As time progresses, the plumes persist, however, they stretch over a longer distance. Particularly, higher salt concentrations correlate with increased surface temperature.

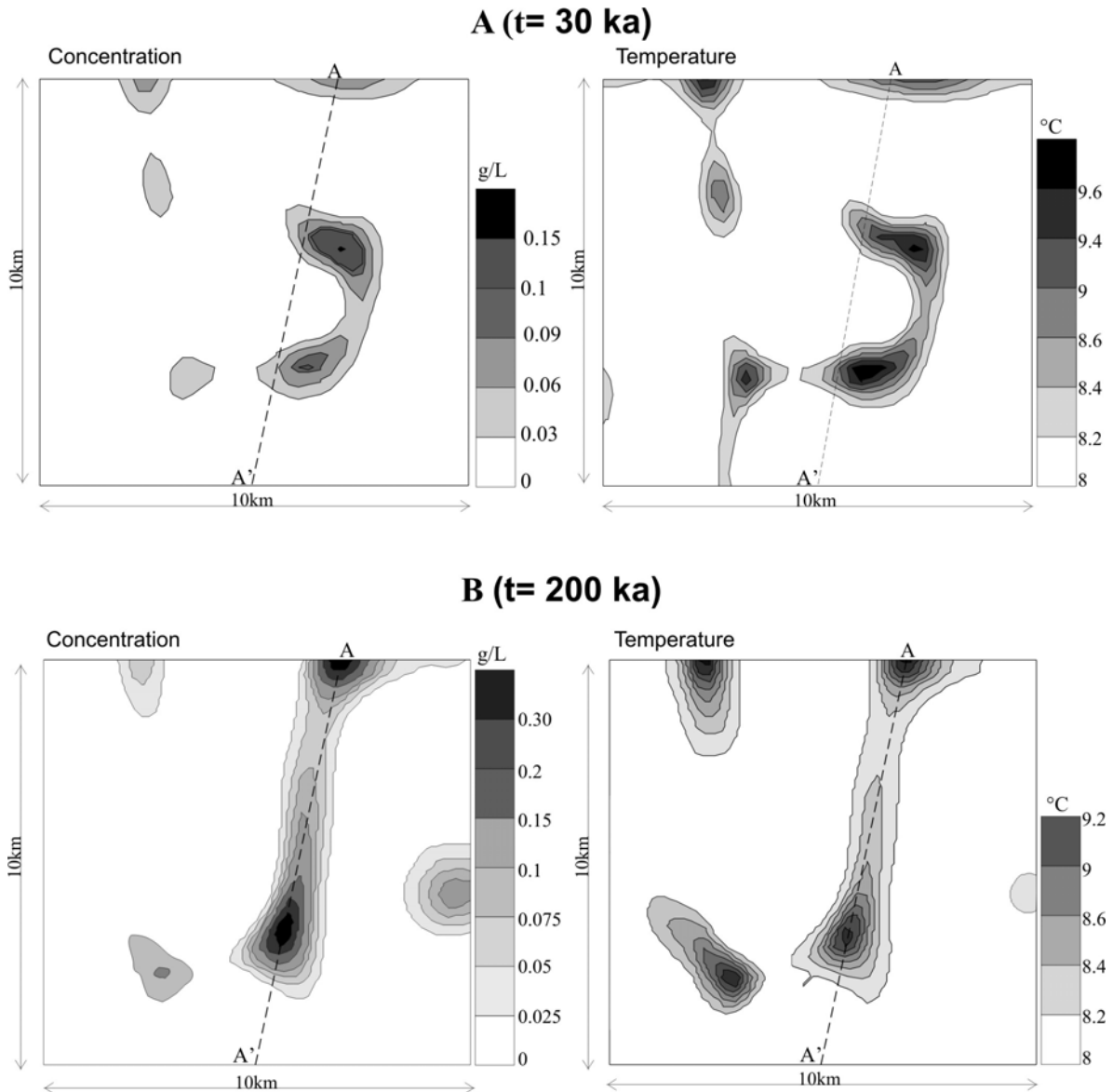


**Fig.4-4:** Reduced model scenario results. **A:** Calculated patterns at the surface at  $t = 30$  ka and **B** at  $t = 200$  ka respectively. Left: salt distribution (g/L). Right: temperature (°C) distribution at the surface. Dotted lines indicate the location of the selected cross-section A-A'.

These simulations highlight two significant aspects of the flow regime:

- If the temperature input is removed from the numerical calculations, no saline water reaches the surface.
- The peak concentration calculated at the end of the simulation run is two times higher than the concentration observed at the onset of the process. The temperatures approximately span the same range.

These two features of the system can be explained as follows. Without temperature input no solute plumes develop, therefore it can be inferred that thermal effects on fluid density generate buoyant forces strong enough to overcome the gravity field that keeps heavy brine close to the salt layer. Consequently, as time progresses, the brine undergoes a continuous salt replenishment from below by upward solute transport induced by the temperature gradient. This process leads to higher concentrations at the surface at the end of the simulation run. In summary, these results indicate that the deep-seated brine can locally reach the surface driven by induced free thermohaline convective flows even in absence of steep salt diapirs. However, the salt concentration values at the surface are inferior to those calculated from the 2D simulations.

In order to emphasize the mechanisms driving solute up to the surface, the calculated concentration, temperature and velocity field are extracted at each computing time step along a cross-section (denoted by A-A' in Fig.4-4). The section of approximately 9,5 km length slices the main brine and temperature pattern obtained at the surface at the end of the 3D simulation run (Fig.4-4 B). In Fig.4-5 the geological structure along A-A' as well as the finite element mesh are shown.

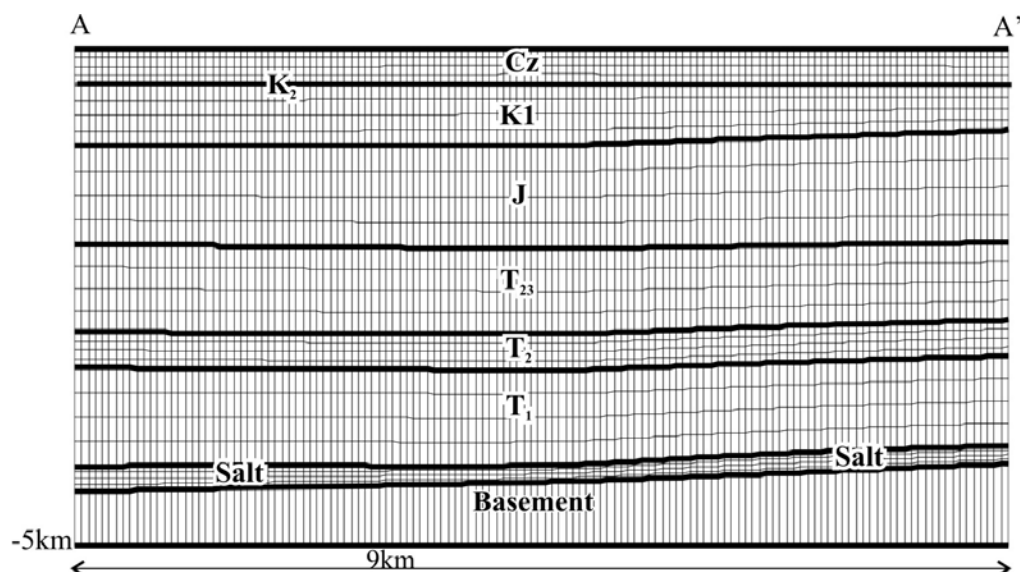


**Fig.4-5: A)** Geological structure (abbreviations given in Table.1) and finite element mesh of the selected cross-section as shown in Fig.4-4.

Fig. 4.6 1, 2, 3 illustrate the calculated velocity ( $\text{m/yr}^{-1}$ ), mass ( $\text{g/L}$ ), and temperature ( $^{\circ}\text{C}$ ) distribution at a computing time of 30 ka (A) and at the end of the simulation run (B).

Fig.4-6. A1 shows the calculated pore velocities of the convective cells at  $t = 30$  ka. Vectors indicate the flow directions. The velocity values range from 37 cm per year in the shallow aquifer to few millimeters per year in the deeper stratigraphic units. The vigour of convective flow decreases of ten orders with increasing depth. This strong velocity contrast is due to the vertical heterogeneity of the layers within the system. Indeed, the shallow aquifer consists of layers which have the highest permeabilities (Table.1). This velocity feature is also confirmed by Rosenberg and Spera (1990) who investigated the role of layered permeability heterogeneity in hydrothermal convection.

The flow dynamics, thereby, separates into two subsystems (Fig.4-6 A2):

- 1: Above the Muschelkalk (located at 3 km of depth), the upward flow is associated with convective transport of dissolved salt which is manifested as salinity plumes protruding throughout the sediments up to the surface. Brine plumes develop as three separated streams forming two well-defined vertically stacked convective cells. The flow field characteristics, described here, are in agreement with those derived from theoretical considerations by Rosenberg and Spera (1992). In that study, the authors summarized the various types of dynamics occurring in thermohaline convection in a porous medium heated from below for different sets of initial conditions and buoyancy ratios. The model scenario presented here corresponds to what they define a “salted from below” boundary condition and “layered box” initial condition system at high buoyancy ratio. For this particular configuration, Rosenberg and Spera found that at early computing time the flow field consists of vertically stacked convection cells. Here, the plumes crests are spaced at about 3 km in the horizontal direction.
- 2: Below the Muschelkalk (within the Buntsandstein) the mass transfer is dominated by diffusion. Accordingly, the solute concentration field is not disturbed presenting almost flat isopleths. The interface fresh water/brine is approximately located at 3 km below the surface within the Muschelkalk.

Fig.4-6 A3 shows the same system dynamic in terms of heat transfer: above the Muschelkalk the heat transfer is characterized by protruding plumes reaching the surface locally while at deeper levels heat transfer is dominated by conduction.

By comparing Fig.4-6 A2 with Fig.4-6 A3, it results that the “density lid” described in the 2D thermohaline simulations is preserved even in 3D: heat and brine plumes rise together to approximately the same height.



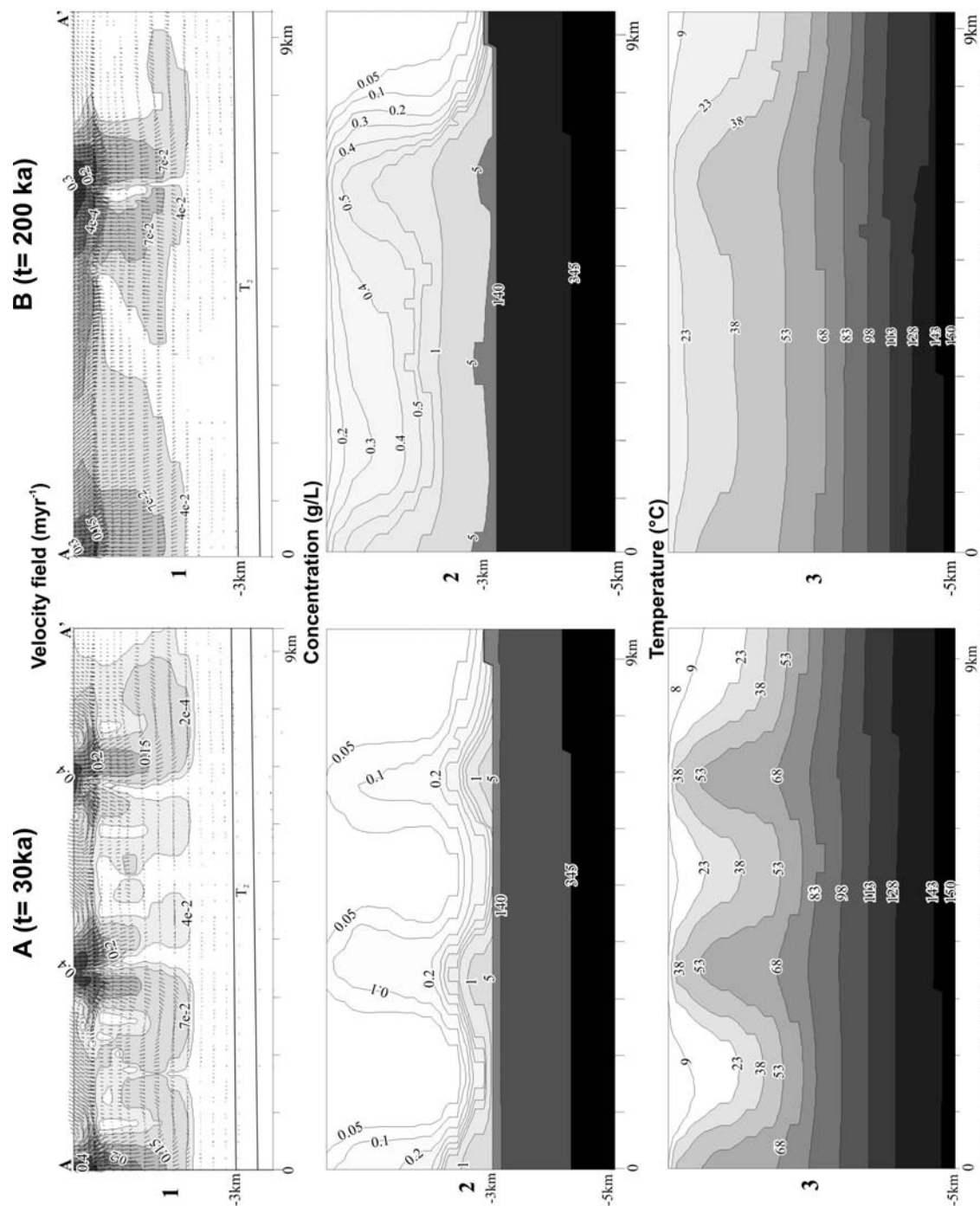


Fig.4-6: 1) velocity field along A-A' ( $\text{myr}^{-1}$ ) 2) Profile of salt distribution (g/L), 3) and temperature ( $^{\circ}\text{C}$ ) resulting from 3D thermohaline simulations at  $t = 30$  ka.(A) and at  $t = 200$  ka

A comparison of Fig.4-6 A1 with 4.6 A2 and with Fig.4-6 A3 emphasizes the strong relation between the vigour of upward convective flows and the areas where thermal and solute plumes protrude. Salty water locally reaches the surface where the highest values of temperature and flow velocity are observed.

At the end of the simulation run (Fig.4-6 B), the system approaches a steady-state which is favored by the lateral boundary conditions. This feature is once more confirmed by Rosenberg and Spera (1992); the authors predicted that, for this type of model scenario, the vertical stacked cells observed at early simulation time eventually evolve to a steady-state. Although the pattern simplifies, the flow regimes still persist. The final flow velocities show still higher values in the shallow aquifer, and peak velocity values are observed in those locations of the study area where solute and thermal plumes reach the surface. The convection pattern is still penetrative but presents only one and a half weak cell. Above the Muschelkalk concentration and temperature gradients are disturbed by the convective regime while below this stratigraphic unit solute and heat transfer are conductive.

Comparison of Fig.4-6 B2 with Fig.4-6 B3 shows that the feature of the density lid is still preserved: the highest solute concentrations are at the top of the convection cell at the same height of the heat plumes. From these pictures, it can also be noticed that the density lid promotes lateral flow of the plumes toward A'.

By comparing Fig.4-6 A with Fig.4-6 B, the velocities have slightly decreased as more solute is advected in the shallow aquifer by the upward convective flows. Some of the weaker convective cells are swallowed up by stronger neighbouring cells. Ranganathan and Hanor (1988) found the same behavior for pore velocities near salt domes. At the end of the simulation run high concentration isopleths come closer to the surface than in earlier phases of the process. Consequently, the sediments above the Muschelkalk are almost all filled with brine and higher concentration values can be observed locally at the basin surface.

In summary, the highly refined grid defined for the reduced model scenario allows to account for thermohaline effects. Simulation results prove that temperature effects on fluid density provide buoyancy forces strong enough to generate upward flows driving dissolved halite to the surface even in absence of steep salt diapirs.

Cross-sections of the calculated 3D pattern provide additional insight into the dynamic of the resulting thermally induced flows. Specifically, two major features are found to persist: above the Muschelkalk the vigour of flow is higher and is manifested by convective cells developing within the sediment fill. On the other hand, below this layer, the system regime is purely conductive. Furthermore, 3D thermohaline simulations emphasize the strong link

between concentration and temperature distribution. In both horizontal and vertical direction, thermal and solute plumes always correlate in space and time.

Evolution analysis of the calculated profiles show that, supported by the close boundaries, dissolved solute continues to fill the shallow aquifer from below as time progresses. Consequently, the increasing concentrations weaken the convective cells. Nevertheless, even in the presence of high dissolution rates, the disturbed temperature gradient generates velocity fields able to drive solute locally up to the surface.

### **4.3 Discussion**

3D numerical simulations of coupled fluid flow, heat and salt transport correlate with the observed data. The large model scenario indicates that regional flow is one mechanism driving solute within the basin. Wide stretched salty plumes spread at the surface even without temperature input. The highly refined model scenario additionally accounts for thermohaline effects on the system dynamics. It was found that the patterns are stable even in three dimensions and that the flow regime strongly depends on the basin lithology. Above the Muschelkalk, plumes of dissolved salt protrude throughout the sediments fill and reach the surface locally, whereas conductive heat and solute transport dominates the deeper part of the basin. The reduced model scenario emphasizes that even without salt diapirs the temperature gradient can be disturbed. Consequently upward solute transport is also possible above flat salt structures due to the resulting thermally induced flow. However, the salt concentration values at the surface are inferior of those calculated from 2D modeling in which salt diapirs are included.

Therefore hydrostatically driven fluid flow and thermohaline convection can be considered among the major mechanisms currently affecting parts of the NEGB, probably even supplying the observed saline springs. The modeling results already provide strong indication that regional flow and temperature-driven convective flow play an important role in driving solute within the area under consideration.

## Chapter 5. Summary and discussion

### Summary

This study originated in the assumption that thermally induced flow could lead to the saline springs observed in the NEGB. Data analysis performed by Christoph Jahnke (BTU, Cottbus) and Maja Tesmer (FU, Berlin) provided a regional picture of water chemistry in the NEGB. The basin is characterized by an inhomogeneous distribution of salt content within the pore water. Furthermore, there is strong evidence for density inversion at greater depth caused by increasing temperature. The density inversion occurs even when the fluids are saturated with salt. Chemical analyses, such as isotope contents and REY patterns emphasized the importance of head-driven flow in the shallow aquifer and the existence of upward inter-aquifer flow at depth below 1500 m. Therefore, mixed convection is likely the favoured fluid-dynamic of the NEGB.

For the first time in the NEGB, the mechanisms driving brine within the basin have been investigated by numerically modelling thermohaline flow. FEFLOW<sup>®</sup> 5 has been used for solving the transient thermohaline problem. The simulations results yielded important insights with regard to coupled hydraulic, thermal, and mass transport processes.

Owing to the complicated basin geometry and to the numerical instabilities characterizing density-driven flow, the first approach was two-dimensional. A model scenario has been built along a representative cross-section of the basin. By running preliminary simulations, the model allowed to define a robust finite element mesh and to evaluate an adequate grid resolution accounting for temperature effects. It turned out that 364 meter is the minimum grid resolution in the **x** direction required for preventing over-dissipative numerical approximation and for ensuring mesh convergence.

Based on this highly refined finite element grid, different kinds of simulations were run in order to study the various components possibly involved in brine transport within the NEGB.

Diffusive brine transport simulations, in which the flow is driven by concentration gradients, showed that the Buntsandstein unit is saturated with highly concentrated brine. Therein a steady-state concentration profile developed at early time stage. On the other hand, steep salt structures supplied a continuous halite replenishment. In the salt dome environment, halite continued diffusing and salty water fills the surrounding sediments in the lateral direction. Downward motion of dissolved halite, due to the gravity, is found to be dominant

along salt flanks. The resulting drag forces generated localized convective cells in the overlying sediments providing the main recharge of fresh water. As heavier salt-laden water is produced, velocities decrease and the convective cells weaken or disappear. Brackish water with 1 g/L of dissolved salt occurs at depths between half and 1 km in the surrounding of shallow salt structures.

Subsequently, the regional flow has been taken into account in order to quantify the advective flow effects on the brine patterns. The mass profile is strongly influenced by head-driven flow even at low velocities. Upward or downward migration of dissolved halite is respectively found in relation to ascending or descending fluid circulation due to the regional flow. It was found that discharge areas occurring above shallow salt structures can lead to surface occurrences of salty water.

The effects of temperature anomalies have been evaluated by simulating free thermohaline convection. The calculated patterns showed features of a thermohaline and a static regime: narrow brine fingers penetrated in the sediments above the Buntsandstein unit and the thermal anomalies manifested as non-periodic waves which intensity decreases with depth. While in the diffusive regime the brine patterns are embedded within the stratigraphic units, thermal buoyant forces led to vertical plumes advecting salty water up to the surface. Flow velocities are increased of 1 order of magnitude in direct relation to the thermally induced convective cells. Furthermore, the increased temperature gradient in the vicinity of salt domes generated upward flow of brine even along the edge of steep salt diapirs. A general aspect of the thermohaline regime is the strong coupling of heat and mass transport which is manifested by salty and thermal plumes rising together.

The effects of regional flow have also been evaluated in combination with the free thermohaline regime. The major features of free convective flow are preserved. However, both salty and thermal fingers evolved into a smaller but larger number of plumes which are shaped by the regional flow. On the other hand, in the areas of the basin where the regional flow rates are smaller than the thermally induced velocities, brine and thermal fingers self-developed as in a free thermohaline regime.

In the mixed convection regime fluid viscosity effects have been quantified. Fluid viscosity increases the permeability of the layer in direct relation to increased temperature gradient. Therefore the thermally induced brine plumes formed faster and higher flow rates. As a result, mixing processes are enhanced leading to weakened convective cells and enlarged brine patterns. By contrast, the convective regime remains dominant in areas of the basin where pore water is close to fresh water conditions.

The experience gained with the 2D modeling approach has been applied to tackle the 3D thermohaline problem. A large scale regional model covering the whole study area (230x330 km) indicates that salt water occurs close to the surface within the discharge areas in the lowlands. However the coarse mesh resolution does not allow to quantify temperature effects on the mass distribution. Therefore a smaller scale model (10x10 km) has been constructed with a grid resolution accounting for possible thermally induced convective flow. It has been found that the convective regime described in the 2D models occurred even above flat salt structures.

## **Discussion**

The model simulated in this study represents simplified conditions of the NEGB. The model is not trying to reproduce reality in details but is meant to delineate the physical causes and forces that contribute to surface brine occurrence. However, to gain additional insights with regard to the long-term behaviour of this geothermal system, more complex models have to be set up. Accordingly, several items should be tested:

- Sensitivity analysis concerning initial conditions: the mass initial conditions used is layered: the initial concentration starts from freshwater condition above the Top Zechstein Salt while a saturation value has been set on the top of the salt. Furthermore, initial pressure and temperature conditions were obtained from steady-state simulations. Now that a robust model has been built up, it would be of great interest to test whether different sets of initial condition can be defined based on the available dataset.
- In addition, different model parameters should also be checked. The convection cells have wavelengths and flow patterns depending on permeabilities as well as on mass, thermal and hydraulic boundary conditions. Clausnitzer et al. (2001) investigated the impact of permeability on temperature oscillations. At the lowest permeability level, free convection vanishes and groundwater stratification is stable. The regional spotty occurrence of the vagabonding springs, therefore, could be due to minor changes in average permeability within a few stratigraphic horizons. However those simulations did not account for density variations due to the salt content and therefore should be re-evaluated with the present model.

Concerning the boundary conditions at the surface, the hydraulic head is assumed to be a subdued replica of the topography. This condition induces a steady state regional flow in which recharge and discharge areas do not evolve in time. However, on such a large time-scale, the role of changing climatic condition on water tables should be accounted for.

Heat and mass boundary conditions at the surface are of Cauchy type. The transfer coefficients which govern these natural boundary conditions were evaluated by rough approximations. Testing different values of these parameters is needed in order to obtain a better reproduction of the observed data. Due to the constant salt concentration at the Salt surface, brine is continuously replenishment supplied. However, in salt dome environment the boundary concentration is strongly dependent on the dynamic processes. Therefore, a Cauchy boundary condition should be as well considered and tested in further studies.

- Simulation time: the model is working with an artificial time scale set up to 200 ka. However the simulations show that a steady state is approached but not reached. Brine fronts are still unstable at the end of the simulation process and therefore fluid-dynamics is subjected to further temporal evolution. Long term simulations can provide more details on the development of these brine fronts.
- Interaction with faults: in the present study, faults were neglected. In reality, the NEGB system contains many faults which can strongly affect the shape and the spatial distribution of the convective cells. These interactions should be investigated in order to quantify their impact on the flow regime. Numerical models of thermal convection in faulted extensional sedimentary basins have been recently carried out by Simms and Garven (2004). Steeply dipping extensional faults can provide pathways for vertical fluid flow across large thick sediments and can modify the dynamics of thermal convection. The presence of faults perturbs the thermal convective flow pattern and can constrain the size and locations of convection cells. Depending on the spacing of the faults and the hydraulic properties of the faults and basin sediments, the convection cells can be spatially organized to align with adjacent faults.
- Paleo-history: it can be expected that the salinity distribution at shallow depth can reflect, to some extent, paleological and hydrodynamic conditions since Zechstein times. These paleo-conditions include: changes in the groundwater level and in the surface temperature as well as interrelationships between the aquifer and the seal-level of the North and Baltic sea during the younger geological history.

While all these effects need to be studied, the numerical results already correlate with the predictions from geochemical analysis, indicating that mixed convection is among the major factors currently affecting parts of the North German Basin, perhaps even causing salt brines to reach the surface in certain areas.

## REFERENCES

- Bayer, U., Clausnitzer, V. and Fuhrmann, J., 2002. Unsteady thermal convection in the North East German basin. Technical report, WIAS Berlin, 741.
- Bear, J., 1988. Dynamics of Fluids in Porous Media. Dover, New York, 764 pp.
- Bear, J., 1991. Modelling transport phenomena in porous media. Convective Heat and Mass Transfer in Porous Media: 7-69.
- Bear, J. and Bachmat, Y., 1990. Introduction to Modeling Transport Phenomena in Porous Media. Kluwer Acad. Publ., New York, 764 pp.
- Bernhard S., 1997. Thermodynamic and Transport Properties of Water and Steam.  
<http://www.cheresources.com/iapwsif97.shtml>.
- Bird, R.B., Stewart, W.E. and Lightfoot, E.N., 1958. Notes on transport phenomena, New York, 455 pp.
- Bjorlykke, K., Mo, A. and Palm, E., 1988. Modelling of thermal convection in sedimentary basins and its relevance to diagenetic reactions. Marine and Petroleum Geology, 5(4): 338-351.
- Bodenlos, A.J., 1970. Cap rock development and salt rock movement. The Geology and Technology of Gulf Coast Salt, Symposium Proceedings. Louisiana State University, Baton Rouge, 192 pp.
- Chen, W., Ghaith, A., Park, A. and Ortoleva, P., 1990. Diagenesis through coupled processes: Modeling approach, self-organization, and implications for exploration. In Prediction of reservoir quality through chemical modeling, AAPG Memoir 49, edited by Indu D. Meshri and Peter J. Ortoleva. Tulsa, OK: AAPG.: 103-130.
- Cheng, P., 1978. Heat transfer in geothermal systems. Advances in Heat Transfer, 14: 1-105.
- Clausnitzer, V., Bayer, U. and Fuhrmann, J., 2001. Large-scale thermal convective instability in sedimentary basins. Eur. Geophys. Soc., Geophys. Res. Abstracts HS02-02.
- Cooper, C.A., Glass, R.J. and Tyler, S.W., 1997. Experimental investigation of the stability boundary for double- diffusive finger convection in a Hele-Shaw cell. Water Resources Research, 33(4): 517-526.
- Dagan, G., 1989. Flow and Transport in Porous Formations. Springer-Verlag, New York Academy of Sciences Transactions, 465pp
- Diersch, H.-J.G., 2002. FEFLOW finite-element subsurface flow and transport simulation system. User's Manual/Reference Manual/White Papers, Release 5.0. WASY GmbH, Berlin.



- Diersch, H.J.G. and Kolditz, O., 1998. Coupled groundwater flow and transport: 2. Thermohaline and 3D convection systems. *Advances in Water Resources*, 21(5): 401-425.
- Diersch, H.J.G. and Kolditz, O., 2002. Variable-density flow and transport in porous media: Approaches and challenges. *Advances in Water Resources*, 25(8-12): 899-944.
- DIN, 1986. Summarische Wirkungs- und Stoffkenngrößen (Gruppe H)-Bestimmung der Säure- und Basekapazität (H7). D. deutsches Institut für Normung e.V.: 1-10.
- DVWK, 1992. Entnahme und Untersuchungsumfang von Grundwasserproben. Paul Parey, Hamburg. 128:33.
- Ekman, V.W., 1906. Beiträge zur Theorie der Meeresströmungen. *Ann. d. Hydrogr.*: 34-50.
- Evans, D.G. and Nunn, J.A., 1989. Free thermohaline convection in sediments surrounding a salt column. *Journal of Geophysical Research*, 94(B9): 12,413-12,422.
- Evans, D.G., Nunn, J.A. and Hanor, J.S., 1991. Mechanisms driving groundwater flow near salt domes. *Geophysical Research Letters*, 18(5): 927-930.
- Evans, G.E., Nunn, J. A., 1989. Free thermohaline convection in sediments surrounding a salt column. *J. Geophys. Res.*, 94: 12413-12422.
- Feyerabend, T., Kuhlmann, K. and Bening, L., 2000. Grundwasserversalzung in der Norddeutschen Tiefebene.
- Flocks, J.G., Kindinger, J.L., Davis, J.B. and Swarzenski, P., 2001. Geophysical Investigations of Upward Migrating Saline Water from the Lower to Upper Floridan Aquifer, Central Indian River Region, Florida. *Water-Resources Investigations, Report 01-4011*: 135-140.
- Garven, G., Bull, S.W. and Large, R.R., 2001. Hydrothermal fluid flow models of stratiform ore genesis in the McArthur Basin, Northern Territory, Australia. *Geofluids*, 1(4): 289-311.
- Georgiadis, J.G., 1991. Future research needs in convective heat and mass transport in porous media. *Convective Heat and Mass Transfer in Porous Media*: 1073-1088.
- Glander, H. and Schirrmeister, L., 1975. Erfassung und Darstellung der oberen Mineralwassergrenze. *Zeitschrift für angewandte Geologie Teil 1*, 21,(7).
- Gresho, P.M. and Sani, R.L., 2000. Incompressible Flow and the Finite Element Method, Volume 1, Advection-Diffusion and Isothermal Laminar Flow. John Wiley & Sons, 480 pp.
- Grube, A., Wichman, K., Hahn, J. and Nachtigall, K., 2000. Geogene Grundwasserversalzung in den Porengrundwasserleitern Norddeutschlands und ihre Bedeutung für die Wasserwirtschaft, 9. Technologiezentrum Wasser Karlsruhe (TZW), Karlsruhe, 203 pp.

- Hanano, M., 1998. A simple model of a two-layered high-temperature, liquid-dominated geothermal reservoir as a part of a large-scale hydrothermal convection system. *Transport in Porous Media*, 33: 3-27.
- Hannemann, M. and Schirrmeister, W., 1998. Paläohydrogeologische Grundlagen der Entwicklung der Süß-/Salzwassergrenze und der Salzwasseraustritte in Brandenburg. *Brandenburgische Geowissenschaftliche Beiträge*, 5: 61-72.
- Hanor, J.S., 1987. Kilometre-scale thermohaline overturn of pore waters in the Louisiana Gulf Coast. *Nature*, 327: 501-503.
- Hassanizadeh, M. and Gray, W.G., 1979a. General conservation equations for multiphase systems: 1. Averaging procedure. *Advances in Water Resources*, 2(3): 131-144.
- Hassanizadeh, M. and Gray, W.G., 1979b. General conservation equations for multiphase systems: 2. Mass, momenta, energy and entropy equations. *Advances in Water Resources*, 2: 191-203.
- Hassanizadeh, M. and Gray, W.G., 1980. General conservation equations for multiphase systems: 3. Constitutive theory for porous media flow. *Advances in Water Resources*, 3(1): 25-40.
- Hassanizadeh, S.M., 1986. Derivation of basic equations of mass transport in porous media, Part1. Macroscopic balance laws. *Advances in Water Resources*, 9: 196-222.
- Hassanizadeh, S.M., 1986. Derivation of basic equations of mass transport in porous media, Part2. Generalized darcy's and Fick's laws. *Advances in Water Resources*, 9: 207-222.
- Hassanizadeh, S.M. and Leijnse, T., 1988. On the modeling of brine transport in porous media. *Water Resources Research*, 24(3): 321-330.
- Heck, H.-L., 1932. Das Grundwasser in Zusammenhang mit dem geologischen Bau Schleswig-Holsteins. *Preußische Geol. Landesanstalt*: 106-133.
- Herbert, A.W., Jackson, C.P. and Lever, D.A., 1988. Coupled groundwater flow and solute transport with fluid density strongly dependent upon concentration. *Water Resources Research*, 24(10): 1781-1795.
- Horton, C.W. and Rogers, F.T., 1945. Convective currents in a porous medium. *J. Appl. Phys.*, 16: 367-370.
- Hoth, P., Seibt, A., Kellner, T. and Huenges, E., 1997. Geowissenschaftliche Bewertungsgrundlagen zur Nutzung hydrogeothermaler Ressourcen in Norddeutschland, Scientific technical report, Potsdam, 149.
- Hurtig, E., 1994. Land Brandenburg. Bohrungen mit kontinuierlichen Bohrlochmessungen. Bohrungen mit Maximaltemperaturen. Unveröff. Unterlagen bereitgestellt durch das Landesamt für Geowissenschaften und Rohstoffe Brandenburg.
- Jevons, W.S., 1857. On the cirrous form of cloud. *London, Edinburgh and Dublin Philosophical Magazine and Journal of Science*, 4th Series, 14: 22-35.

- Johannsen, A., 1980. Hydrogeologie von Schleswig Holstein. *Geologische Jahrbuch*, 28: 451.
- Kohout, F.A., 1965. A hypothesis concerning cyclic flow of salt water related to geothermal heating in the Floridian aquifer. *New York Academy of Sciences Transactions*, ser. 2, v.28, no. 2: 249-271.
- Kolditz, O., Ratke, R., Diersch, H.J.G. and Zielke, W., 1998. Coupled groundwater flow and transport: 1. Verification of variable density flow and transport models. *Advances in Water Resources*, 21(1): 27-46.
- Kubitschek, J.-P. and Weidman, P., 2003. Stability of a fluid-saturated porous medium heated from below by forced convection. *International Journal of Heat and Mass Transfer*, 46: 3697-3705.
- Kühn, 1997. Geochemische Folgereaktionen bei der hydrothermalen Energiegewinnung, Diss.Universität Bremen, 129 pp.
- Lehmann, H.-W., 1974. Geochemie der Tiefenwässer der Nordostdeutschen Senke. *Zeitschrift für Angewandte Geologie Teil 2*, 20: 502-509.
- Lehmann, H.-W., 1974. Geochemie der Tiefenwässer der Nordostdeutschen Senke. *Zeitschrift für Angewandte Geologie Teil 2*, 20: 551-557.
- Lever, D.A. and Jackson, C.P., 1985. On the equations for the flow of concentrated salt solution through a porous medium. U.K. DOE Report No. DOE/RW/85.100.
- Löhnert, E., Bauhus, W. and Sonntag, C., 1986. Mechanism of groundwater salinization in the Hamburg region, F.R. Germany -facies and new findings. In: Boekelman R.H., Van Dam, J. Evertman, M. & Ten Hoorn, W. (HRSG.): *Proceedings of the salt water intrusion meeting*. Delft, Netherlands: 613-628.
- MacNeal, R.H., 1990. The shape sensitivity of isoparametric elements. *Proc. Sixth World Conf. on Finite Element Methods*: 520-529.
- Magri, F., 2004. Derivation of the coefficients of thermal expansion and compressibility for use in FEFLOW. *WASY White papers, III*: 13-23.
- Mercer, J.W. and Pinder, G.F., 1974. Finite element analysis of hydrothermal systems. *Finite Element Methods in Flow Problems*. Proc. 1st Symp., Swansea, ed. Oden, J. T. et al., Univ. of Alabama Press: 401-414.
- Meyer, H., Schönicke, L., Wand, U., Hubberten, H. and Fridrichsen, H., 2000. Isotope studies of hydrogen and oxygen in ground ice - Experiences with the equilibration technique. *Isotopes Environ. Health Stud.*, 36: 133-149.
- Möller, P., Dulski, P. and Morteani, G., 2003. Partitioning of rare earth elements yttrium and some major elements among source rocks, liquid and vapor of Larderello-Travale Geothermal Field, Tuscany (Central Italy). *Geochim.Cosmochim. Acta*, 67: 171-183.
- Müller, E. and Papendieck, G., 1975. Zur Verteilung , Genese und Dynamik von Tiefenwässern unter besonderer Berücksichtigung des Zechsteins. *Zt. geol. Wiss.*, 3(2): 167-196.

- Musgrove, M. and Banner, J.L., 1993. Regional ground-water mixing and the origin of saline fluids; midcontinent, United States. *Science*, 259(5103): 1877-1882.
- Naumann, 2000. *Salinare Tiefenwässer in Norddeutschland: Gas- und isotopengeochemische Untersuchungen zur Herkunft und geothermischen Nutzung*, Potsdam.
- Neumann, 1975. *Hydrogeologische Verhältnisse des Paläozoikums und Mesozoikums am Nordrand der Norddeutsch-Polnischen Senke und ihre Beziehungen zu den Erdöl- und Erdgasvorkommen*, Freiberg.
- Nield, D.A., 1968. Onset of thermohaline convection in a porous medium. *Water Resources Research*, 4(3): 553-560.
- Nield, D.A., 1974. Comments on "Effect of solute dispersion on thermal convection in a porous medium layer". *Water Resources Research*, 10: 889.
- Nield, D.A., 1991. The stability of convective flows in porous media. *Convective heat and mass transfer in porous media*: 79-122.
- Nield, D.A. and Bejan, A., 1999. *Convection in porous media*. Springer, New York, 546 pp.
- Oldenburg, C.M. and Pruess, K., 1998. Layered thermohaline convection in hypersaline geothermal systems. *Transport in Porous Media*, 33(1-2): 29-63.
- Oldenburg, C.M. and Pruess, K., 1999. Plume separation by transient thermohaline convection in porous media. *Geophysical Research Letters*, 26(19): 2997-3000.
- Ortega, J.M. and Rheinboldt, W.C., 1970. *Iterative solution of nonlinear equations in several variables*. Academic Press, New York.
- Person, M., Raffensperger, J.P., Ge, S. and Garven, G., 1996. Basin-scale hydrogeologic modeling. *Reviews of Geophysics*, 34(1): 61-87.
- Posey, H.H. and Kyle, J.R., 1988. Fluid -rock interactions in the salt dome environment: an introduction and review. *Chemical Geology*, 74(1-2): 1-24.
- Qin, Y., Guo, J. and Kaloni, P., 1995. Double diffusive penetrative convection in porous media. *International J. Engng. Sci.*, 33(3): 303-312.
- Ranganathan, V. and Hanor, J.S., 1988. Density-driven groundwater flow near salt domes. *Chemical Geology*, 74(1-2): 173-188.
- Rayleigh, J.W.S., 1883. Investigation of the character of the equilibrium of an incompressible heavy fluid of variable density. *Proc. London Math. Soc*, 14: 170-177.
- Rayleigh, L., 1916. On convection currents in a orizontal layer of fluid when the higher temperature is on the under side. *Philos.Mag.*, Ser. 6 32: 529-546.
- Reese, R.S., 2003. Hydrogeology and the distribution and the origin of salinity in he Floridian aquifer system, Southeastern Florida. 94-4010.

- Rockel, W., Hoth, P. and Seibt, A., 1997. Charakteristik und Aufschluss hydrogeothermaler Speicher. *Geowissenschaften*, 15(8): 244-252.
- Rosenberg, N.D. and Spera, F.J., 1990. Role of anisotropic and/or layered permeability in hydrothermal convection. *Geophysical Research Letters*, 17(3): 235-238.
- Rosenberg, N.D. and Spera, F.J., 1992. Convection in porous media with thermal and chemical buoyancy: a comparison of two models for solute dispersion. *Chaotic Processes in the Geological Science, IMA Volume in Mathematics and Its Applications*: 319-333.
- Rosenberg, N.D. and Spera, F.J., 1992. Thermohaline convection in a porous medium heated from below. *International Journal of Heat and Mass Transfer*, 35(5): 1261-1273.
- Rubin, H., 1975. Effect of solute dispersion on thermal convection in a porous medium layer. *Water Resources Research*, 11: 154-158.
- Rutter, 1988. Hydrogeologische Einschätzung des Saxons im Beckenzentrum und angrenzender Gebiete. Abschlussbericht VEB Geol. Forsch. und Erk. Halle BT Stendal.
- Sarkar, A., Nunn, J.A. and Hanor, J.S., 1995. Free thermohaline convection beneath allochthonous salt sheets: an agent for salt dissolution and fluid flow in Gulf Coast sediments. *Journal of Geophysical Research*, 100: 18,085-18,092.
- Scheck, M., 1997. Dreidimensional Strukturmodellierung des Nordostdeutschen Beckens unter Einbeziehung von Krustenmodellen, Geoforschungszentrum Potsdam.
- Scheck, M. and Bayer, U., 1999. Evolution of the Northeast German Basin - inferences from a 3D structural model and subsidence analysis. *Tectonophysics*, 313(1-2): 145-169.
- Schincariol, R.A., Schwartz, F.W. and Mendoza, C.A., 1994. On the generation of instabilities in variable density flow. *Water Resources Research*, 30(4): 913-927.
- Schirrmeister, W., 1996. Aus der Literatur überlieferte Angaben über natürliche Salzwasseraustritte an der Grundwasseroberfläche/Geländeoberfläche in Brandenburg. *Brandenburgische Geowissenschaftliche Beiträge*, 3: 94-96.
- Simmons, C.T., Fenstemaker, T.R. and Sharp, J.M., 2001. Variable-density groundwater flow and solute transport in heterogeneous porous media: approaches, resolutions and future challenges. *Journal of Contaminant Hydrology*, 52: 245-275.
- Simms, M.A. and Garven, G., 2004. Thermal convection in faulted extensional sedimentary basins: Theoretical results from finite-element modeling. *Geofluids*, 4(2): 109-130.
- Sorey, M.L., 1976. Numerical modeling of liquid geothermal systems. USGS Open File Report: 75-613.
- Stern, M.E., 1960. The salt fountain and thermohaline convection. *Tellus*, 12: 172-175.
- Stommel, H., Arons, A.B., Blanchard, D., 1956. An oceanographic curiosity: the perpetual salt fountain. *Deep sea Res.*, 3: 152-153.

- Straus, J.M., 1979. Large amplitude convection in porous media. *Journal of Fluid Mechanics*, 64: 51-63.
- Straus, J.M. and Schubert, G., 1977. Thermal convection of water in a porous medium: effects of temperature and pressure dependent thermodynamic and transport properties. *Journal of Geophysical Research*, 82: 325-333.
- Tan, K., Sam, T. and Jamaludin, H., 2003. The onset of transient convection in bottom heated porous media. *International Journal of Heat and Mass Transfer*, 46: 2857-2873.
- Tesmer, M. et al., submitted. Deep-reaching fluid flow in the North East German Basin. Origin and processes of ground water salinization. *International Journal of Geoscience*.
- Thomas, 1994. Hydrogeochemische Untersuchungen an Ölfeldwässern aus dem NM-Deutschland und dem Oberrheingraben und ihre Modellierung unter dem Aspekt eines Expertensystems für Fluid-Rock-Interactions (XPS Frocki), Berlin.
- Trettin, R., Haase, G. and Haberdank, M., 1990.  $^{87}\text{Sr}/^{86}\text{Sr}$ -Untersuchungen an Grundwässern des Berliner Urstromtales. *Isotopenpraxis*, 26(12): 595-598.
- Trettin, R., Hiller, A., Wolf, M., Deibel, K. and Gläßer, W., 1997. Isotopenanalytische Charakterisierung tiefliegender Grundwässer im Raum der Fürstenwalde-Gubener Störungszone. *Grundwasser*, Berlin; Heidelberg, 2,2: 65-76.
- Trevisan, O.V. and Bejan, A., 1987. Mass and Heat Transfer by High Rayleigh Number Convection in a Porous Medium Heated from Below. *International Journal of Heat and Mass Transfer*, 30: 2341-2356.
- Van der Lee, J., De Windt, L., 2001. Present state and future directions of modelling of geochemistry in hydrogeological systems. *Journal of Contaminant Hydrology*, 47: 265-282.
- Voigt, H., 1972. Genese und Hydrochemie mineralisierter Grundwässer. WTI Sonderheft. Berlin, 6.
- Voigt, H., 1975. Zur Dynamik mineralisierter Schichtenwässer. *Z. angew. Geol.*, 21, 4, Berlin.
- Voigt, H., 1977. Zur Geochemie der Spurenelemente Brom, Jod, Bor, Strontium und Lithium in den Mineralwässern des Nordteiles der DDR. *Z. angew. Geol.*, 23, 8, Berlin.
- Wagner, W., 2000. The IAPWS Industrial Formulation 1997 for the Thermodynamic Properties of Water and Steam. *ASME J. Eng. Gas Turbines and Power*, 122: 150-182.
- WASY-GmbH, 2002. FEFLOW finite-element subsurface flow and transport simulation system. User's Manual/Reference Manual/White Papers, Release 5.0, WASY GmbH, Berlin.



# Appendix 1. Fluid, heat and mass transport equations in porous media

## 1.1. *Formulation of the problem of heat and mass transfer in a porous medium (macroscopic level)*

This appendix gives a mathematical description of the problem of heat and mass transfer in a porous medium. The core of the mathematical modeling is defined by the fundamental physical principles of:

- Mass conservation of the fluid
- Mass conservation of the solute
- Conservation of the linear momentum of the fluid
- Energy conservation

In the continuum approach, mass, motion and energy-related quantities can be defined in a 'microscopic' (local) volume element for which balance laws are postulated. Mass, linear momentum and energy represent extensive properties, i.e. quantities which are additive over volumes of the continuum. On the other hand, intensive properties concern densities of these extensive properties being independent of the balance volume.

In principle, given the initial and boundary conditions, the transport problem in a porous medium can be solved at the continuum (microscopic) level. However, this approach is not feasible in practice because at that level it is not possible to describe the configuration of the surface that bounds the considered phase (i.e., the solid surface bounding the considered fluid phase filling the void space) except in simple cases such as a medium composed of straight capillary tubes. Moreover constitutive equations require coefficients that can only be determined experimentally and that obviously can't be measured at a microscopic level in real system.

In order to circumvent these difficulties, the transport problem is lifted from microscopic level to a macroscopic one, i.e. a coarser level of averaging is reached (upscaling or macroscopization). This is still a continuum approach but on a higher level at which quantities can be measured and problem boundaries can be identified. As a consequence, the real porous medium domain is regarded as a conceptual model in which each phase is assumed to behave



as a continuum filling the entire domain. At every point within these continua, values are assigned for the variables and parameters involved, and they are averaged over a Representative Elementary Volume (REV). To allow the passage from the microscopic to the macroscopic level, parameters such as porosity  $\phi$ , tortuosity, permeability  $\mathbf{k}$ , dispersivity  $\mathbf{D}$ , etc. have to be introduced. The numerical value of these coefficients must be determined experimentally or in the field. These coefficients are related to the chosen model of the considered problem but for convention are referred to the porous medium.

At this stage, an important remark on the appropriate size of REV has to be made: since the macroscopic parameters have the meaning of average values over a REV centered in the point where the parameter is measured, the latter will be useful only if the measuring device also averages over the same REV scale. That is, a strong relationship exists between the REV size of a porous medium and the measuring instrument. Moreover, referring to fractured media, the concept of a REV can be impractical or even invalid as in the case where fractures create a non-leaching network (Georgiadis 1991).

To obtain the macroscopic balance equations, some averaging rules (closure) to the corresponding microscopic equations must be applied. The averaging method has been developed over 30 years with majors contributions from Bear and Bachmat (1990), Hassanizadeh and Gray (1979a, 1979b, 1980, 1986a, 1986b). Here the problem of heat and mass transfer in porous medium will be directly formulated as a set of average equations in the dependent average variables  $C, \rho_f, p, \mu, \mathbf{V}^*, T_f, T_s$ . In this context, a single-phase fluid that occupies the entire void space of a porous medium, is considered. In the equations, fluid and solid phase will be labeled with  $f$  and  $s$  subscript, respectively. Fluid is a binary system (for instance, water and a non-reactive solute which concentration is denoted by  $C$ ) with molecular diffusion  $D_{diff}$ . All fluxes are expressed per unit of area.

### Equation 1: Mass conservation of the fluid.

$$\boxed{\begin{aligned} \frac{\partial}{\partial t} \phi \rho_f + \text{div}(\rho_f \mathbf{q}) &= 0 \\ \mathbf{q} &= \phi \mathbf{V}^* \end{aligned}} \quad (1.1)$$

where  $\phi$  is the porosity of the porous medium,  $\mathbf{q}$  is the Darcy (or volumetric flux density velocity) signifying the specific discharge of the fluid,  $\mathbf{V}^*$  is also often referred to as pore

velocity.

Usually the mass conservation balance is implemented in the simulations codes in a different form that can be obtained by developing the derivatives in (1.1):

$$\phi \underbrace{\frac{\partial}{\partial t} \rho_f}_{\rho_f \left( \bar{\alpha} \frac{\partial C}{\partial t} - \bar{\beta} \frac{\partial T}{\partial t} + \bar{\gamma} \frac{\partial p_f}{\partial t} \right)} + \cancel{\rho_f} \underbrace{\frac{\partial}{\partial t} \phi}_{(1-\phi)Y \frac{\partial p_f}{\partial t}} + \cancel{\rho_f} \text{div}(\mathbf{q}) + \mathbf{q} \cdot \underbrace{\text{grad}(\rho_f)}_{\cancel{\rho_f} (\bar{\alpha} \text{grad} C - \bar{\beta} \text{grad} T + \bar{\gamma} \text{grad} p_f)} = 0$$

Simplifications yield to:

$$S_0 \frac{\partial p_f}{\partial t} + \text{div}(\mathbf{q}) = Q_{\text{Bous sin esq}} \quad (1.2)$$

where:

$Q_{\text{Bous sin esq}} = -\mathbf{q} \cdot (\bar{\alpha} \text{grad} C - \bar{\beta} \text{grad} T + \bar{\gamma} \text{grad} \phi) - \phi \left( \bar{\alpha} \frac{\partial C}{\partial t} - \bar{\beta} \frac{\partial T}{\partial t} \right)$  is a term resulting from the developed derivatives of (1.1) which incorporates mass-dependent and temperature dependent compression effects.

$S_0 = \phi \bar{\gamma} + (1 - \phi)Y$  is the specific storage coefficient or medium storativity which physically represents the volume of water released (or added to) from storage in the aquifer per unit volume of aquifer and per unit decline (or rise) of head,  $Y$  being the bulk compressibility.

## Equation 2: Mass conservation of the solute.

$$\frac{\partial \phi C}{\partial t} + \text{div}(\rho_f C \mathbf{q}) + \text{div}(\bar{\mathbf{j}}_c^*) - \text{div}(\mathbf{D}_{\text{disp}} \text{grad}(C)) = Q_c \quad (1.3)$$

$Q^c$  is a mass supply.

Three different kind of fluxes are involved:  $C\mathbf{q}$  is an advective flux,  $\bar{\mathbf{j}}^*$  is a diffusive flux and  $\mathbf{D}_{\text{disp}} \text{grad}(C)$  a dispersive flux. As a phenomenological law, dispersive flux is regarded as a diffusion-like process, hence it depends on a concentration gradient.  $\mathbf{D}_{\text{disp}}$  is the tensor of mechanical dispersion which physical meaning is explained in the next paragraph.

The advective flux represents the quantity of mass advected by the pore velocity  $\mathbf{V}^*$  per unit area of the porous medium.

$\bar{\mathbf{j}}^*$  expresses the flux of the solute at macroscopic level.

$$\bar{\mathbf{j}}_c^* = -\phi \bar{\mathbf{D}}_{\text{diff}} \mathbf{grad}(C) \quad (1.4)$$

Here  $\bar{\mathbf{D}}_{\text{diff}}$  is a tensor and is called coefficient of molecular diffusion in a (saturated) porous medium.

By substituting (1.4) in (1.3):

$$\boxed{\frac{\partial \phi C}{\partial t} + \text{div}(\rho_f \mathbf{q} C) - \text{div}(\mathbf{D} \mathbf{grad}(C)) = Q_C} \quad (1.5)$$

where

$$\mathbf{D} = \mathbf{D}_{\text{disp}} + \phi \bar{\mathbf{D}}_{\text{diff}} \quad (1.6)$$

is the tensor of hydrodynamic dispersion. This coefficient includes the effects of both mechanical dispersion and molecular diffusion.

Hydrodynamic dispersion is a phenomena that arises whenever a solute carried by a fluid flows through a porous medium. For instance, if a uniform flow in a 2D porous medium is considered, experience shows that as flow takes place the solute gradually spreads occupying a portion of the flow domain both in the direction of the uniform flow (referred to as longitudinal) and also in its normal direction (transversal). The observed spreading (at macroscopic level) results from two inseparable processes occurring at microscopic level: the mechanical dispersion and the molecular diffusion. The two basics factor that produce mechanical dispersion are the flow itself and the presence of the pore system through which flow takes place: because of the shape of the interconnected pore space, a close group of tracer particles will spread throughout the flow domain primarily in the longitudinal direction. Essentially, dispersive flux of the mass solute expresses the rate at which mass is transported because of the velocity variations in the void space of the REV. Very little spreading in a direction transversal to the flow can be produced by velocity variations only. Therefore, an additional flux referred to as molecular diffusion takes place in the pore space. In hydrodynamic context, molecular diffusion cannot be separated from mechanical dispersion although molecular diffusion can take place alone also in absence of motion. Its effect on the overall dispersion is more significant at low velocities while at high velocities it can be negligible. A parameter that allows us to estimate which process is dominant in hydrodynamic dispersion is the Peclet number defined as

$$\text{Pe}_D = \frac{L |\mathbf{V}^*|}{\bar{\mathbf{D}}_{\text{diff}}} \quad (1.7)$$

where  $L$  is a characteristic length. The Peclet number is the ratio between rate of transport by convection to the rate of transport by molecular diffusion.

If  $Pe_D \ll 1$  then diffusion will control the flow otherwise if  $Pe_D \gg 1$  the flow is advective-dominated

### Equation 3: Conservation of linear momentum of the fluid (equation of motion).

$$\mathbf{V}^* = -\frac{\mathbf{k}}{\phi\mu_{0f}} f_\mu (\mathbf{grad}(p_f) - \rho_f \mathbf{g}) \quad (1.8)$$

where  $\mathbf{k}$  is the tensor of permeability.

Equation of motion can be rewritten in terms of the piezometric head  $\varphi = z + \frac{p_f}{\rho_{0f}g}$

The differentiation of this relation yields to  $\mathbf{grad}(p_f) = \rho_{0f}g (\mathbf{grad}(\varphi) - 1)$ , hence:

$$\mathbf{q} = -\frac{\mathbf{k}\rho_{0f}g}{\mu_{0f}} f_\mu \mathbf{grad}(\varphi + \frac{\rho_f - \rho_{0f}}{\rho_{0f}}) = -\mathbf{K}f_\mu \mathbf{grad}(\varphi + \frac{\rho_f - \rho_{0f}}{\rho_{0f}}) \quad (1.9)$$

where

$$\mathbf{K} = \frac{\mathbf{k}\rho_{0f}g}{\mu_{0f}} \quad (1.10)$$

is the hydraulic conductivity tensor related to the reference fluid density  $\rho_{0f}$ . Eq. (1.9) is the extension of Darcy's experimental law to a 3D anisotropic media.

The term

$$f_\mu = \frac{\mu_{0f}}{\mu_f(\varphi, C, T)} \quad (1.11)$$

is the viscosity function which takes into account the viscosity effects due to temperature and concentration variations.

$\rho_{0f}$  in Eq. (1.9) and  $\mu_{0f}$  in Eq.(1.11) are both related to the reference conditions for the hydraulic head  $\varphi_0$ , the concentration  $C_0$  and the temperature  $T_{0f}$ .

$\frac{\rho_f - \rho_{0f}}{\rho_{0f}}$  represents the buoyancy term and can be easily derived from of the EOS for  $\rho_f$ .

#### Equation 4: Energy conservation of the fluid and solid.

$$\frac{\partial}{\partial t}(\phi \rho_f c_f T_f) + \text{div}(\rho_f c_f T_f \mathbf{q}) + \text{div}(\bar{\mathbf{j}}_f^{*T}) - \text{div}(\lambda^{\text{disp}}_f \mathbf{grad}(T_f)) = Q^T_f \quad (1.12)$$

In the averaging the term  $\sigma \text{div}(\mathbf{V}^*)$  (rate of internal energy production due to surface force) has been neglected.  $c_f$  is the fluid heat capacity and  $T_f$  is the fluid temperature.

$$\bar{\mathbf{j}}_f^{*T} = -\phi \bar{\lambda}_f^{\text{cond}} \mathbf{grad}(T_f) \quad (1.13)$$

$\bar{\lambda}_f^{\text{cond}}$  tensor of heat conduction of the fluid occupying the void space of a porous medium.

$-\lambda^{\text{disp}}_f \mathbf{grad}(T_f)$  expressed the dispersive heat flux resulting from fluctuations in  $\mathbf{V}^*$  and  $T_f$  in the pore space.  $\lambda^{\text{disp}}_f$  is referred to as tensor of thermal dispersion and conceptually can be considered similar to the mechanical dispersion tensor seen in (1.3)

The macroscopic heat balance equation for the solid phase is:

$$\frac{\partial}{\partial t}((1-\phi) \rho_s c_s T_s) + \text{div}(\bar{\mathbf{j}}_s^{*T}) = Q^T_s \quad (1.14)$$

where  $Q^T_s$  is a heat supply,  $c_s$  is the solid heat capacity,  $T_s$  is the solid temperature and

$$\bar{\mathbf{j}}_s^{*T} = -(1-\phi) \bar{\lambda}_s^{\text{cond}} \mathbf{grad}(T_s) \quad (1.15)$$

is the conductive heat flux in the solid.  $\bar{\lambda}_s^{\text{cond}}$  is named tensor of thermal conductivity of the solid porous matrix.

Because solid grains are relatively small and fluid velocity in the void space is small, solid and liquid phase can be considered in thermal equilibrium, i.e.  $T_f = T_s = T$ . Therefore summing equation (1.12) and (1.14) the heat equation balance for a porous medium as a whole can be obtained.

$$\boxed{\frac{\partial}{\partial t} \left( \underbrace{\left( \phi \rho_f c_f + (1-\phi) \rho_s c_s \right)}_M T \right) + \text{div}(\rho_f c_f T_f \mathbf{q}) - \text{div}(\lambda \mathbf{grad}(T)) = Q^T} \quad (1.16)$$

where

$M$  in the r.h.s. underbrace is often referred to as accumulation term for the heat.

$Q^T$  is the heat supply and

$$\lambda = \underbrace{\phi \bar{\lambda}_f^{\text{cond}} + (1-\phi) \bar{\lambda}_s^{\text{cond}}}_{\bar{\lambda}_p^{\text{cond}}} + \lambda^{\text{disp}} \quad (1.17)$$

$\lambda$  is the thermodispersion tensor, in which the coefficient in the underbrace,  $\lambda_p^{\text{cond}}$  is the thermal conductivity of the saturated porous medium as a whole. The coefficient of thermal dispersion  $\lambda^{\text{disp}}$  can be neglected with respect to  $\lambda_p^{\text{cond}}$  as shown in Bear (1988).

$-\lambda \mathbf{grad}(T)$  combines the conductive heat flux in the fluid and in the solid, and the dispersive heat flux in the fluid.

By observing (1.5) and (1.16) it results that solute is transported at the pore velocity  $\frac{\mathbf{q}}{\phi} = \mathbf{V}^*$  while the heat transport is retarded due to the heat exchange between the fluid and the solid grains ( $M$ , accumulation term for the heat). For a given Darcy velocity  $\mathbf{q}$  the velocity of the advective thermal front is

$$\mathbf{V}_T = \frac{\rho_f c_f \mathbf{q}}{M} = \mathbf{V}^* \underbrace{\frac{\phi \rho_f c_f}{M}}_{1/R} \quad (1.18)$$

Oldenburg and Pruess (1999) estimated that for an hydrothermal convective system the retardation factor  $R$  appearing in (1.18) is approximately 7, i.e. the thermal front will move at 1/7 the speed of the solute front.

The equation of state for the fluid density (1.19) and one for the fluid viscosity (1.20) have to be added:

$$\rho_f = \rho_{f0} \left( 1 + \bar{\gamma}(p_f - p_{f0}) - \bar{\beta}(T_f - T_{f0}) + \bar{\alpha}(C_\alpha - C_{\alpha0}) \right) \quad (1.19)$$

where  $\rho_f = \rho_{f0}$  for  $p_f = p_{f0}$ ,  $T_f = T_{f0}$  and  $C_\alpha = C_{\alpha0}$

$\bar{\gamma}$ ,  $\bar{\beta}$  and  $\bar{\alpha}$  are the coefficient of compressibility, the coefficient of thermal expansion and the mass concentration ratio respectively.

For the fluid viscosity

$$\mu_f = \mu_f(C, T) \quad (1.20)$$

where the concentration and temperature dependencies are determined by empirical polynomial relationships (Hassanizadeh and Leijnse 1988).

In the end, six equations in six dependent variables:  $\mathbf{V}^*, \rho_f, \mu_f, C, p_f, T$  are defined: four balance equations ((1.1) (1.8) (1.5) (1.16)) and two equations of states for  $\rho_f$  and  $\mu_f$ . To complete the mathematical statement of heat and mass transfer problem appropriate initial and boundary conditions must be added.

## Nomenclature

$c$	heat capacity (fluid or solid).	$L^2 T^2 \Theta^{-1}$
$C$	concentration of the solute.	$M L^{-3}$
$D$	hydrodynamic dispersion tensor.	$L^2 T^{-1}$
	concentration of the considered $\alpha$ specie.	
$\bar{D}_{diff}$	molecular diffusion of the saturated porous media.	$L^2 T^{-1}$
$D_{disp}$	mechanical dispersion tensor.	$L^2 T^{-1}$
$g$	vector of gravity acceleration.	$L T^{-2}$
$j^*$	diffusive flux relative to the mass average velocity.	$M L^2 T^{-1}$
$k$	permeability.	$L^2$
$K$	hydraulic conductivity tensor.	$L T^{-1}$
$M$	Heat accumulation term	$M L^{-1} T^{-2} \Theta^{-1}$
$Pe_D$	Peclet number.	1
$p_f$	fluid pressure.	$M L^{-1} T^{-2}$
$q$	Darcy velocity.	$L T^{-1}$
$Q_{Bous sin esq}$	Boussinesq term.	$M L^{-3} T^{-1}$
$Q$	sink/source term.	$M L^{-3} T^{-1}$
$R$	Retardation factor	1
$S_0$	medium storativity.	$L^{-1}$
$T$	temperature.	$\Theta$
$V^*$	pore velocity	$L T^{-1}$

## Greek symbols

$\bar{\alpha}$	mass concentration ratio.	1
$\bar{\beta}$	coefficient of thermal expansion.	$\Theta^{-1}$
$\bar{\gamma}$	coefficient of compressibility.	$L^{-1}$
$\lambda$	thermodispersion tensor.	$M L T^{-3} \Theta^{-1}$

$\bar{\lambda}_f^{\text{cond}}$	tensor of heat conduction of the fluid occupying the void space of a porous medium.	$\text{M L T}^{-3} \Theta^{-1}$
$\lambda_f^{\text{disp}}$	tensor of thermal dispersion.	$\text{M L T}^{-3} \Theta^{-1}$
$\bar{\lambda}_s^{\text{cond}}$	tensor of thermal conductivity of the solid porous matrix.	$\text{M L T}^{-3} \Theta^{-1}$
$\mu$	dynamic fluid viscosity.	$\text{M L}^{-1} \text{T}^{-1}$
$\rho_f$	density of the fluid system.	$\text{M L}^{-3}$
$\phi$	porosity.	1
$\varphi$	piezometric head or Hubbert potential	L
$\sigma$	stress tensor.	$\text{M L}^{-1} \text{T}^{-2}$

### Subscript

$f$	fluid.
$s$	solid.
0	reference values of the considered property.





## Appendix 2. Derivation of the coefficients of thermal expansion and compressibility for use in FEFLOW 5<sup>®</sup>

(Magri 2004)

In this appendix the coefficients of thermal expansion and compressibility appearing in the equation of state for the fluid density (Eq. (1.40 Appendix 1)) will be derived for a wide range of pressure and temperature  $p_{Sat} < p \leq 100$  MPa and  $0 \leq T \leq 350$  °C.

This is of big use for modelling heat transfer in geothermal reservoir such as the NEGB where high temperature and pressure are involved in the simulations. Indeed in thermohaline problems, the fluid density  $\rho^f$  varies with pressure  $p$ , temperature  $T$  and concentration of various components  $C^e$  (where  $C^e$  stands for the  $C^e$ 's of all components present in the fluid) according to relations called equations of state:

$$\rho^f = \rho^f(T, p, C^e) \quad (2.1)$$

From Eq.(2.1) it follows that:

$$\begin{aligned} d\rho^f &= \left. \frac{\partial \rho^f}{\partial T} \right|_{p, C^e} dT + \left. \frac{\partial \rho^f}{\partial p} \right|_{T, C^e} dp + \sum_e \left. \frac{\partial \rho^f}{\partial C^e} \right|_{p, T} dC^e \\ &= \rho^f (\beta dT + \gamma dp + \alpha^e dC^e) \end{aligned} \quad (2.2)$$

where

$$\beta \equiv \frac{1}{\rho^f} \left. \frac{\partial \rho^f}{\partial T} \right|_{p, C^e} \quad (2.3)$$

$$\gamma \equiv \frac{1}{\rho^f} \left. \frac{\partial \rho^f}{\partial p} \right|_{T, C^e} \quad (2.4)$$

$$\alpha^e \equiv \frac{1}{\rho^f} \left. \frac{\partial \rho^f}{\partial C^e} \right|_{p, T} \quad (2.5)$$

with:

$\beta$ : coefficient of thermal expansion at constant pressure and concentration,

$\gamma$ : coefficient of compressibility of the fluid at constant temperature and concentration,

$\alpha^e$ : introduces the effect of a density change due to the concentration of a e-component at constant temperature and pressure.

If, in certain ranges of  $p$ ,  $T$  and  $C$ , the coefficients  $\beta$ ,  $\gamma$  and  $\alpha^e$  are constants or can be approximated as such for a given fluid, the equation of state (Eq.1) takes on the specific form

$$\begin{aligned}\rho^f &= \rho_0^f \exp\left[-\beta(T-T_0) + \gamma(p-p_0) + \sum_e \alpha^e(C^e - C_0^e)\right] \\ &\approx \rho_0^f \left(1 - \bar{\beta}(T-T_0) + \bar{\gamma}(p-p_0) + \sum_e \bar{\alpha}^e(C^e - C_0^e)\right)\end{aligned}\quad (2.6)$$

with

$$\bar{\beta} \equiv - \frac{1}{\rho_0^f} \frac{\partial \rho^f}{\partial T} \Big|_{p, C^e} \quad (2.7)$$

$$\bar{\gamma} \equiv \frac{1}{\rho_0^f} \frac{\partial \rho^f}{\partial p} \Big|_{T, C^e} \quad (2.8)$$

$$\bar{\alpha}^e \equiv \frac{1}{\rho_0^f} \frac{\partial \rho^f}{\partial C^e} \Big|_{T, p} \quad (2.9)$$

where  $\rho^f = \rho_0^f$  when  $T = T_0$ ,  $p = p_0$  and  $C^e = C_0^e$  that is when  $T$ ,  $p$  and  $C^e$  are respectively equal to the reference temperature  $T_0$ , reference pressure  $p_0$  and reference concentration  $C_0^e$ .

Eq.(2.6) states that the density  $\rho^f$  can be approximated by a linear form.

In FEFLOW<sup>®</sup> 5 the following EOS for fluid density is implemented:

$$\rho^f = \rho_0^f \left(1 - \bar{\beta}(T-T_0) + \frac{\bar{\alpha}}{C_s - C_0} (C - C_0)\right) \quad (2.10)$$

with  $\bar{\beta}$  defined in Eq.(2.7) and  $\bar{\alpha}$ , defined in Eq.(2.9), is normalized by the saturation concentration of the solute at saturation,  $C_s$ .

It is important to notice that the EOS for the fluid density coded in the present version of FEFLOW<sup>®</sup> 5 (Eq.10) is valid only in a range of 0-100°C. Moreover it does **not** take in account the coefficient of compressibility  $\bar{\gamma}$  and only **one** component can be considered in the effect of a density change due to its concentration. The following empirical relationship is given for  $\bar{\alpha}$

$$\bar{\alpha} = \frac{\rho^f(C_s) - \rho_0^f}{\rho_0^f} \quad (2.11)$$

While the above linear approximation for  $\bar{\alpha}$  is normally sufficient for the most practical needs, wide ranges of pressure and temperature require variable thermal fluid expansion  $\bar{\beta}$  Eq.(2.7) and fluid compressibility  $\bar{\gamma}$  Eq.(2.8) within the state equation of density Eq.(2.10).

Figure 1 shows the well-known pressure-temperature diagram of water. The phase of interest is the liquid phase in a range of 0-350 °C for the temperature and less or equal than 100 MPa for the pressure. Therefore the area of study in the pressure-temperature diagram is **region 1**, bounded by  $p_{Sat} < p \leq 100 \text{ MPa}$  and  $0 \leq T \leq 350 \text{ °C}$ , where  $p_{Sat}$  is the saturation pressure of water.

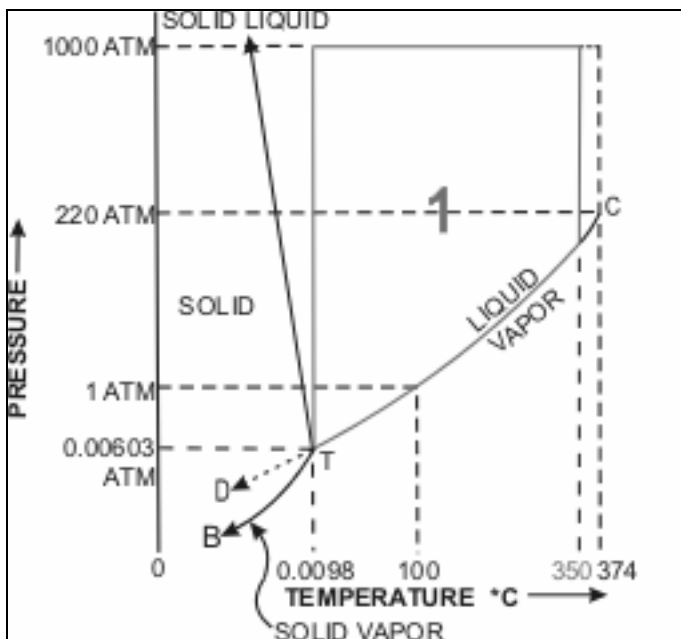


**Fig 1.** Pressure-temperature diagram of water. Our domain of interest is region 1, which boundaries are  $p_{Sat} < p \leq 100 \text{ MPa}$  and  $0 \leq T \leq 350 \text{ °C}$

The following expression provides a good approximation with an accuracy of 0.5% for  $\rho^f$  **in region 1** (figure 1).

with temperature  $T$  in  $^{\circ}\text{C}$  and the pressure  $p$  in kPa. The coefficients of the derived polynomial fitting are:

**Table 2-1.** Coefficients of the polynomial surface fitting of freshwater density  $\rho'(p,T)$  in region 1 as expressed in Eq.(6)

The coefficients have been derived for freshwater conditions, so the surface given by Eq.(2.12) is related to a reference concentration  $C_0=0$ . Fig.2 illustrates the fresh water density  $\rho^f$  as a function of pressure and temperature in region 1.

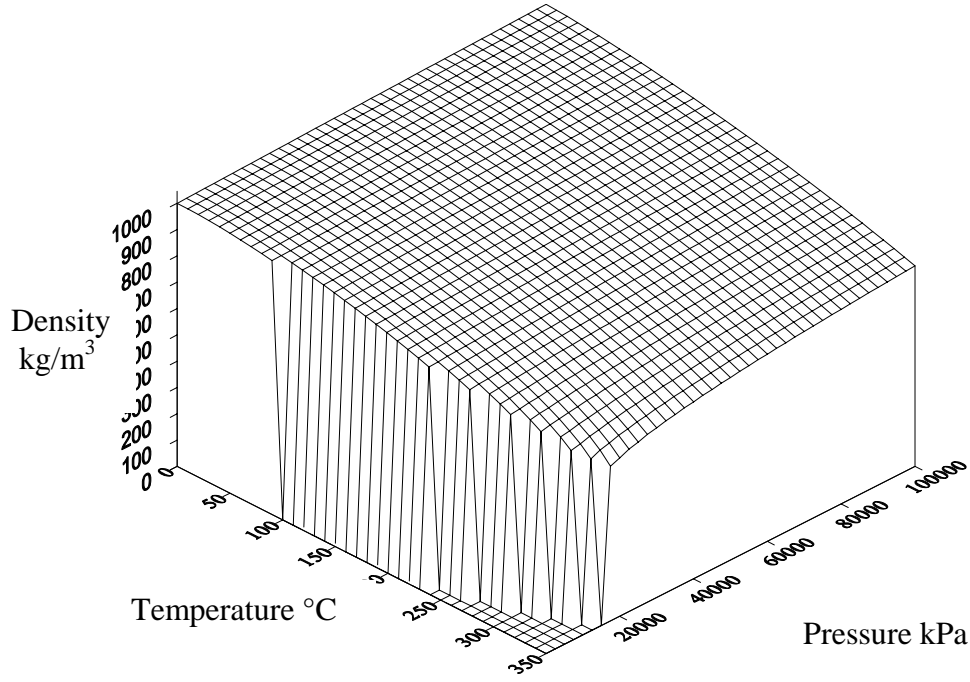


**Figure 2** Fresh water density  $\rho^f$  as a function of pressure and temperature in region 1. For pictorial clarity,  $\rho^f$  is set to zero outside region 1.

The reference fluid density  $\rho_0^f$  can be derived by introducing in Eq.(2.12) the reference temperature  $T_0$  and the reference pressure  $p_0$  leading to:

$$\begin{aligned} \rho_0^f(T_0, C_0, p_0) = & a(p_0)|_{C_0} + b(p_0)|_{C_0} T_0 + c(p_0)|_{C_0} T_0^2 + d(p_0)|_{C_0} T_0^3 + e(p_0)|_{C_0} T_0^4 \\ & + f(p_0)|_{C_0} T_0^5 + g(p_0)|_{C_0} T_0^6 \end{aligned} \quad (2.13)$$

For instance, taking the atmospheric pressure ( $p_0=100$  kPa) and  $T_0=0$  °C as the reference pressure and temperature respectively, from Eq.(2.13) and Eq.(2.12) it follows:

$$\rho_0^f(T_0, C_0, p_0) = a(p_0) = a_0 + a_1 p_0 + a_2 p_0^2 = 998.8396 \text{ [g/l]} \quad (2.14)$$

The goal is to find the thermally variable fluid density  $\bar{\beta}(p, T)$  and the variable fluid compressibility  $\bar{\gamma}(p, T)$  of the fluid density function

$$\rho^f = \rho_0^f \left[ 1 + \underbrace{\bar{\gamma}(T, p)}_{\text{variable expansion}} (p - p_0) - \underbrace{\bar{\beta}(T, p)}_{\text{variable expansion}} (T - T_0) \right] \quad (2.15)$$

in order to implement them in FEFLOW<sup>®</sup> 5. No effects from concentration of a component are taken in account in the fluid density since these are already included in FEFLOW as shown in Eq.(2.10)

Let's consider a Taylor series expansion for the fluid density  $\rho^f(T, p)$  around  $T_0$  and  $p_0$  where a 6<sup>th</sup> order approximation is used for the temperature  $T$  and a 2<sup>nd</sup> order approximation is used for the pressure dependence, viz.,

$$\begin{aligned} \rho^f(T, p) = & \rho^f(T_0, p_0) + (\rho^f)^{(1,0)} \Big|_{T_0, p_0} (T - T_0) + \frac{1}{2} (\rho^f)^{(2,0)} \Big|_{T_0, p_0} (T - T_0)^2 + \\ & \frac{1}{3!} (\rho^f)^{(3,0)} \Big|_{T_0, p_0} (T - T_0)^3 + \frac{1}{4!} (\rho^f)^{(4,0)} \Big|_{T_0, p_0} (T - T_0)^4 + \frac{1}{5!} (\rho^f)^{(5,0)} \Big|_{T_0, p_0} (T - T_0)^5 + \\ & \frac{1}{6!} (\rho^f)^{(6,0)} \Big|_{T_0, p_0} (T - T_0)^6 + (p - p_0) \left[ (\rho^f)^{(0,1)} \Big|_{p_0, T_0} + (\rho^f)^{(1,1)} \Big|_{T_0, p_0} (T - T_0) + \right. \\ & \frac{1}{2} (\rho^f)^{(2,1)} \Big|_{T_0, p_0} (T - T_0)^2 + \frac{1}{3!} (\rho^f)^{(3,1)} \Big|_{T_0, p_0} (T - T_0)^3 + \frac{1}{4!} (\rho^f)^{(4,1)} \Big|_{T_0, p_0} (T - T_0)^4 + \\ & \left. \frac{1}{5!} (\rho^f)^{(5,1)} \Big|_{T_0, p_0} (T - T_0)^5 + \frac{1}{6!} (\rho^f)^{(6,1)} \Big|_{T_0, p_0} (T - T_0)^6 \right] + (p - p_0)^2 \left[ \frac{1}{2} (\rho^f)^{(0,2)} \Big|_{T_0, p_0} + \right. \\ & \frac{1}{2} (\rho^f)^{(1,2)} \Big|_{T_0, p_0} (T - T_0) + \frac{1}{4} (\rho^f)^{(2,2)} \Big|_{T_0, p_0} (T - T_0)^2 + \frac{1}{12} (\rho^f)^{(3,2)} \Big|_{T_0, p_0} (T - T_0)^3 + \\ & \left. \frac{1}{48} (\rho^f)^{(4,2)} \Big|_{T_0, p_0} (T - T_0)^4 + \frac{1}{240} (\rho^f)^{(5,2)} \Big|_{T_0, p_0} (T - T_0)^5 + \frac{1}{1440} (\rho^f)^{(6,2)} \Big|_{T_0, p_0} (T - T_0)^6 \right] \end{aligned} \quad (2.16)$$

where

$$(\rho^f)^{(i,j)} \Big|_{T_0, p_0} \equiv \frac{\partial^{i+j} \rho^f(T, p)}{\partial T^i \partial p^j} \Big|_{T_0, p_0} \quad (2.17)$$

By utilizing Eq.(2.12), the above derivatives (Eq.(2.17)) can be calculated at  $p_0$  and  $T_0$  leading to the following equation:

$$\begin{aligned}
\rho^f(T, p) = & a_0 + p_0 a_1 + p_0^2 a_2 + T_0(b_0 + p_0 b_1 + p_0^2 b_2) + T_0^2(c_0 + p_0 c_1 + p_0^2 c_2) + T_0^3(d_0 + p_0 d_1 + p_0^2 d_2) + \\
& T_0^4(e_0 + p_0 e_1 + p_0^2 e_2) + T_0^5(f_0 + p_0 f_1 + p_0^2 f_2) + T_0^6(g_0 + p_0 g_1 + p_0^2 g_2) + \\
& (T - T_0)^6(g_0 + p_0 g_1 + p_0^2 g_2) + (T - T_0)^5(f_0 + p_0 f_1 + p_0^2 f_2 + 6T_0(g_0 + p_0 g_1 + p_0^2 g_2)) + \\
& (T - T_0)^4(e_0 + p_0 e_1 + p_0^2 e_2 + 5T_0(f_0 + p_0 f_1 + p_0^2 f_2) + 15T_0^2(g_0 + p_0 g_1 + p_0^2 g_2)) + \\
& (T - T_0)^3(d_0 + p_0 d_1 + p_0^2 d_2 + 4T_0(e_0 + p_0 e_1 + p_0^2 e_2) + 10T_0^2(f_0 + p_0 f_1 + p_0^2 f_2) + 20T_0^3(g_0 + p_0 g_1 + p_0^2 g_2)) + \\
& (T - T_0)^2(c_0 + p_0 c_1 + p_0^2 c_2 + 3T_0(d_0 + p_0 d_1 + p_0^2 d_2) + 6T_0^2(e_0 + p_0 e_1 + p_0^2 e_2) + 10T_0^3(f_0 + p_0 f_1 + p_0^2 f_2) + \\
& 15T_0^4(g_0 + p_0 g_1 + p_0^2 g_2)) + \\
& (T - T_0)(b_0 + p_0 b_1 + p_0^2 b_2 + 2T_0(c_0 + p_0 c_1 + p_0^2 c_2) + 3T_0^2(d_0 + p_0 d_1 + p_0^2 d_2) + 4T_0^3(e_0 + p_0 e_1 + p_0^2 e_2) + \\
& 5T_0^4(f_0 + p_0 f_1 + p_0^2 f_2) + 6T_0^5(g_0 + p_0 g_1 + p_0^2 g_2)) + \\
& (p - p_0)^2(a_2 + T_0 b_2 + T_0^2 c_2 + T_0^3 d_2 + T_0^4 e_2 + T_0^5 f_2 + T_0^6 g_2 + (T - T_0)^6 g_2 + (T - T_0)^5(f_2 + 6T_0 g_2) + \\
& (T - T_0)^4(e_2 + 5T_0 f_2 + 15T_0^2 g_2) + (T - T_0)^3(d_2 + 4T_0 e_2 + 10T_0^2 f_2 + 20T_0^3 g_2) + \\
& (T - T_0)^2(c_2 + 3T_0 d_2 + 6T_0^2 e_2 + 10T_0^3 f_2 + 15T_0^4 g_2) + \\
& (T - T_0)(b_2 + 2T_0 c_2 + 3T_0^2 d_2 + 4T_0^3 e_2 + 5T_0^4 f_2 + 6T_0^5 g_2)) + \\
& (p - p_0)[a_1 + 2p_0 a_2 + T_0(b_1 + 2p_0 b_2) + T_0^2(c_1 + 2p_0 c_2) + T_0^3(d_1 + 2p_0 d_2) + T_0^4(e_1 + 2p_0 e_2) + \\
& T_0^5(f_1 + 2p_0 f_2) + T_0^6(g_1 + 2p_0 g_2) + (T - T_0)^6(g_1 + 2p_0 g_2) + (T - T_0)^5(f_1 + 2p_0 f_2 + 6T_0(g_1 + 2p_0 g_2)) + \\
& (T - T_0)^4(e_1 + 2p_0 e_2 + 5T_0(f_1 + 2p_0 f_2) + 15T_0^2(g_1 + 2p_0 g_2)) + \\
& (T - T_0)^3(d_1 + 2p_0 d_2 + 4T_0(e_1 + 2p_0 e_2) + 10T_0^2(f_1 + 2p_0 f_2) + 20T_0^3(g_1 + 2p_0 g_2)) + \\
& (T - T_0)^2(c_1 + 2p_0 c_2 + 3T_0(d_1 + 2p_0 d_2) + 6T_0^2(e_1 + 2p_0 e_2) + 10T_0^3(f_1 + 2p_0 f_2) + 15T_0^4(g_1 + 2p_0 g_2)) + \\
& (T - T_0)(b_1 + 2p_0 b_2 + 2T_0(c_1 + 2p_0 c_2) + 3T_0^2(d_1 + 2p_0 d_2) + 4T_0^3(e_1 + 2p_0 e_2) + \\
& 5T_0^4(f_1 + 2p_0 f_2) + 6T_0^5(g_1 + 2p_0 g_2))] \quad (2.18)
\end{aligned}$$

Comparing the above equation with the EOS for the fluid density Eq.(2.15) the expression for the coefficient of thermal expansion and the coefficient of compressibility are obtained, viz.

$$\begin{aligned}
\bar{\beta}(T, p) = & -\frac{1}{\rho_0^f} \left[ (T - T_0)^5(g_0 + p_0 g_1 + p_0^2 g_2) + (T - T_0)^4(f_0 + p_0 f_1 + p_0^2 f_2 + 6T_0(g_0 + p_0 g_1 + p_0^2 g_2)) + \right. \\
& (T - T_0)^3(e_0 + p_0 e_1 + p_0^2 e_2 + 5T_0(f_0 + p_0 f_1 + p_0^2 f_2) + 15T_0^2(g_0 + p_0 g_1 + p_0^2 g_2)) + \\
& (T - T_0)^2(d_0 + p_0 d_1 + p_0^2 d_2 + 4T_0(e_0 + p_0 e_1 + p_0^2 e_2) + 10T_0^2(f_0 + p_0 f_1 + p_0^2 f_2) + 20T_0^3(g_0 + p_0 g_1 + p_0^2 g_2)) + \\
& (T - T_0)(c_0 + p_0 c_1 + p_0^2 c_2 + 3T_0(d_0 + p_0 d_1 + p_0^2 d_2) + 6T_0^2(e_0 + p_0 e_1 + p_0^2 e_2) + 10T_0^3(f_0 + p_0 f_1 + p_0^2 f_2) + \\
& 15T_0^4(g_0 + p_0 g_1 + p_0^2 g_2)) + \\
& (b_0 + p_0 b_1 + p_0^2 b_2 + 2T_0(c_0 + p_0 c_1 + p_0^2 c_2) + 3T_0^2(d_0 + p_0 d_1 + p_0^2 d_2) + 4T_0^3(e_0 + p_0 e_1 + p_0^2 e_2) + \\
& 5T_0^4(f_0 + p_0 f_1 + p_0^2 f_2) + 6T_0^5(g_0 + p_0 g_1 + p_0^2 g_2)) \left. \right] \quad (2.19)
\end{aligned}$$

and



$$\begin{aligned}
\bar{\gamma}(T, p) = \frac{1}{\rho_0^f} & \left\{ (p - p_0) \left( a_2 + T_0 b_2 + T_0^2 c_2 + T_0^3 d_2 + T_0^4 e_2 + T_0^5 f_2 + T_0^6 g_2 + (T - T_0)^6 g_2 + (T - T_0)^5 (f_2 + 6T_0 g_2) + \right. \right. \\
& (T - T_0)^4 (e_2 + 5T_0 f_2 + 15T_0^2 g_2) + (T - T_0)^3 (d_2 + 4T_0 e_2 + 10T_0^2 f_2 + 20T_0^3 g_2) + \\
& (T - T_0)^2 (c_2 + 3T_0 d_2 + 6T_0^2 e_2 + 10T_0^3 f_2 + 15T_0^4 g_2) + \\
& \left. (T - T_0)(b_2 + 2T_0 c_2 + 3T_0^2 d_2 + 4T_0^3 e_2 + 5T_0^4 f_2 + 6T_0^5 g_2) \right) + \\
& \left[ a_1 + 2p_0 a_2 + T_0(b_1 + 2p_0 b_2) + T_0^2(c_1 + 2p_0 c_2) + T_0^3(d_1 + 2p_0 d_2) + T_0^4(e_1 + 2p_0 e_2) + \right. \\
& T_0^5(f_1 + 2p_0 f_2) + T_0^6(g_1 + 2p_0 g_2) + (T - T_0)^6(g_1 + 2p_0 g_2) + (T - T_0)^5(f_1 + 2p_0 f_2 + 6T_0(g_1 + 2p_0 g_2)) + \\
& (T - T_0)^4(e_1 + 2p_0 e_2 + 5T_0(f_1 + 2p_0 f_2) + 15T_0^2(g_1 + 2p_0 g_2)) + \\
& (T - T_0)^3(d_1 + 2p_0 d_2 + 4T_0(e_1 + 2p_0 e_2) + 10T_0^2(f_1 + 2p_0 f_2) + 20T_0^3(g_1 + 2p_0 g_2)) + \\
& (T - T_0)^2(c_1 + 2p_0 c_2 + 3T_0(d_1 + 2p_0 d_2) + 6T_0^2(e_1 + 2p_0 e_2) + 10T_0^3(f_1 + 2p_0 f_2) + 15T_0^4(g_1 + 2p_0 g_2)) + \\
& (T - T_0)(b_1 + 2p_0 b_2 + 2T_0(c_1 + 2p_0 c_2) + 3T_0^2(d_1 + 2p_0 d_2) + 4T_0^3(e_1 + 2p_0 e_2) + \\
& \left. \left. 5T_0^4(f_1 + 2p_0 f_2) + 6T_0^5(g_1 + 2p_0 g_2) \right) \right] \left. \right\} \quad (2.20)
\end{aligned}$$

with  $\rho_0^f$  computed from Eq.(2.14) and the coefficients  $(a_k, b_k, c_k, d_k, e_k, f_k, g_k)_{k=0,1,2}$  are given in Table 2-1.

These two expressions can be implemented in FEFLOW by the use of the interface manager (IFM) as shown in Appendix 3.

## Appendix 3. Implementation of the coefficient of thermal expansion and compressibility through the IFM interface manager for use with FEFOW 5 (Magri 2004)

Here the equations derived in Appendix 2 for the coefficient of thermal expansion and compressibility will be implemented in FEFLOW through the IFM interface. The definitions of the coefficients involved in the equations are given in Appendix 2.

### Goal

The goal is to incorporate in FEFLOW the following EOS

$$\rho^f = \rho_0^f \left( 1 - \bar{\beta}(T, p)(T - T_0) + \bar{\gamma}(T, p)(p - p_0) + \frac{\bar{\alpha}}{C_s - C_0}(C - C_0) \right) \quad (3.1)$$

in order to reproduce the fluid density for a wide range of temperature and pressure ( $p_{Sat} < p \leq 100$  MPa and  $0 \leq T \leq 350$  °C).

For this purpose Eq.(3.1) must include the equations for  $\bar{\beta}(T, p)$  and  $\bar{\gamma}(T, p)$  derived in Appendix 2 (Eq.(2.19) and Eq.(2.20)). From now on these equations are referred to freshwater condition ( $C_0=0$  g/l) at the atmospheric pressure ( $p_0=100$  kPa) and at triple point temperature ( $T_0=0$  °C) , i.e.

$$\bar{\beta}(T, p) = - \frac{1}{\rho_0^f} \left[ T^5(g_0 + p_0 g_1 + p_0^2 g_2) + T^4(f_0 + p_0 f_1 + p_0^2 f_2) + T^3(e_0 + p_0 e_1 + p_0^2 e_2) + T^2(d_0 + p_0 d_1 + p_0^2 d_2) + T(c_0 + p_0 c_1 + p_0^2 c_2) + (b_0 + p_0 b_1 + p_0^2 b_2) \right] \quad (3.2)$$

and

$$\bar{\gamma}(T, p) = \frac{1}{\rho_0^f} \left[ (p - p_0)(a_2 + T^6 g_2 + T^5 f_2 + T^4 e_2 + T^3 d_2 + T^2 c_2 + T b_2) + a_1 + 2p_0 a_2 + T^6(g_1 + 2p_0 g_2) + T^5(f_1 + 2p_0 f_2) + T^4(e_1 + 2p_0 e_2) + T^3(d_1 + 2p_0 d_2) + T^2(c_1 + 2p_0 c_2) + T(b_1 + 2p_0 b_2) \right] \quad (3.3)$$

where  $\rho_0^f(T_0, C_0, p_0) = 998.8396$  [g/l] and the coefficients are given in Table 2.1 (Appendix 2)

## Equation to implement

In FEFLOW 5 the following EOS for the fluid density is incorporated:

$$\rho^f = \rho_0^f \left( 1 - \bar{\beta}(T - T_0) + \frac{\bar{\alpha}}{C_s - C_0} (C - C_0) \right) \quad (3.4)$$

For achieving the cited goal, an external module coding the new expression of  $\bar{\beta}(T, p)$  (Eq.(3.2) and  $\bar{\gamma}(T, p)$  (Eq.(3.3)) has been implemented in the EOS Eq.(3.4). The implementation of  $\bar{\beta}(T, p)$  can be done directly by the use of the IFM. The IFM offers the users different Application Programming Interfaces (API) whereby external codes can be linked. For instance, the coefficient of thermal expansion can be implemented in FEFLOW via the API “IfmSetMatFlowExpansionCoeff”. On the other hand the EOS for the fluid density present in FEFLOW (Eq.4) does not take in account the coefficient of compressibility  $\bar{\gamma}(T, p)$ . Therefore no related API interface exists for this coefficient and it's not possible to implement directly the expression for  $\bar{\gamma}(T, p)$  (Eq.(3.2)) into Eq.(3.4). Therefore, to make up for this lack, a little trick is required:

Let's apply a simple factorisation in the EOS for the fluid density to be incorporated into FEFLOW (Eq.(3.1)):

$$\begin{aligned} \rho^f &= \rho_0^f \left( 1 - \bar{\beta}(T, p)(T - T_0) + \bar{\gamma}(T, p)(p - p_0) + \frac{\bar{\alpha}}{C_s - C_0} (C - C_0) \right) \\ &= \rho_0^f \left( 1 - \left( \bar{\beta}(T, p) - \bar{\gamma}(T, p) \frac{(p - p_0)}{(T - T_0)} \right) (T - T_0) + \frac{\bar{\alpha}}{C_s - C_0} (C - C_0) \right) \\ &= \rho_0^f \left( 1 - \bar{\beta}^*(T, p)(T - T_0) + \frac{\bar{\alpha}}{C_s - C_0} (C - C_0) \right) \end{aligned} \quad (3.5)$$

with

$$\underbrace{\bar{\beta}^*(T, p)}_{\substack{\text{Defined as BETASTAR} \\ \text{in the source code}}} = \left( \underbrace{\bar{\beta}(T, p)}_{\substack{\text{Defined as BETA} \\ \text{in the source code}}} - \underbrace{\bar{\gamma}(T, p) \frac{(p - p_0)}{(T - T_0)}}_{\substack{\text{Defined as GAMMASTAR} \\ \text{in the source code}}} \right) \quad T \neq T_0 \quad (3.6)$$

and  $\bar{\beta}(T, p)$ ,  $\bar{\gamma}(T, p)$  expressed in Eq.(3.3) and Eq.(3.4) respectively.

In this way, a new variable,  $\bar{\beta}^*(T, p)$  has been derived.  $\bar{\beta}^*(T, p)$  takes in account the coefficient of thermal expansion  $\bar{\beta}(T, p)$  and compressibility  $\bar{\gamma}(T, p)$ . This new variable can be directly implemented in the EOS of the fluid density present in FEFLOW (Eq.(3.4)) through the API “IfmSetMatFlowExpansionCoeff” leading to the EOS Eq.(3.1).

### **Description of the source code Beta\_Gamma.c**

The input parameters required for calculating  $\bar{\beta}^*(T, p)$  are the temperature (T) and pressure (p) of each element of the FE mesh. The temperature and pressure are nodal values therefore the code has to calculate the temperature and mean pressure of the grid element. This can be easily done by summing the nodal values of the considered physical parameters and then dividing this sum by the number of nodes of the element.

Below is attached the complete source code Beta\_Gamma.C. The proprietary code has been programmed in C++ language through the IFM tool.

The nodal values of temperature and pressure are loaded by the use of the API functions “IfmGetResultsTransportHeatValue”

and “IfmGetResultsFlowPressureValue” respectively.  $\bar{\beta}^*(T, p)$  is calculated for each mesh element by use of Eq.6. The resulting value is fully implemented in FEFLOW via the API function “IfmSetMatFlowExpansionCoeff”.

```

static void PostTimeStep (IfmDocument pDoc)
{
    int e, i;
    double T, p, A, B;
    double beta, gammastar, BETASTAR;

    /* Coefficients for the fitting and its derivatives */
    /* Useless a0 = 9.99792877961606e+02; */
    double a1 = 5.07605113140940e-04;
    double a2 = -5.28425478164183e-10;
    double b0 = 5.13864847162196e-02;
    double b1 = -3.61991396354483e-06;
    double b2 = 7.97204102509724e-12;
    double c0 = -7.53557031774437e-03;
    double c1 = 6.32712093275576e-08;
    double c2 = -1.66203631393248e-13;
    double d0 = 4.60380647957350e-05;
    double d1 = -5.61299059722121e-10;
    double d2 = 1.80924436489400e-15;
    double e0 = -2.26651454175013e-07;
    double e1 = 3.36874416675978e-12;
    double e2 = -1.30352149261326e-17;
    double f0 = 6.14889851856743e-10;
    double f1 = -1.06165223196756e-14;
    double f2 = 4.75014903737416e-20;
    double g0 = -7.39221950969522e-13;
    double g1 = 1.42790422913922e-17;
    double g2 = -7.13130230531541e-23;
    /*Reference pressure is 100kPa while REFERENCE TEMPERATURE IS 0!!!!!!!*/
    double p0 = 100.;

    /* Number of elements and number of nodes */
    int nElements = IfmGetNumberOfElements(pDoc);
    int nNodes = IfmGetNumberOfNodesPerElement(pDoc);

    /* Loop through all elements */
    for (e = 0; e < nElements; e++)
    {
        T = 0.;
        p = 0.;

        /* loop locally through all nodes of this element */
        for (i = 0; i < nNodes; i++)
        {
            /* Get global node index */
            int indNode = IfmGetNode(pDoc, e, i);
            /*T +=IfmGetResultsTransportHeatPreviousTimeValue(pDoc,indNode);*/
            T +=IfmGetResultsTransportHeatValue(pDoc,indNode);
            p +=IfmGetResultsFlowPressureValue(pDoc,indNode);
        }

        /* Solving the average physical properties (T and p) of this element */
        T /=(double)nNodes;
        p /=(double)nNodes;

        A = gam0+(gam1+(gam2+(gam3+(gam4+(gam5+gam6*T)*T)*T)*T)*T;
        B = a2+(b2+(c2+(d2+(e2+(f2+g2*T)*T)*T)*T)*T;

        /* Set BETA */
        beta = -(1/999.843633188666)*(bp0+(cp0+(dp0+(ep0+(fp0+gp0*T)*T)*T)*T)*T);

        /* Set GAMMA */
        gammastar = -(1/999.843633188666)*(A+B*(p-p0))/(T+.1);

        /* Set BETASTAR */
        BETASTAR=beta+gammastar;
        IfmSetMatFlowExpansionCoeff(pDoc, e, BETASTAR);
    }
}

```

Definition of the coefficients

Solving the average value for  
Temperatue (T) and prfessure (p)

Setting  $\bar{\beta}^i(T, p)$  as expressed in  
Eq.6

## Validation of the code.

The equations for  $\bar{\beta}(T, p)$  and  $\bar{\gamma}(T, p)$  (Eq.(3.2) and Eq.(3.3) have been derived from the following polynomial fitting:

$$\rho^f(T, p) = a(p) + b(p)T + c(p)T^2 + d(p)T^3 + e(p)T^4 + f(p)T^5 + g(p)T^6 \quad \text{in } [\text{kg/m}^3] \quad (3.7)$$

$0 \leq T \leq 350$  and  $p_{\text{sat}} < p \leq 100$

with temperature  $T$  in °C , the pressure  $p$  in kPa and the coefficients for fresh water are given in Table 2.1 (Appendix 2).

For validating the source code, the implemented Beta\_Gamma module has been tested on a vertical 2D coupled heat transport and fluid flow simulation (i.e.  $\bar{\alpha} = 0$ ). In this way it is possible to compare the fluid density calculated from the simulation (Eq.5) with the one provided by the polynomial fitting (Eq.(3.7)). The code is valid only if these values coincide.

The conceptual model used for the coupled simulation is a 3.5 x 3.5 km square. The rectangular mesh is composed by 9 elements. At the top, a constant temperature of 10 °C and a head value of 0 m are set as boundary conditions while at the bottom a constant temperature of 150 °C is set.

The temperature and the pressure are calculated during the simulation process at each node of the considered element. The implemented Beta\_Gamma module derives the elemental mean value of these physical parameters and uses them as input data for returning the elemental value of BETASTAR. Results are shown in Fig 1.

For simplicity, only the central element of the mesh is considered. The mean temperature and pressure for this element are 79.9 °C and  $1.7 \times 10^4$  kPa respectively. The Beta\_Gamma module returns a value of BETASTAR equal to  $3.502 \times 10^{-4}$  1/K which leads to a fluid density equal to 979.24589 kg/m<sup>3</sup> (Eq.5) On the other hand, by replacing the (Eq 7.) the fluid density calculated by use of the polynomial fitting is equal to 979.24589 kg/m<sup>3</sup>. Since the numerical value of BETASTAR coincides with the value obtained from the polynomial fitting the code is validated.

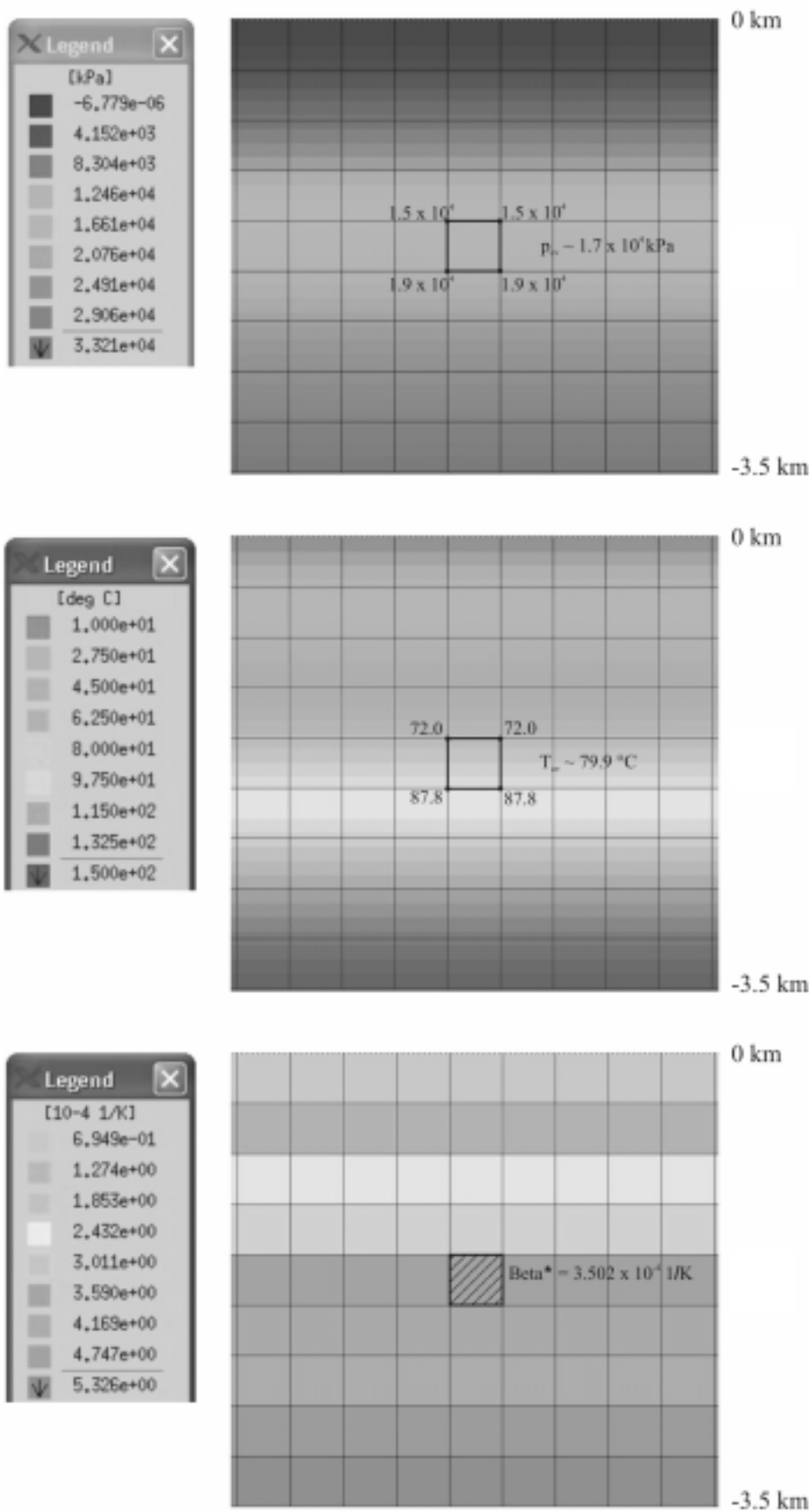


**Fig.1** Calculated pressure (A) and temperature (B) input data and returned BETASTAR (C) by the use of the Beta\_Gamma module.

## Appendix 4. Rayleigh stability criteria

### *Brief historical overview of double-diffusive convection (DDC)*

Convective flows are driven by density variations within fluid. DDC is mentioned when the density variations are caused by two factors which have different rates of diffusion. The archetypal example is heat and dissolved salt in water often referred to as thermohaline convection.

First experimental investigations on convective currents and stability were carried out in viscous liquids by Jevons (1857), Rayleigh (1883) and Ekman (1906) over the period 1856-1906. These pioneers of convection motions generally investigated the stability of stratified fluid layers with density either increasing or decreasing by means of different observational scenarios.

As shown in the schematic picture in Fig.1, we can distinguish two main groups of instability:

- A diffusive regime favoring oscillatory instability (Fig.1A), where the destabilizing potential results from the component with larger diffusivity (i.e., colder at the top, warmer at the bottom) while the concentration gradient is stabilizing (i.e., fresher at the top, saltier at the bottom).
- A finger regime favoring monotonic instability (Fig.1B), where the driving destabilizing forces are caused by the more slowly diffusing component (i.e., saltier at the top, fresher at the bottom) while the temperature gradient is stable (warmer at the top, colder at the bottom).

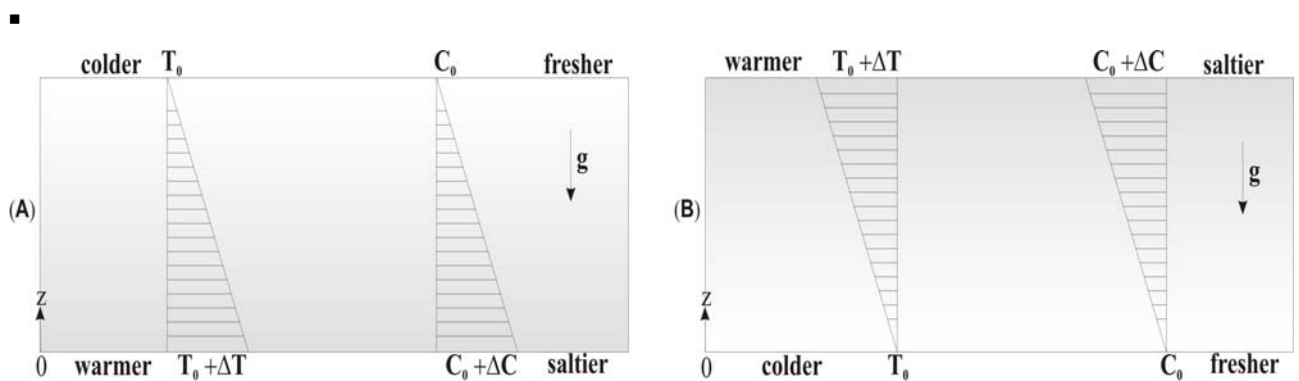


**Fig.1:** Temperature (T) and concentration (C) profile for two different DDC regimes: (A) diffusive regime, (B) finger regime. From Nield and Bejan 1999



From these stability studies, in 1916 Lord Rayleigh provided a criterion to predict the occurrence of instability in an adverse linear temperature gradient in a fluid layer (Rayleigh 1916). Such condition is described by a dimensionless number named in his honor, the Rayleigh number.

Nevertheless, DDC was “rediscovered” and understood only in 1960 as an oceanographic curiosity by Stommel (1956) and Stern (1960). Stern studied the long fingers of rising and sinking water which are produced when hot salty water lies over cold fresh water. A blob of hot salty water which finds itself surrounded by cold water rapidly loses its heat while retaining its salt due to the very different rates of diffusion of heat and salt (the first diffusing much more faster than the latter). Consequently, the salty blob loses part of its heat while it keeps more or less the same salt concentration hence becoming denser than the surrounding fluid. This tends to make the blob sink further, drawing down more hot salty water from above which gives rise to sinking fingers of salty fluid. At the same time, the surrounding fluid gains heat from these descending fingers and in turn it becomes lighter and moves upward. Eventually, the region becomes filled with fingers of salty and fresh water protruding in alternating downwards and upwards directions.

In the late 1960s, DDC has been demonstrated to be also possible in porous media (Bird et al. 1958; Nield 1968; Nield 1991). Since then a multitude of stability analysis based on laboratory experiments were carried out on saturated porous media with vertical gradients of temperature and salinity (Trevisan and Bejan 1987; Qin et al. 1995; Cooper et al. 1997; Tan et al. 2003; Kubitschek and Weidman 2003). Owing to the presence of the solid matrix, the theory of convective motions in porous media introduces essential differences from the one in viscous fluids. For example, according to the term of heat accumulation in equation (2.55), the contribution due to thermal absorption by the solid grains is taken into account, a feature totally absent in thermohaline convection in viscous fluids. The solid grains play a primary role on the dynamic of mass transport as already seen in the paragraph 2.5 dedicated to hydrodynamic dispersion. In addition, from equation (2.49) it results that advection is governed by Darcy’s law rather than by the Navier-Stokes equations applicable for viscous flow. Darcy’s law introduces a new fundamental parameter, the hydraulic permeability, characterizing unequivocally the porous media in which the flow takes place and controls its velocity. The equation of motion expressed in the form of (2.50) shows further that the flow is caused by two driving force: one resulting from piezometric head differences and the other resulting from a buoyancy force.

## *Convection stability*

Here the convection stability criteria is derived for a porous media in diffusive regime, i.e. where heat and salt are respectively the destabilizing and stabilizing buoyancy forces, such as in the case of a infinite horizontal porous layer heated from below. This problem, also known as the Horton-Rogers-Lapwood problem (Horton and Rogers 1945), was studied in its double-diffusive generalization by Nield (Nield 1968). Since there are two sources of buoyancy (heat and dissolved salt), there are two Rayleigh numbers that characterize the convection processes: the thermal Rayleigh number  $Ra$  and the solutal Rayleigh number  $Ra_D$ . From a dimensional analysis of the governing balance equations in paragraph 2.5 the following definition of Rayleigh number for solutes and thermal energy are given (Nield and Bejan 1999):

$$Ra = \frac{K \beta \Delta T d}{\lambda} \quad (4.1)$$

$$Ra_D = \frac{K \alpha \Delta C d}{D} \quad (4.2)$$

where  $K$  is the hydraulic conductivity as defined in Eq.(2.51)  $\alpha$  introduces the effect of a density change due to the concentration the solute at temperature and pressure  $\beta$  is the coefficient of thermal expansion at constant pressure and concentration,  $\lambda$  is the coefficient of thermal conductivity,  $\Delta C$  is the concentration variation,  $\Delta T$  is the temperature variation,  $d$  is a characteristic length of the porous media (e.g., the layer thickness),  $D$  is the coefficient of molecular diffusion.

The solutal and thermal Rayleigh numbers are related by:

$$Ra_D = N \cdot Le \cdot Ra \quad (4.3)$$

where the dimensionless numbers in connection with heat and mass transport are:

$$\begin{aligned} N &= \frac{\alpha \Delta C}{\beta \Delta T} \\ Le &= \frac{\lambda}{D} \end{aligned} \quad (4.4)$$

$N$  is called the buoyancy ratio (or Turner number) and  $Le$  is the Lewis number.

The Rayleigh numbers as expressed in equation (4.1) and (4.2) are the ratio of driving forces of buoyancy and gravitation to the dissipative mechanisms of viscous drag and heat conduction ( $Ra$ ), and hydrodynamic dispersion ( $Ra_D$ ).

In the diffusive regime considered here,  $Ra$  promotes convection while  $Ra_D$  inhibits it. If the top and bottom surface of the porous layer are impermeable, isothermal and isosolutal ( $C$  constant) boundary conditions, a criteria for the onset of DDC is summarized as follows (Nield 1991, Diersch and Kolditz 2002 and Trevisan and Bejan 1987):

- The monotonic instability (or stationary convection) boundary is a straight line defined by  $Ra + Ra_D = Ra_c = 4\pi^2$ , where  $Ra_c$  is the critical Rayleigh number.
- The region delimited by  $Ra + Ra_D < 4\pi^2$  is a stable regime characterized by pure conduction and no convection. The portion of this region for which  $\Phi Ra + Ra_D > 4\pi^2(1 + \Phi)$ , where  $\Phi \equiv \frac{Le}{R}$ , corresponds to oscillatory instability. The boundary lines delimiting stationary convection and oscillatory convection intersects at  $Ra = \frac{4\pi^2\Phi}{\Phi - 1}$ ,  $Ra_D = \frac{4\pi^2}{\Phi - 1}$ . In Fig.2 is illustrated the case where  $\Phi = 2$
- In a range between  $4\pi^2 < Ra < 240-300$  steady state convective cells develop as two-dimensional rolls rotating in clockwise or counter-clockwise direction. A second critical Rayleigh number  $Ra_{c2} = 240-300$  is identified as an upper limit.
- For  $Ra > Ra_{c2}$  the convection regime is unstable and characterized by a transition to an oscillatory and transient convection behaviour.

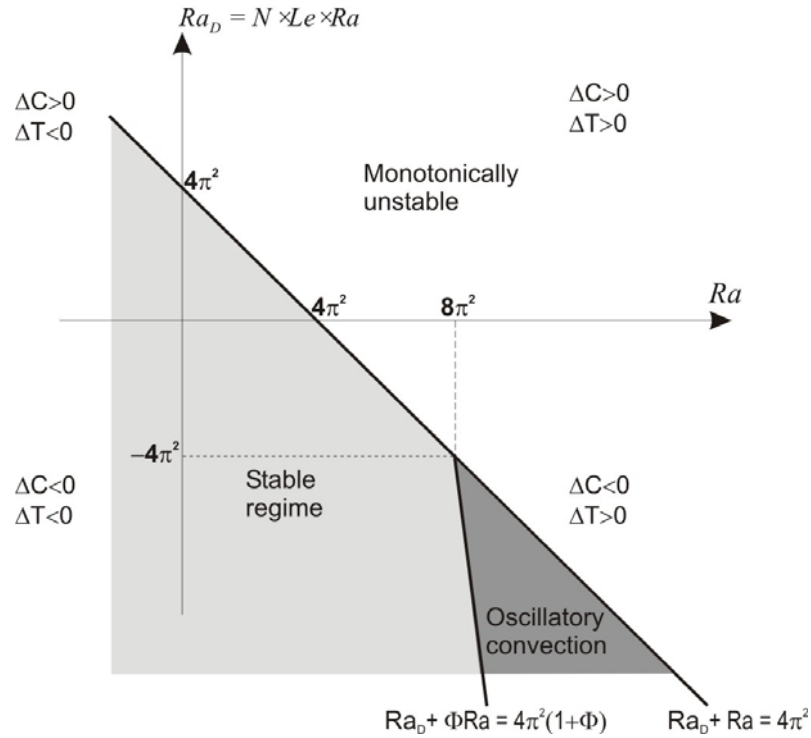


**Fig.2** Stability and instability domains for DDC in a horizontal porous layer with identical set of boundary conditions for  $\Phi = 2$ . Modified from Nield and Bejan 1999

As mentioned by Nield and Bejan (1999), when two settings of boundary conditions are identical thermal and solutal effects are additive otherwise the two effects won't be additive. In the latter, "the coupling between them will be less than perfect and one can expect that the monotonic instability boundary will be concave toward the origin". Critical values of  $Ra_c$  for various combinations of boundary conditions are given in Table.1.

<b>Boundary Key:</b> $K = \infty$ impermeable; $K = 0$ constant pressure $L = \infty$ constant temperature; $L = 0$ constant heat flux <b>Subscript:</b> l = lower; u = upper				
$K_l$	$K_u$	$L_l$	$L_u$	$Ra_c$
$\infty$	$\infty$	$\infty$	$\infty$	$4\pi^2 \approx 39.5$
$\infty$	$\infty$	0	0	27.1
$\infty$	$\infty$	0	0	12
$\infty$	0	$\infty$	$\infty$	27.1
$\infty$	0	0	$\infty$	17.65
$\infty$	0	$\infty$	0	$\pi^2 \approx 9.9$
$\infty$	0	0	0	3
0	0	$\infty$	$\infty$	12
0	0	$\infty$	0	3
0	0	0	0	0

**Table 1** Values of the critical Rayleigh number  $Ra_c$  for different set of boundary conditions from Nield 1991



## ERKLÄRUNG

Hiermit versichere ich, dass ich die Dissertation selbständig verfasst und keine anderen als die angegebenen Hilfsmittel verwendet habe. Daten, Materialien und Informationen, die ich durch andere erhalten habe, sind in der Arbeit kenntlich gemacht.

Diese Arbeit hat in gleicher oder anderer Form noch keiner Prüfungskommission (-behörde) vorgelegen.

Mit Genehmigung erfolgte Vorabveröffentlichungen von Teilergebnissen sind der Arbeit beigelegt.

Berlin,

## FABIEN MAGRI

### PERSONAL DETAILS

---

- **Address:** Uhlandstr. 153, 10719 Berlin - Germany
- **Mobile:** +491792389497
- **Email** fabienma@gfz-potsdam.de
- **Nationality:** French and Italian
- **Birth:** 07/12/1976 Milan, Italy
- **URL:** <http://www.gfz-potsdam.de/pb4/pg3/people/magri.html>

### EDUCATION

---

- **1995 - 2001** University of Milan (Italy), Physics  
Graduation in July 2002, earth physic-groundwater modelling.  
Topic of the master degree thesis:  
*Stationary groundwater model for the freatic aquifer of the Maggia Valley (Canton Ticino, CH)* (in Italian)
- **1981 - 1994** Lycée Stendhal de Milan Baccalaureat C (scientific)

### WORK EXPERIENCE

---

- **Winter 2001** Institute of Earth Sciences (IST) Trevano, Switzerland  
Team work concerning MaVal project (ground water model)  
Role: creation of a 2D groundwater model of the Maggia valley (Switzerland) with the finite differential technical (forward discreet problem)
- **At present** Research scientist in the DFG SPP 1135 project "[Deep reaching fluid flow in the Central European Basin System](http://www.gfz-potsdam.de/pb4/pg3/projects/deepcirculation.html)"  
GeoForschungsZentrum Potsdam, Germany  
(<http://www.gfz-potsdam.de/pb4/pg3/projects/deepcirculation.html>)  
Ph.D thesis submitted at the Freien Universität, Berlin, the 25<sup>th</sup> of February 2005. **Title:** Mechanisms and fluid-dynamics driving saline waters within the North East German Basin. Results from thermohaline numerical simulations.

### EXTRA WORK EXPERIENCE

---

Private tutoring of mathematics and physics.

### ACHIEVEMENTS

---

- **Winter 2001 University of Milan**  
Scholarship financed by IST (SUPSI, Trevano, Switzerland) for developing a numerical model for the Maggia aquifer.
- **1994 Lycée Stendhal de Milan**  
Distinction « good » in baccalaureate C + scholarship  
GeoForschungsZentrum Potsdam  
Scientific Technical Report STR 05/12

■ **28-29.11.2002 Schloß Eringerfeld, Geseke, Germany**

U. Bayer, F. Magri, C. Jahnke, P. Möller, A. Pekdeger, M. Tesmer, H. Voigt:  
DEEP REACHING FLUID-FLOW IN THE CENTRAL EUROPEAN  
BASIN SYSTEM, DFG Rundgespräch "SPP Sedimentbeckendynamik".  
(Abstract + Poster)

■ **6-12.04.2003 EGS, Nice, France**

Magri F., Bayer U., Jahnke C., Möller P., Pekdeger A., Tesmer M., Voigt H.:  
DEEP REACHING FLUID-FLOW IN THE CENTRAL EUROPEAN  
BASIN SYSTEM  
EGS-AGU-EUG joint Assembly, CD-ROM: Geophysical Research  
Abstracts, vol. , 2003; Abstract number: EAE03-A-01015 6-12 April 2003,  
Nice, France)

■ **18.06.2003 Hannover, Germany**

C. Jahnke, F. Magri, U. Bayer, P. Möller, A. Pekdeger, M. Tesmer, H. Voigt:  
DEEP REACHING FLUID-FLOW IN THE CENTRAL EUROPEAN  
BASIN SYSTEM, DFG  
Rundgespräch "SPP Sedimentbeckendynamik"

■ **3-5.12.2003 Bonn, Germany**

U. Bayer, F. Magri, C. Jahnke, P. Möller, A. Pekdeger, M. Tesmer, H. Voigt:  
DEEP REACHING FLUID-FLOW IN THE CENTRAL EUROPEAN  
BASIN SYSTEM, DFG Rundgespräch "SPP Sedimentbeckendynamik".  
(Abstract + Poster)

■ **25-30.04.2004 Nice, France**

F. Magri, U. Bayer, C. Jahnke: DEEP REACHING FLUID-FLOW IN  
THE CENTRAL EUROPEAN BASIN SYSTEM. 1<sup>st</sup> EGU General  
Assembly, Geophysical Research Abstracts, vol. 6, 00097, 2004;  
Abstract Number: Sref-ID: 1607-7962/gra/EGU04-A-00098. (Abstract  
+ Poster)

■ **28-30.09.2004 Leipzig, Germany**

F. Magri, U. Bayer, C. Jahnke: DEEP REACHING FLUID-FLOW IN  
THE CENTRAL EUROPEAN BASIN SYSTEM. GEOLEIPZIG  
2004, (Abstract + Poster)

■ **1-3.12.2004, Eringerfeld, Germany**

F. Magri, U. Bayer, C. Jahnke, P. Möller, A. Pekdeger, M. Tesmer, H. Voigt:  
SALTY WATERS IN THE N-E GERMAN BASIN. ORIGINS AND  
DYNAMICS. Terra Nostra. Heft Nr 2004/05, p 59-62. DFG  
Rundgespräch "SPP Sedimentbeckendynamik", (Abstract + Talk)

■ **21-25.03.2005, IPG Paris, France**

F. Magri, U. Bayer: Convective brine transport in the North East German  
Basin. Results from numerical simulations. (Abstract + Talk)



- Magri, F., 2004 Derivation of the coefficients of thermal expansion and compressibility for use in FEFLOW (+ implementation code in C++). WASY White papers Vol. III.
- Bayer, U., Magri, F., Clausnitzer, V., Jahnke, C., Fuhrmann, J., Möller, P., Pekdeger, A., Tesmer, M., Voigt, H., 2005 Deep reaching fluid flow close to convective instability in the NE German Basin. *Tectonophysics*, 397, 5-20
- Magri, F., Bayer, U., 2005 Deep reaching fluid flow in the NE German Basin. Fluid-dynamics driving saline waters. *International Journal of Geoscience*, in press